LEVEL III

031-806

MAR 12 1981

TECHNICAL REPORT

TO

THE OFFICE OF NAVAL RESEARCH
CONTRACT NO. N00014-78-C-0275

APPLICATION OF RAPID SOLIDIFICATION TECHNIQUES

TO ALUMINUM ALLOYS

BY

C. G. Levi and R. Mehrabian

Department of Metallurgy and Mining Engineering
Department of Mechanical and Industrial Engineering
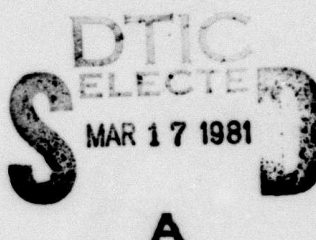University of Illinois
Urbana, Illinois 61801

October, 1980

DTIC
ELECTE
MAR 17 1981

S D

A

81 3 16 161

REPORT DOCUMENTATION PAGE

READ INSTRUCTIONS BEFORE COMPLETING FORM

1. REPORT NUMBER	2. GOVT ACCESSION NO.	3. RECIPIENT'S CATALOG NUMBER
6	AD-A096 492	

4. TITLE (and Subtitle)	5. TYPE OF REPORT & PERIOD COVERED
Application of Rapid Solidification Techniques to Aluminum Alloys.	Technical Report— 1 Jul 1979 to 31 Jan 1980.
	6. PERFORMING ORG. REPORT NUMBER

7. AUTHOR(s)	8. CONTRACT OR GRANT NUMBER(s)
C. G. Levi and R. Mehrabian	N00014-78-C-0275, ARPA Order-3517

9. PERFORMING ORGANIZATION NAME AND ADDRESS	10. PROGRAM ELEMENT, PROJECT, TASK AREA & WORK UNIT NUMBERS
Department of Metallurgy and Mining Engineering Department of Mechanical and Industrial Engineering University of Illinois, Urbana, IL 61801	12 206

11. CONTROLLING OFFICE NAME AND ADDRESS	12. REPORT DATE
Dr. E. C. vanReuth Defence Advanced Research Projects Agency 1400 Wilson Blvd., Arlington, VA 22209	October 1980
	13. NUMBER OF PAGES

14. MONITORING AGENCY NAME & ADDRESS(If different from Controlling Office)	15. SECURITY CLASS. (of this report)
Dr. B. A. MacDonald, Metallurgy Division Office of Naval Research, Code 471 Department of the Navy Arlington, VA 22217	Unclassified
	15a. DECLASSIFICATION/DOWNGRADING SCHEDULE

16. DISTRIBUTION STATEMENT (of this Report)

This document has been approved for public release and sale; its distribution is unlimited.

17. DISTRIBUTION STATEMENT (of the abstract entered in Block 20, if different from Report)

Approved for public release; Distribution Unlimited

18. SUPPLEMENTARY NOTES

19. KEY WORDS (Continue on reverse side if necessary and identify by block number)

Rapid Solidification, Atomization, Heat Flow, Nucleation, Growth Kinetics, Microstructure

20. ABSTRACT (Continue on reverse side if necessary and identify by block number)

This portion of the program was conducted for the purpose of developing a predictive model of heat flow and solidification for aluminum alloys produced under the high cooling rate conditions achievable in atomization processes. It is a combined experimental and theoretical study of the relationship between the important solidification variables (e.g. cooling rate, temperature gradients, interface shape and velocity, supercooling and transformation kinetics) and the structure of rapidly solidified aluminum alloy powders.

DD FORM 1473 **1 JAN 73** EDITION OF 1 NOV 65 IS OBSOLETE
S/N 0102-LF-014-6601

176014

JOB

This report covers that portion of the investigations which addressed the characterization of the thermal history of rapid solidification in metal droplets, and its effects on powder microstructure. The main effort was focused on modelling the heat flow during solidification, and relationships were established between the atomization parameters, the growth kinetics, the interface velocity and undercooling, and other important variables. Numerical solutions based on the enthalpy model were developed, and their results compared to the trends predicted from the Newtonian model. The analysis covered situations of isothermal solidification at the melting temperature, as well as those where significant undercoolings are necessary for nucleation and growth. The implications of single vs. multiple nucleation were also discussed.

In general, the results indicate that when substantial undercoolings are achieved in the droplet prior to nucleation, the thermal history consists of two distinct solidification regimes. In the first one, the interface velocities are high, the droplet absorbs most of the latent heat released, and the external cooling plays usually a minor role. The second regime is one of slower growth, and strongly depends on the heat extraction at the droplet surface. The extent of "rapid solidification", as determined from the fraction of material solidified above a certain critical undercooling, is a function of the nucleation temperature, the particle size, a kinetic parameter and the heat transfer coefficient. Substantial departures from the Newtonian model were calculated for Biot numbers as low as 0.0001.

The concepts developed from the heat flow analysis were coupled to microstructural observations in Aluminum alloy powders, mostly in the submicron size range. It was shown that reducing the particle size decreases the extent of segregation, promotes multiple nucleation and the formation of twins during solidification. Homogeneously solidified powders were found in Al-3%Si and 6%Si below 1 μm in diameter; their incidence is enhanced by reducing the solute content and increasing the heat transfer coefficient.

Accession For		
NTIS GRA&I	☑	
DTIC TAB	☐	
Unannounced	☐	
Justification		
By		
Distribution/		
Availability Codes		
Dist	Avail and/or Special	
A		

APPLICATION OF RAPID SOLIDIFICATION

TECHNIQUES TO ALUMINUM ALLOYS

Abstract

This investigation was the last part of a program conducted for the purpose of developing a predictive model of heat flow and solidification of aluminum alloys produced under conditions of high cooling rates. It addresses the characterization of the thermal history of rapid solidification in metal droplets, and its effects on powder microstructure. The main effort was focused on modelling the heat flow during solidification, and relationships were established between the atomization parameters, the growth kinetics, the interface velocity and undercooling, and other important variables. Numerical solutions based on the enthalpy model were developed, and their results compared to the trends predicted from the Newtonian model. The analysis covered situations of isothermal solidification at the melting temperature, as well as those where significant undercoolings are necessary for nucleation and growth. The implications of single vs. multiple nucleation were also discussed.

In general, the results indicate that when substantial undercoolings are achieved in the droplet prior to nucleation, the thermal history consists of two distinct solidification regimes. In the first one the interface velocities are high, the droplet absorbs most of the latent heat released, and the external cooling usually plays a minor role. The second regime is one of slower

growth, and strongly depends on the heat extraction at the droplet surface. The extent of "rapid solidification", as determined from the fraction of material solidified above a certain critical undercooling, is a function of the nucleation temperature, the particle size, a kinetic parameter and the heat transfer coefficient. Substantial departures from the Newtonian model were calculated for Biot numbers as low as 10^{-4}.

The concepts developed from the heat flow analysis were coupled to microstructural observations in aluminum alloy powders, mostly in the submicron size range. It was shown that reducing the particle size decreases the extent of segregation, promotes multiple nucleation and the formation of twins during solidification. Homogeniously solidified powders were found in Al-3%Si and 6%Si below 1 μm, in diameter; their incidence is enhanced by reducing the solute content and increasing the heat transfer coefficient.

ACKNOWLEDGEMENTS

TABLE OF CONTENTS

LIST OF TABLES

TABLE   PAGE

LIST OF FIGURES

FIGURE   PAGE

FIGURE   PAGE

FIGURE   PAGE

CHAPTER 1

INTRODUCTION

Atomization is perhaps the process with the highest potential for large scale production of rapidly solidified metals. However, early methods for generation of metal powders were limited in their achievable cooling rates to about 10^4 K s^{-1}, and their benefits in terms of property enhancement were mainly due to microstructural refinement and homogeneous distribution of second phases and inclusions. Extensive research on splat cooling and related techniques, where cooling rates are estimated to range from 10^6 K s^{-1} to 10^9 K s^{-1}, has led to a variety of metastable modifications in alloy microstructure. These results broaden the scenario for alloy development, for example, through extension in solid solubility of elements in the primary phase, as in the cases of highly ductile aluminum-silicon alloys and precipitation hardening aluminum-iron alloys. An important goal in metal powder production is then to increase the achievable cooling rates, and newer processes like centrifugal atomization are claimed to surpass 10^6 K s^{-1} by improvements in the droplet-gas heat transfer coefficient, resulting from high droplet velocities and controlled particle size in the range of 100 µm or less. However, in order to optimize the capabilities of atomization it is necessary to understand the solidification mechanism in small metal droplets and its relationship to

progressively higher rates of heat extraction.

There is also a theoretical interest in solidification of metal powders. Atomization is unique among the rapid cooling processes because the interactions with molds, substrates or other solidifying particles are practically absent. Conceivably, then, most of the liquid droplets could achieve high undercooling levels prior to nucleation--provided the purity level is adequate--because the active nucleation catalysts will be isolated in a small fraction of the total volume. In addition to this undercooling, the very efficient heat transfer is expected to partially relieve the recalescence effects and increase the driving force for microstructural modifications. Furthermore, the development of electrohydrodynamic atomization has provided a tool for the controlled generation of powders below 1 μm in diameter. These powders, while not of commercial importance, are especially suited for fundamental studies because they are electron-transparent, and therefore permit the three-dimensional observation of a complete solidification structure.

It is evident from the current literature that the microstructures resulting from rapid solidification of alloy powders can not always be explained with available theories of nonequilibrium dendritic growth. The purpose of this investigation was to enhance our understanding of the relationship between the process variables in atomization, the undercooling and the growth kinetics, and the powder microstructure and microchemistry.

There were two main areas of interest in the scope of this investigation. The first one is basically theoretical and was aimed to modelling the heat transfer during cooling and solidification of atomized metal droplets. The second is experimental and involved the microstructural characterization of aluminum alloy powders produced by two different atomization techniques. The formation of these structures is discussed in terms of the heat flow results and the current understanding of the solidification mechanisms.

CHAPTER 2

LITERATURE REVIEW

In the search for improved properties in aluminum alloys a variety of techniques which involve the direct quenching from the liquid state have been investigated. The general approach in most of them has been to reduce the volume or thickness of material being solidified at one time. A second goal in their development has been to increase the heat extraction efficiency between the "casting" and the "heat sink". The overall effect is the achievement of cooling rates estimated in the range of 10^3 to 10^9 K s^{-1}.

Solidification under the increasingly higher cooling rates --and conceivably higher undercoolings--typical of atomization, splat cooling or any of their related techniques, commonly results in progressive departure from the microstructures produced by conventional casting. The first part of this review summarizes the structural modifications reported for aluminum alloys processed by rapid solidification (RSP), whereas the second part is devoted to the thermodynamic and kinetic considerations involved in the current interpretation of these phenomena.

2.1 Metastable Effects in Rapidly Solidified Aluminum Alloys

Rapid solidification of aluminum alloys commonly results in one or more of the following modifications:

1. microstructural refinement, manifested as smaller grain size and dendrite arm spacings;

2. extension in terminal solid solubility of the primary α-Al phase;

3. morphological changes of the eutectic or the primary phase;

4. formation of non-equilibrium phases;

5. coupled eutectic growth at off-eutectic compositions; and

6. vacancy supersaturation.

Although all these effects have been observed in aluminum alloys, some even at the moderate cooling rates of 10 to 10^3 K s^{-1}, only the first four are reviewed herein because they are the most important in terms of improving the properties of the final product.

2.1.1 Microstructural refinement

In general, the fineness of dendritic microstructures can be correlated to the average cooling rate during solidification, ε, or the local solidification time (i.e. time available for coarsening), t_f, by:

$$DAS = a\ \epsilon^{-b} = a\ (T_L - T_S)^{-b}\ t_f^b \qquad (2.1)$$

where $(T_L - T_S)$ is the solidification temperature range, DAS is
the dendrite arm spacing, a and b are constants. Relationships
of this type have been established for a series of aluminum
alloys [1-4], although experimental difficulties have usually
limited the range of accurately measured cooling rates to less
than 10^3 K s^{-1}. For example, studies in Al-4.5%Cu^{+} at cooling
rates between 10^{-5} and 10^3 K s^{-1} yield values for a = 40 and
b = 0.39 [2,3]. Values for a = 47 and b = 0.33 have also been
determined for thin castings of Al-10.5%Si at cooling rates up to
10^5 K s^{-1} [4].

Dendritic spacings of 0.01 to 0.5 μm [5-8] and eutectic
spacings in the same order of magnitude [9] have been reported
for electron transparent areas of Al alloy gun splats. When
these data were plotted versus the corresponding average cooling
rates estimated from heat flow calculations, they were found in
reasonable agreement with the extrapolation of Equation (2.1) for
a and b established at much lower cooling rates [3,5,6]. These
results gave then origin to the common practice of estimating
cooling rates based on dendrite arm spacing measurements in
rapidly solidified materials. It should be noted, however, that
caution must be exercised in following this practice, since the
dendritic morphologies change sometimes markedly as cooling rate
increases. Furthermore, the constants in Equation (2.1) vary
with alloy system and composition, although there is some

[+]weight % unless otherwise specified

disagreement in the literature as to the influence of this latter variable. Studies on the effect of alloy composition on structure at fixed average cooling rate for Al binary alloys with Cu, Mg, Si or Zn have shown that increasing the solute content refines the dendrite arm spacing, especially at low solute concentrations [1,10].

Refinement of secondary phases including eutectic constituents also occurs with increasing cooling rate during solidification. Dispersion hardening associated with this effect has been reported in Al-Si [11] and Al-Fe [12] base alloys.

2.1.2 Extension of solid solubility

Extension of the equilibrium terminal solid solubility has been obtained at sufficiently high cooling rates in almost all the aluminum alloy systems investigated, Al-Zn being the only notable exception [13,14]. Table 1 shows the maximum supersaturations reported for several elements in aluminum.

Increased solid solubility via rapid solidification permits higher alloying levels resulting in superior strength-ductility combinations in a number of systems. Enhanced solid solution hardening and dispersion strengthening after aging have been reported for Al-Cu compositions beyond the equilibrium solubility limit [15]. The possibility of precipitation hardening in Al-Fe base alloys has been demonstrated [16], and considerable interest exists in the substantial ductilities attainable in high-silicon aluminum alloys [17,18].

Table 1

Extension of Solid Solubility in Binary Aluminum
Alloys Quenched from the Melt [14]

| Solute | Maximum at Equilibrium | | RSP Data |
	$T_E(K)$	X_E(at%)	(at%)
Cr	934	0.44	5-6
Cu	821	2.48	17-18
Fe	928	0.025	4-6
Mg	724	16.3	36.8-40
Mn	932	0.9	6-9
Ni	913	0.023	1.2-7.7
Si	850	1.59	10-16
Zn	655	66.5	38

There are indications that the extent of solute
supersaturation increases with the severity of the quench and
increased nominal alloy composition [14,15]. Furthermore, it has
been shown that additions especially prone to solubility
extension in binary alloys (e.g. Mn) can be used in ternaries to
increase the solubility limit of less susceptible elements (e.g.
Fe, Co, Ni) [19].

2.1.3 Morphological modifications

A variety of grain shapes and dendrite morphologies have
been reported in alloys quenched from the liquid state [20,21].
The primary phase dendrites in some alloys tend to assume a
cellular or rod-like configuration with progressively faster
cooling rates [6,21]. Similar observations have been reported
for bulk specimens of nickel and iron base alloys with increasing

supercooling prior to nucleation of the solid phase [22]. In addition, rapid solidification can sometimes suppress formation of an equilibrium primary phase from the melt. For example, formation of α-Al dendrites instead of equilibrium Al_3Fe phase has been reported in hypereutectic Al-Fe alloys both in chill-cast [23] and splat-cooled specimens [24].

Rapid solidification may also alter the composition range of cooperative eutectic growth, the eutectic constituents and their morphologies. For example, quenching liquid Al-Fe alloys in the range of 10 to 10^4 K s^{-1} has resulted in eutectic morphologies changing from irregular $Al-Al_3Fe$ to regular $Al-Al_6Fe$, as well as coupled eutectic growth at noneutectic compositions [23,25]. Changes in the interdendritic eutectic from lamellar to rod-like have been shown to occur at high cooling rates [24]. In addition, degenerate and radial eutectic structures in Al-17.3 at%Cu and structural changes as a function of Cu content have been studied via splat cooling [26].

2.1.4 Nonequilibrium phases

Formation of nonequilibrium phases during rapid solidification of aluminum alloys is not as common as the effects noted above. Nevertheless, a certain number of cases are reported in the literature and have been classified by Jones [14] in three types:

I - Phases existing at equilibrium but not stable at the temperature and alloy compositions in which they were observed. Examples include the formation of Al_4Mn and Al_4Cr in alloys where the phases in equilibrium with α-Al are Al_6Mn and Al_7Cr [27,28].

II - Phases not formed from the melt, which either appear during quenching through the solid state, or are precipitated upon further heat treatment. Aging of rapidly solidified Al-Fe alloys shows a sequence of precipitation similar to the Al-Cu system [29,30]. Supersaturated Al-Si solid solutions also exhibit a gradual decomposition, starting with GP zones which are nucleated by clustering of Si-vacancy pairs [31]. Although some vacancies are annihilated to accomodate the misfit between the matrix and the cluster, coherent GP zones do not grow appreciably larger than 1.5 to 2 nm [32]. Subsequent precipitation has been reported to produce spherical, acicular and lamellar morphologies, as well as rods and distorted cubes, depending on the alloy composition and the thermal history [33-36]. Si needles and plates commonly form on the {111} and {100} planes of the Al parent crystal [32].

III - Phases resulting from rapid solidification, but not known to exist under equilibrium conditions at any other composition within the alloy system. Typical of

this type are the formation of Al_6Fe in contact with α-Al, replacing the equilibrium phase Al_3Fe [37]. Al_3Cu_2 has been produced by splat quenching Al-45at%Cu, whose constituents at equilibrium are θ ($CuAl_2$) and η_2 ($\sim$CuAl) [38]. Furthermore, non-crystalline structures have been reported in Al-17.3at%Cu [9], Al-30at%Ge [39], Al-Si and Al-Pd alloys [40].

It is commonly observed that particular nonequilibrium effects do not happen above a critical thickness in splat cooling [41], i.e., below a given cooling or growth rate during solidification. For example, Al_6Fe can displace the equilibrium phase Al_3Fe at cooling rates as low as 3 K s^{-1}; however, cooling rates of the order of 10^4 K s^{-1} are required to avoid formation of FCC Al_3Mg_2 in Al-Mg alloys [14].

2.2 Thermodynamic and Kinetic Considerations

In normal solidification processes it is usually assumed that the thermodynamic conditions at the interface, i.e. temperature and composition, correspond fairly closely to those dictated by the equilibrium phase diagram, and that the growth rate is mainly controlled by the dissipation of the latent heat away from the moving front. The results of theories assuming local equilibrium at the interface, which can predict the nonequilibrium solidification path and phase composition in the

resulting microstructures, have been considered as supportive of the cited assumption. However, when dealing with processes where the heat extraction mechanisms are very efficient and the volumes of material involved are small (splat cooling or atomization), the theories based on interface equilibrium do not always satisfactorily explain the metastable structures obtained, and kinetic considerations must be brought in to understand the solidification process. The following paragraphs summarize the basic thermodynamic and kinetic concepts involved in the current interpretation of rapid solidification phenomena. Since the extension of solid solubility is of special interest to the field, part of this review is devoted to that particular topic.

2.2.1 Nucleation

Solidification under rapid cooling rates is normally a nucleation and growth process, except in the formation of amorphous metals. This latter phenomenon is usually ascribed to the existence of a large energy barrier for the atoms to join an embryo (i.e. the viscosity is high or the diffusivity is low), therby suppressing nucleation until the metal reaches its glass transition temperature [42]. Recent investigations [43] have shown that amorphous solidification can be obtained in some eutectic alloys even in the presence of the crystalline phase (no need for nucleation). If the alloy is thermodynamically unable to form a single phase, and the solidification velocity is

increased enough to overcome the diffusion-controlled partitioning process at the interface, the growing eutectic exhibits a transition to glass. Nevertheless, amorphous solidification is not of common occurrence in the atomization processes and alloys of interest to this work, and therefore will not be further discussed.

Since the growth rate is considerable at relatively small undercoolings for metals and other liquids of high fluidity, nucleation is usually the controlling step in the crystallization process. Although a number of theories for homogeneous and heterogeneous nucleation based on the classical droplet model have been developed and discussed elsewhere [44], their application is limited by the lack of data, especially regarding the surface energies. Classical models usually assume isothermal conditions and a steady state distribution of embryos and their applicability to condensed systems has been questioned in the past. Turnbull [45] proposed the concept of an "incubation period" (whose length depends on the diffusivity) for the steady state distribution of embryos to develop when the sample is rapidly cooled from above to below the melting temperature. Reiss and Katz [46] have analyzed the nucleation problem during continuous cooling, and assuming that the liquid self-diffusion coefficient, D_L, obeys an Arrhenius-type law, they concluded that cooling rates in excess to 10^{12} K s^{-1} are necessary to avoid the steady state distribution in liquid copper. However, they also claim that the actual value of D_L may be actually more than six

orders of magnitude smaller than the value predicted by the Arrhenius extrapolation and, therefore, cooling rates in excess of 10^6 K s^{-1} would be large enough to produce significant deviations of the nucleation rate from that predicted by the steady state model. In general, for nucleation to be suppressed until a desired undercooling is reached in an assembly of volume V, the total number of nuclei N, given by

$$N = V \int_0^t J(t) \, dt \tag{2.2}$$

should be less than unity. In this expression the nucleation frequency J is a function of time t due to the variations in temperature and cooling rate during quenching.

Another factor which may be questionable regarding the applicability of classical expressions to nucleation in small droplets is the number of atoms available to produce and maintain the statistical distribution of embryos.

Experimental programs using either an emulsion of droplets [47-51], or single droplets [52] as a means of isolating the heterogeneous nucleation catalysts in a small fraction of the liquid, have been aimed at determining the maximum undercooling ΔT_N (conceivably the onset of homogeneous nucleation) achievable in a metal or alloy. Hollomon and Turnbull [48] found that most metals investigated reach a maximum undercooling of about 0.18 T_M (e.g., they obtained a ΔT_N for aluminum of 195 K or

$0.21 \ T_M$). More recently Perepezko et al. [49] found undercoolings for Sn and Bi in the range of $0.35 \ T_M$ and therefore indicated that the previously reported values (and perhaps even these latter ones) correspond to heterogeneous and not homogeneous nucleation. Furthermore, it has been shown that reducing the droplet size markedly increases the achievable undercooling [50]. Droplet experiments in the Sn-Bi [49] and Cu-Ni [51] systems revealed that undercoolings comparable to those of the pure metals can be obtained in alloys throughout the entire phase diagram.

Undercooling results have been used in the past to estimate the values for the liquid-solid interfacial energies from classical nucleation theory [48]. However, the data obtained will always be underestimated unless homogeneous nucleation conditions are satisfactorily established [49].

Christian [42] has examined the compositional variations during the nucleation of solid from a liquid alloy. Using the free energy (F) vs. composition (X) diagram he indicated that the maximum driving force for a solid of composition X' to nucleate from a liquid of composition X_0 corresponds to the point at which

$$(\partial F_S / \partial X)_{X'} = (\partial F_L / \partial X)_{X_0} \qquad (2.3)$$

where F_S and F_L are the molar free energies of the solid and the

liquid respectively. Therefore, if nucleation occurs in the liquid-solid range the composition of the solid X' differs from that of the liquid X_0 by a greater amount than does the composition of the equilibrium solid, X_{SE}. However, the chemical term of the surface free energy tends to drive X' in the opposite direction. If nucleation occurs below the solidus temperature it is not possible to generalize if the first solid to form will be richer or poorer than X_{SE}.

For alloys in the two-phase range of a eutectic binary, a critical undercooling must be achieved for the nucleation of each phase, and the second phase must either nucleate heterogeneously on the primary phase or homogeneously in the liquid. The general conclusion from Christian's analysis is that the proportion of the two phases in a solidified alloy within the eutectic range will only agree with that calculated from the equilibrium phase diagram if one phase acts as a perfect catalyst for the nucleation of the other. The discussion assumes that no recalescence takes place during solidification, and that no foreign catalysts are present.

Several authors have utilized variations of the droplet technique to study the catalyzing effect of the primary phase on the nucleation of the second phase in several systems [50,53,54]. For example, undercoolings of 68 and 176 K (with respect to the solidus and liquidus corresponding to the composition of the liquid phase at the moment of nucleation) were obtained for the nucleation of Si on Al. Furthe   e, it was found that for

certain systems like Al-Ge the undercoolings observed were greater than those reported previously for "homogeneous" nucleation, implying that the crystalline substrate (Al) had no influence on the nucleation of the second phase from the liquid. These results were examined by Cantor and Doherty [55] who proposed a model to quantify the catalyzing activity of the primary phase, and concluded that in some cases like Zn-Bi the solute (Bi) had nucleated homogeneously from the liquid.

2.2.2 Growth kinetics

Most of the rapid solidification processes are believed to take place in the continuous growth regime with a diffuse interface [56]. The kinetic relationship suggested by Turnbull [57] for the steady-state continuous growth of a planar front is

$$R = (D_{LM}/\delta) \; \exp(-E_D \Delta T^*/T^*) \; [1-\exp(-\Delta H_M \Delta T^*/R' T_M T^*)] \qquad (2.4)$$

where R is the interface velocity, D_{LM} is the self-diffusion coefficient in the liquid at the melting temperature, E_D is the activation energy for diffusion, ΔT^* and T^* are the interface undercooling and temperature, respectively, ΔH_M is the heat of fusion at the melting temperature T_M, δ is the length of an interface step and R' is the gas constant. For moderate undercoolings the above equation reduces to

$$R \cong \beta(D_{LM}/\delta) \; (\Delta H_M/R' T_M^2) \; \Delta T^* \qquad (2.5)$$

$$\beta = (\delta/\gamma)^2 \ (\upsilon^*/\upsilon_L) \qquad\qquad (2.6)$$

where β is a factor incorr rated by Cahn et al. [56] including
the ratio of the jumpin equencies near the interface υ^* and in
the liquid υ_L, the average jumping distance for an atom to join
the solid γ and the length of an interface step δ. Values for β
vary from 1 to 100 for symmetric molecules.

Equations (2.4) and (2.5) will be henceforth called the
exponential and linear laws respectively. For the purposes of
this work the factor β was also included in Equation (2.4).

Shaefer and Glicksman developed a mathematical model to
study the effects of curvature and heat flow in the transient
growth of a spherical crystal nucleus in an infinite undercooled
melt [58]. Their analysis shows that the initial growth rate is
very small due to the large effect of the surface tension right
after nucleation. The interface velocity increases rapidly as
the curvature is reduced, goes through a maximum and then reaches
a steady state whose characteristics depend on the melt
undercooling and a kinetic parameter.

The problem of stability of a moving interface has been
extensively discussed in the literature. For most cases of low
interface velocities the principle of constitutional supercooling
has been widely used as an adequate guideline to determine the
growth conditions that result in unstable interfaces during alloy
solidification [59]. This principle is basically an application
of thermodynamics to determine if the liquid ahead of a moving

interface is undercooled with respect to its composition. The stability parameter emerging from this theory is the ratio of the temperature gradient in the liquid ahead of the moving interface G_L to its velocity R. Greater stability is promoted by increasing G_L/R.

The theory of morphological stability [60,61] approaches the problem from a kinetic point of view, solving the thermal and diffusion field equations about the interface under steady state conditions. It is also assumed that local equilibrium prevails at the solidification front. The resulting criterion identifies three factors contributing to the overall stability of the interface. The solute field created by segregation is always destabilizing, but the capillary forces always oppose the growth of a perturbation. The thermal field, as determined by the average gradient

$$G_{SL} = 2 \ (k_S G_S + k_L G_L)/(k_S + k_L) \tag{2.7}$$

will be stabilizing if G_{SL} is positive, and destabilizing in the opposite case. k_S and k_L are the thermal conductivities of the solid and liquid respectively. Note that while the constitutional supercooling criterion predicts instability for all cases where $G_L < 0$, the morphological theory may predict stability if G_S is sufficiently positive to make the average gradient term also positive.

Recent studies have compared the predictions of both theories for the case of rapid solidification. Cohen et al. [62] mapped the regimes of stability in a G_L vs. R plot and indicated that sufficiently increasing the cooling rate and decreasing composition will promote planar interfaces. Other studies [63,64] have extended the morphological stability theory and indicated that two effects are important in rapid solidification phenomena. The first one is known as absolute stability and arises because only short wavelength perturbations are important at high velocities, and these are stabilized by surface energy. The net result is that given a sufficiently high velocity the interface will be stable for any value of G_L (assuming that G_{SL} is positive). The second effect is caused by departure from local equilibrium at the interface. Coriell and Sekerka [64] concluded that most departures from local equilibrium enhance the interface stability, especially in the case where the partition coefficient tends to 1. Baker [65] analyzed the behavior of the partition coefficient as a function of interface velocity for various models and indicated that given a sufficiently high velocity the partition coefficient will always tend to unity.

Interface instability usually leads to cellular or dendritic patterns depending on the growth conditions. Analysis of dendritic solidification has been approached by several authors [66-68]. In general, the growth of a dendrite tip into a supercooled melt can be described by an expression of the type

$$\theta^* = -Pe \; e^{Pe} \; Ei(Pe) \qquad\qquad (2.8)$$

$$\theta^* = C_L(T^* - T_M)/\Delta H_M = -C_L \; \Delta T^*/\Delta H_M \qquad (2.9)$$

$$Pe = (R \; r_t/2\alpha_L) \qquad\qquad (2.10)$$

where θ^* is the dimensionless tip temperature, Pe is the Peclet number, relating the tip velocity R and radius r_t, T^* and ΔT^* are the temperature and undercooling of the dendrite tip respectively, and α_L and C_L are the thermal diffusivity and specific heat of the liquid respectively.

Glicksman and Huang [69] have developed a series of relationships between the microstructural size scale (segregate spacing) and interface undercooling, and concluded that for small ΔT the spacing should be a fixed multiple of the critical nucleation radius. Furthermore, they suggested that as supercooling increases towards unity the scale of the morphology should become rapidly smaller. They also studied the coarsening process during solidification and indicated that the initial microstructure is produced far from thermodynamic equilibrium in order to comply with the transport processes during growth. The final microstructure tends to be substantially different from that produced at the dendrite tip conditions, and can be correlated to the coarsening time by a scaling law.

2.2.3 Extension of solid solubility

Massalski and Bienvenu have discussed the limitations imposed by the Hume-Rothery rules on the metastable extension in solid solubility in the systems formed by the quartet Cu, Zn, Ag and Cd [70]. They indicate that complete miscibility through the phase diagram requires a certain undercooling for which the free energy of the liquid F_L is higher than that of the solid F_S for all compositions. If the size factor or a difference in crystal structure produces a "hump" or a discontinuity on the F_S curve, complete miscibility may never be achieved.

The assumption of local equilibrium at the interface implies that extension in solid solubility results from suppressing nucleation of the second phase below the eutectic temperature. The system then follows the metastable solidus line as it moves into the two phase region of the phase diagram. Therefore, the maximum solid solubility is limited to the composition dictated by this metastable solidus at the solidification temperature. Experiments in Zn-Cd, a system with a retrograde solidus, have shown this hypothesis to be incorrect, and furthermore have proven the occurrence of solute trapping and deviation from local equilibrium at the liquid-solid interface [71].

Baker and Cahn [72] have discussed the thermodynamics of nonequilibrium solidification in a binary alloy. With the aid of free energy (F) vs. composition (X) curves, they defined the domain of possible interface compositions for isothermal and

steady state solidification. They concluded that for any liquid composition X_L, there is a range of solid compositions X_S which are thermodynamically viable. The maximum X_S that can be formed at the temperature of interest is determined by the point at which the liquid and solid free energy curves intersect. This is known as the $X(T_O)$ composition and the locus of all these points forms a curve between the liquidus and the solidus of the equilibrium phase diagram. Therefore, the T_O curve effectively limits the achievable solid solubility at a given temperature, regardless of solidification rate. Partitionless transformations can occur only if $X_L < X(T_O)$ (or equivalently if $T < T_O$ for any X_L). This involves an increase in the chemical potential of the solute on crossing the interface and therefore implies that the two species have to solidify in a "cooperative" manner. The solute is then "trapped" by a reaction which produces an overall decrease in the free energy of the system.

Cahn et al. [63] have indicated that for a system with a retrograde solidus the maximum value of $X(T_O)$ occurs at 0 K and corresponds approximately to the value of the liquid composition in equilibrium at the retrograde temperature. They also compared calculated maxima for Zn-Cd and some Si-base alloys with the maximum solubility extension observed in those systems during rapid solidification, and concluded that the estimated bounds were consistent with the experimental results.

Hillert and Sundman have used the solute drag treatment to determine the limiting conditions for partitionless

solidification [73]. Their results indicate that the critical temperature for this process is lower than the T_O value and depends on the interface velocity and the ratio of the diffusivities in the solid and the liquid.

When nucleation is suppressed below the solidus temperature, the first solid to form is of composition very similar to the liquid. However, since heat extraction in metal droplets is usually controlled at the surface, and the growth rates are large for undercoolings higher than a few degrees, the solidification process after nucleation is considered essentially adiabatic. Therefore, the extent of homogeneous or partitionless solidification is limited by the reheating of the metal back into the liquid-solid region due to the transformation of latent into sensible heat. As in other metastable effects, the onset of segregation must be characterized by a critical temperature T_C, whose value falls presumably between the solidus and the T_O curve. The production of a homogeneous solid under adiabatic conditions requires then an initial undercooling dictated by the following relationship

$$\Delta H_M \leq \int_{T_N}^{T_C} C_L \, dT \qquad (2.11)$$

where T_N is the temperature of nucleation. The maximum value of T_N that satisfies the above relationship is the "hypercooling" temperature T_H.

The heat transfer to the surroundings is then more important prior to than during solidification. Hirth [74] has estimated the cooling rates necessary for a particle to satisfy Equation (2.11) before the number of nuclei given by Equation (2.2) becomes unity. His calculations show that homogeneous solidification appears feasible for alloys of Fe and Co but not for those of Ni, Cu or Al, under the cooling rates currently achievable in atomization processes. However, these conclusions are questionable since he used the steady state expression for J and considered homogeneous nucleation to occur at the maximum undercoolings reported in the emulsified droplet experiments.

CHAPTER 3

HEAT FLOW ANALYSIS: OVERVIEW

Previous investigations have indicated that the production
of metastable solid structures from the liquid depends on the
achievable interface velocity (or undercooling) during the
solidification process. It is also agreed that for most metals
the flow of latent heat away from the moving interface is the
kinetically rate limiting process, or at least a major component
of it.

During solidification of metal powders, heat is extracted
from the droplets by both convection and radiation at their
surface. Most atomization techniques are characterized by Biot
numbers lower than 0.1, where

$$Bi = hr_0/k_L \qquad (3.1)$$

is the ratio of the surface conductance, or heat transfer
coefficient h, to the metal conductance (k_L/r_0); k_L is the
thermal conductivity of the liquid metal and r_0 is the droplet
radius. It is then concluded that the dominant resistance to
heat flow occurs at the surface, and that no significant
temperature gradients can develop inside the droplet. This
assumption is the basis of the Newtonian model, which has been
used in previous studies on this topic for single-phase cooling

and solidification without undercooling [75,76].

The Newtonian approximation will become less valid as the droplet diameter or the heat transfer coefficient increase, and some numerical simulations have been made in the past to study this effect [77]. Furthermore, its basic assumption of uniform temperature distribution will also lose validity if any substantial undercooling prior to nucleation is achieved in the powders, since the local recalescence of the interface is likely to be faster than the overall recalescence of the droplet.

In dealing with rapid solidification processes it is commonly accepted that two extreme heat flow situations may arise [69]. In the first one the solidification front moves into a superheated liquid, and the heat of fusion must be withdrawn through the solid. Such are the cases of surface melting and splat cooling, where the achievable interface velocities are limited by the rate of heat extraction to the substrate and the thickness of material being processed. The second situation involves solidification into a supercooled melt, where most of the heat of fusion is absorbed by the liquid itself, thereby raising its temperature (recalescing). The external role of heat extraction and the volume of the casting become less relevant during growth, as the interface velocities are now mainly controlled by the melt supercooling.

Since atomization is more limited than surface melting or splat cooling in the achievable rates of heat extraction, it is desirable to reach substantial undercoolings prior to nucleation

in order to enhance the rapid solidification effects. For
example, it is considered that homogeneous solidification can
only be obtained if an amount of enthalpy equivalent to the heat
of fusion is withdrawn from the liquid before solidification
starts [74]. Experimental evidence from this and other
investigations [22,49,50] has shown that large metastable effects
can indeed be obtained under slow cooling conditions by
suppressing the onset of nucleation.

It has also been contended that the external cooling during
atomization may be sufficiently high to partially offset the
recalescence of the droplet and extend the regime of rapid
solidification. Proper assessment of this hypothesis requires a
clear knowledge of the important process variables and their
effects on the thermal history of freezing undercooled droplets.
Unfortunately, previous studies relating heat flow and interface
kinetics have been mainly focused on the growth of dendrite tips
or other curved interfaces into large supercooled melts
[58,66-69] and are difficult to relate to the transient heat flow
conditions inside a powder.

It is then the purpose of this investigation to further
develop our understanding of the thermal history during
solidification of liquid metal droplets. Most of the analysis
will be presented in dimensionless terms, since it tries to
encompass as wide a range of conditions as possible.
Furthermore, general relationships will be developed between the
process variables and the main solidification parameters.

3.1 Parameters

As will be evident later in this work, the most important process variable is the droplet size; values from 0.1 to 1000 μm were considered to cover the typical range of most current laboratory and commercial atomization techniques.

The second important parameter is the combined radiative and convective heat transfer coefficient at the droplet surface, h. Values for h during atomization have been for sometime a matter of uncertainty, since its experimental determination from direct measurements of the heat flow in a moving droplet will be extremely difficult, if not impossible. Nevertheless, it is possible to estimate h from some analytical expressions and other indirect methods.

In gas atomization the convective heat transfer coefficient h_c, is overriding and can be related to other process parameters by the following expression [78]

$$Nu = 2 + 0.6 \sqrt[2]{Re} \sqrt[3]{Pr} \qquad (3.2)$$

where Nu, Re and Pr are the Nusselt, Reynolds and Prandtl dimensionless numbers respectively, given by

$$Nu = (2hr_0)/k_G \qquad (3.3)$$

$$Re = (2r_0 V_\infty)/\nu_G \qquad (3.4)$$

$$Pr = \nu_G/\alpha_G \qquad (3.5)$$

k_G, α_G and ν_G are the thermal conductivity, thermal diffusivity and kinematic viscosity of the gas, respectively, and V_∞ is the particle velocity relative to the gas. Rearranging Equation (3.2) we obtain an expression for the heat transfer coefficient as a function of particle size and velocity

$$h_c = (k_G/r_0) + 0.42 \; [(k_G/ \sqrt[3]{\alpha_G} \; \sqrt[6]{\nu_G})] \; \sqrt[2]{V_\infty/r_0} \qquad (3.6)$$

The first term in this expression represents the contribution from conductive heat transfer when the droplet is cooling in a stagnant gas. Values determined from Equation (3.6) for helium atomization are shown in Table 2, where V_∞ is also expressed as Mach number, or fractions of the velocity of sound (965 m s^{-1} in He).

Table 2

Calculated Heat Transfer Coefficients for Helium Atomization[†]

Mach	V_∞ (m s^{-1})	Droplet Diameter (μm)			
		1	10	100	1000
0	0	5.1×10^5	5.1×10^4	5.1×10^3	5.1×10^2
0.1	97	5.7×10^5	7.1×10^4	1.1×10^4	2.5×10^3
0.3	290	6.2×10^5	8.6×10^4	1.6×10^4	4.0×10^3
0.5	483	6.5×10^5	9.6×10^4	1.9×10^4	5.0×10^3
1.0	965	7.1×10^5	1.1×10^5	2.5×10^4	6.9×10^3

† from Equation (3.6), in Wm^{-2}K^{-1}
droplet is Aluminum at T_M = 933 K, He at 300 K

Analysis of the h_c values in this table reveals that the cooling efficiency is enhanced by reducing the particle size and/or increasing its velocity relative to the gas. However, the contribution of the latter decreases with increasing velocity and is more pronounced in the larger particles. An additional conclusion from this table is that as the particle radius tends to zero the product hr_0, and hence the Biot number, becomes a constant, since the Nusselt number is dominated by the first term of Equation (3.2). It should also be noted that this equation was developed for laminar flow past a sphere and its accuracy when applied to gas atomization has not been tested.

Indirect estimates of heat transfer coefficients in various atomization processes have also been made by comparison of measured segregate (dendrite arm) spacings in crystalline alloy powders with predetermined relationships between these spacings and average cooling rates during solidification, Equation (2.1). The heat transfer coefficients for gas atomization deduced in this way are of the same order of magnitude as those calculated from mathematical expressions [79].

In vacuum (e.g. Electrohydrodynamic) atomization the radiative heat transfer coefficient h_r, is dominant and can be estimated from the following relationship

$$h_r = e \; \sigma \; T_S^4 / (T_S - T_G) \tag{3.7}$$

where e is the surface emissivity, σ is the Stefan Boltzmann constant, T_S and T_G are the droplet and cooling environment temperatures respectively. The cause for uncertainty in Equation (3.7) is the emissivity factor, since values for liquids are usually unknown and values from 0.05 to 0.3 are reported for solid aluminum surfaces in the literature [80]. An h_r of about 80e W m^{-2} K^{-1} can be calculated for for T_S = 933 K and T_G = 300 K.

In general then, the combined radiative and convective heat transfer coefficient may vary between 10 W m^{-2} K^{-1} for the pure radiation case to less than 10^6 W m^{-2} K^{-1} for convection under the most favorable experimental conditions [81]. The limitations on h translate into Biot numbers lower than 1 for most metals and particle sizes of interest. For example, 500 μm droplets of Al, Fe and Ni result in Biot numbers of 0.28, 0.62 and 0.64 for a high heat transfer coefficient of 10^5 W m^{-2} K^{-1}.

The third major parameter is the kinetic relationship between the interface undercooling and velocity. Although models for the different growth mechanisms have been fairly well discussed in the literature [56], their experimental verification has been limited to non-metallic substances [82,83] and a few low melting metals like Ga [84].

The application of the kinetic models discussed in section 2.2.2 involves an assumption of the factor β, whose values may range over two orders of magnitude. Furthermore, data for the self-diffusion coefficient in supercooled liquid metals D_{LM} are

generally unknown, and even values for the superheated liquid are unavailable for Al. For the purposes of this work the following expression will be used

$$D_L = 3.3 \times 10^{-9} \exp(-2.3\Delta T/T) \; m^2 \; s^{-1} \tag{3.8}$$

Equation (3.8) was estimated from the theory of corresponding states [85] using available data on liquid viscosity above the melting point [86].

The exponential and linear laws, Equations (2.4) and (2.5), have been plotted as R/β versus dimensionless undercooling for Al in Figure 1, where it is evident that the latter always dictates higher velocities. The differences between the two models become more pronounced for larger undercoolings, and for $\theta^* < -0.65$ ($\Delta T^* > 240$ K) they predict opposite trends with increasing ΔT^*.

Despite the relative uncertainty in the variables discussed above, it will be shown in the course of this work that the conclusions regarding the general trends and limitations to the effect of heat flow on the solidification process are fairly independent of the numerical values of the individual parameters.

3.2 The Enthalpy-Temperature Diagram

The thermal history of powder solidification can be readily described on the enthalpy temperature diagram shown in Figure 2. This diagram represents graphically the following equation
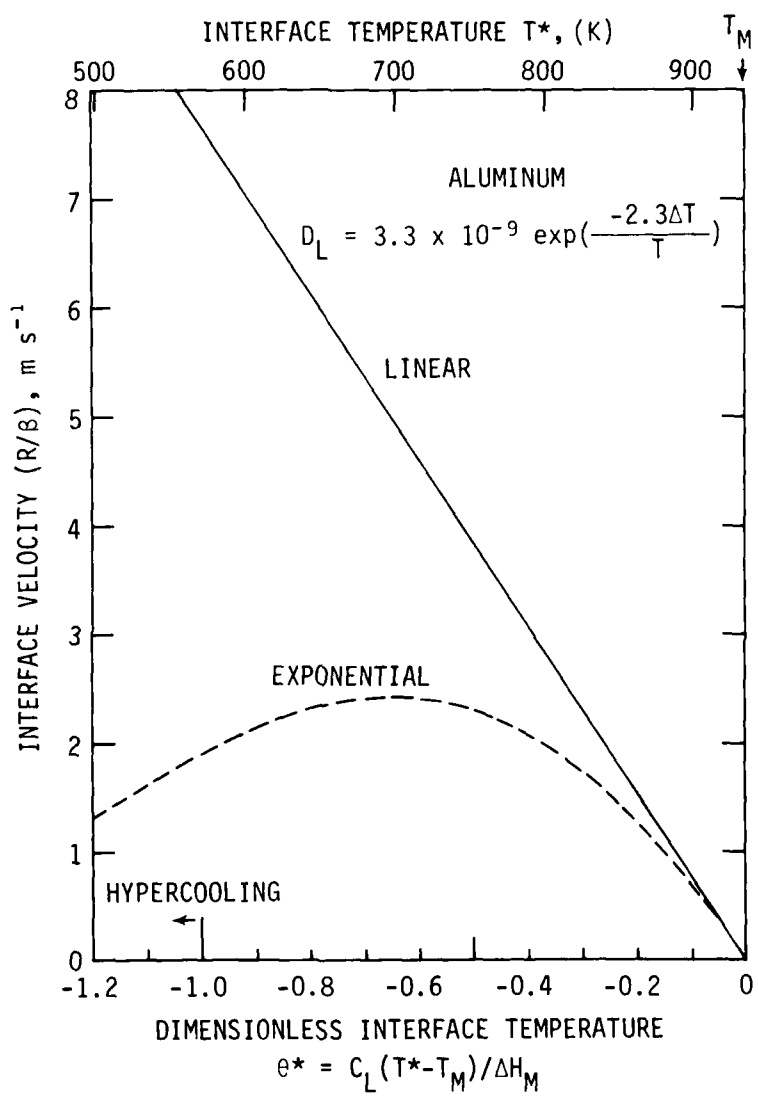
Figure 1. Interface velocity as a function of temperature for the exponential kinetic model and its linear approximation.
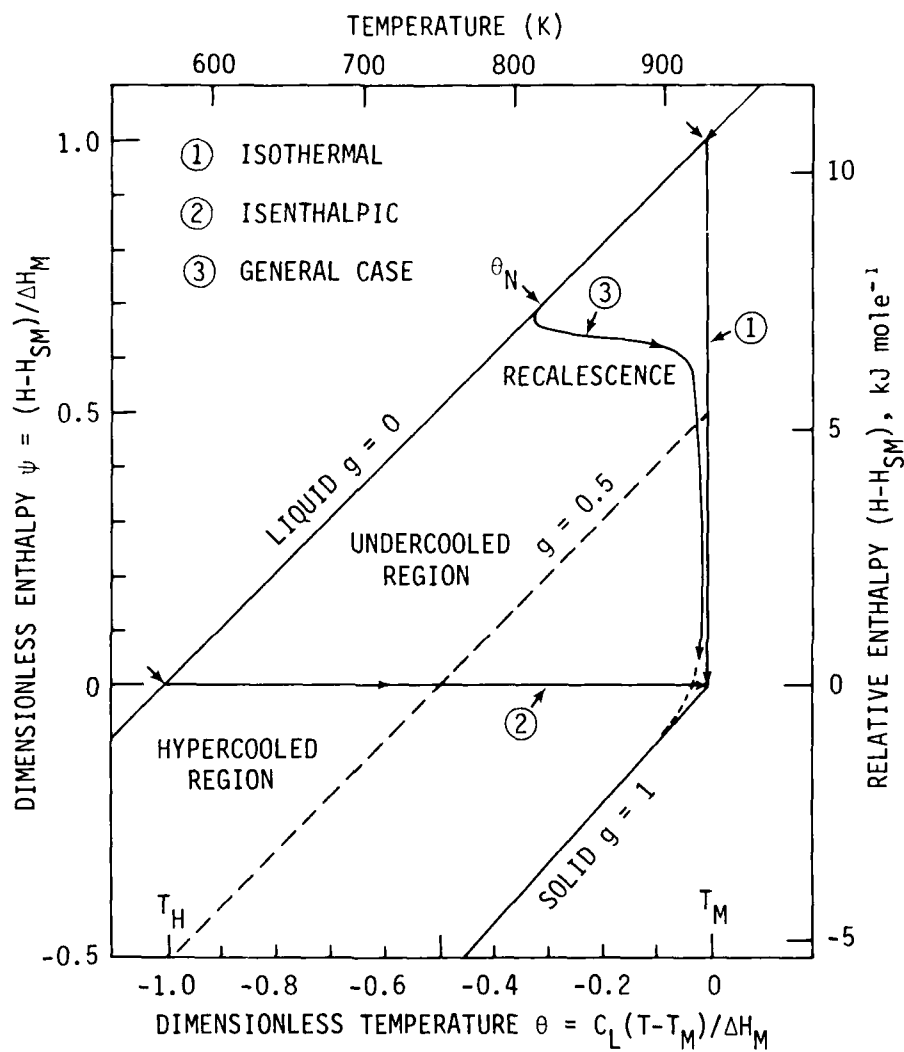
Figure 2. Enthalpy-temperature diagram showing possible solidification paths. θ_N is the dimensionless temperature at the moment of nucleation.

$$(H-H_{SM}) = [\triangle H_M + C_L(T-T_M)](1-g) + C_S(T-T_M)g \qquad (3.9)$$

where H is the enthalpy of the system at temperature T and fraction solid g, above the enthalpy of the solid at the melting temperature H_{SM}, $\triangle H_M$ is the heat of fusion at the melting temperature T_M, C_L and C_S are the specific heats of the liquid and solid respectively. Equation (3.9) can be written in terms of the dimensionless enthalpy ψ and temperature θ as

$$\psi = (1+\theta)(1-g) + (C_S/C_L)\theta g \qquad (3.10)$$

where

$$\psi = (H-H_{SM})/\triangle H_M \qquad (3.11)$$

$$\theta = C_L(T-T_M)/\triangle H_M \qquad (3.12)$$

The two terms on the right hand side of Equation (3.10) represent the enthalpies of the liquid and solid fractions respectively. For a solid volume (g = 1) the dimensionless nodal enthalpy ψ is always negative or zero since $\theta \leq 0$, whereas for a volume of superheated liquid (g = 0, $\theta > 0$) ψ is larger than unity. Since constant fraction solid lines in Figure 2 intersect the melting temperature axis ($\theta = 0$) at $\psi = 1-g$, a volume of partially solid material at T_M will have an enthalpy equal to its fraction of liquid. Note also that the lines of constant g change gradually

in slope $(d\psi/d\theta)$ from 1 at $g = 0$ to C_S/C_L at $g = 1$ (solid).

The system can conceivably follow any path of decreasing enthalpy in the supercooled region ($\psi < 1$) starting at the nucleation temperature ($\theta_N < 0$) on the liquid line, and ending at some point on the solid line. A vertical path represents isothermal solidification, of which a limiting case is the no-undercooling situation (path 1 in Figure 2). A horizontal path represents isenthalpic (or adiabatic) solidification. If nucleation can be suppressed until an amount of enthalpy at least equivalent to the heat of fusion has been removed (i.e. $\psi \le 0$) the system can undergo complete solidification without further heat extraction (path 2 in Figure 2). The region of the diagram for which $\psi \le 0$ is known as "hypercooled". A more realistic path such as that described by curve 3 will be discussed later.

The present investigation will address both undercooling and no-undercooling situations, and numerical models will be developed for each case. The Newtonian model will also be reviewed and extended to use it as a basis of comparison and develop trends for the limiting case where the resistance to heat flow inside the droplet is negligible. Although most of the work is focused on powders coming from a single nucleus, the implications of multiple nucleation, especially when leading to microcrystalline structures, will also be discussed.

CHAPTER 4

PROBLEM STATEMENT AND SOLUTION APPROACH

We consider the cooling of a superheated pure liquid metal droplet and its subsequent solidification due to radially uniform heat loss by radiation and convection from its surface. Surface conductance--heat transfer coefficient--and the temperature of the environment are assumed to remain constant. The thermal properties of the solid and the liquid are considered to be different, but independent of temperature. Heat transfer inside the droplet occurs only by conduction.

First, a complete analysis based on the Newtonian model will be used to develop some general relationships and their trends with changing particle size, heat transfer coefficient, etc. The liquid cooling stage and solidification with and without undercooling will be discussed, both for one nucleation event and massive nucleation cases.

Next, a dimensionless form of the analytical solution to the single-phase, one-dimensional heat conduction equation in spherical coordinates will be used to study the liquid cooling stage and its results compared with the previous Newtonian relationship and trends. It will also be used to determine the temperature profile in the droplet when its surface reaches the prescribed nucleation temperature. This profile is then used as the initial boundary condition for the subsequent solidification problem.

The next chapter involves the numerical analysis of the solidification stage with no undercooling required for nucleation or growth. The concepts of the enthalpy model proposed by Shamsundar and Sparrow [87] are used to develop the solutions for this portion of the problem. In this model the enthalpy is used as a dependent variable in addition to the temperature, and the finite difference equations are written in their fully implicit form. The important variables during cooling and solidification of the droplets are determined and expressed in their most general dimensionless form over a range of Biot numbers of practical interest for droplets of three elements: aluminum, nickel and iron.

Finally the numerical modelling of the solidification of an undercooled liquid droplet from a single nucleation event occurring at the surface will be described. The problem is two-dimensional in nature and has a symmetry axis going from the nucleation point on the surface to its antipode. A modified version of the enthalpy model is developed and the mesh is defined on a superimposed bispherical (rotational bipolar) coordinate system. Since the temperature of each solidifying node, i.e. that containing a portion of the liquid-solid interface, is allowed to depart from the melting point, a kinetic relationship must be added to compensate for this extra degree of freedom in the nodal enthalpy equations. As before, the finite difference equations are written in their fully implicit form and solved by a Gauss Seidel iteration routine. The results are

compared with the equivalent Newtonian case and approximate interface velocities and temperature gradients in front of the liquid solid front are calculated. These last parameters are later discussed in terms of the interface stability theory.

For mathematical consistency, all the dimensionless numbers in the following formulation are written in terms of the properties of the liquid. The values of the thermophysical properties used in the calculation are given in Appendix A.

CHAPTER 5

NEWTONIAN MODEL

The Newtonian or "point source" model assumes that all the resistance to heat flow is concentrated at the surface and therefore no temperature gradients can develop inside the droplet. It is commonly accepted that this model may be applied when the Biot number is lower than 0.1 [78]; however, it will be later shown that this criterion may not be always satisfactory in powder solidification.

According to the Newtonian model, the thermal history of a cooling droplet can be described by

$$(d\psi/dFo) = -3 \ Bi \ (\theta + Ste) \tag{5.1}$$

where ψ and θ are the dimensionless enthalpy and temperature respectively, Fo is the Fourier number or dimensionless time,

$$Fo = \alpha_L t/r_0^2 \tag{5.2}$$

and Ste is the Stefan number,

$$Ste = C_L \ (T_M - T_G)/\Delta H_M \tag{5.3}$$

which is equivalent to the dimensionless temperature of the

cooling environment with opposite sign.

5.1 Liquid Cooling Stage

For single phase cooling the rate of enthalpy change in the liquid is given by

$$(d\psi/dFo) = (d\theta/dFo) \tag{5.4}$$

(for the solid phase cooling the right hand side is multiplied by the ratio of solid to liquid specific heats C_S/C_L). Combining Equations (5.1) and (5.4) produces an expression for the actual instantaneous cooling rate

$$\epsilon = 3 \; (\alpha_L/k_L) \; (h/r_0) \; (T - T_G) \tag{5.5}$$

where r_0 is the droplet radius, T and T_G are the liquid and cooling environment temperatures respectively. The sign of the temperature derivative has been changed so that ϵ is positive for $T > T_G$.

Equation (5.5) can be now readily integrated to yield an expression for the cooling time, i.e. the time it takes for the droplet to cool from an initial temperature T_0 ($\theta_0 > 0$) to the prescribed nucleation temperature T_N ($\theta_N < 0$)

$$Fo_N = \ln[(\theta_0 + Ste)/(\theta_N + Ste)] \; / \; 3Bi \tag{5.6}$$

$$t_N = (k_L/3\alpha_L) \ (r_0/h) \ \ln[(T_0 - T_G)/(T_N - T_G)] \qquad (5.7)$$

The above equations give the cooling time dependence on the process parameters in dimensionless and dimensional forms respectively.

In general, Equations (5.5) to (5.7) indicate that decreasing the droplet radius by one order of magnitude will proportionally increase the cooling rate and decrease the cooling time. Increasing the heat transfer coefficient h will have the same effect.

5.2 Solidification without Undercooling

For isothermal solidification at the melting point ($\theta = 0$) the rate of enthalpy change is

$$-(d\psi/dFo) = (dg/dFo) = 3 \ Bi \ Ste \qquad (5.8)$$

where (dg/dFo) is the dimensionless solidification rate. This equation can be readily integrated to yield the expressions for the dimensionless and dimensional solidification times

$$Fo_f = (3 \ Bi \ Ste)^{-1} \qquad (5.9)$$

$$t_f = [\Delta H_M \rho/3(T_M - T_G)] \ (r_0/h) \qquad (5.10)$$

where T_M is the melting temperature, ΔH_M and ρ are the heat of fusion and density of the material respectively.

Equations (5.8) to (5.10) indicate that the solidification rate and time depend on r_0 and h in the same way as the cooling rate and time discussed above.

The Newtonian model per se does not imply any particular geometry for the liquid solid interface. Nevertheless, one could conceivably calculate interface velocities from this model by prescribing such a geometry. Manipulation of Equation (5.8) shows that, in general, the dimensionless ($\underline{R}$) and dimensional (R) interface velocities can be written as

$$\underline{R} = (r_0/\alpha_L) \; R = Bi \; Ste \; g' \qquad (5.11)$$

$$R = [(T_M - T_G)/\rho\Delta H_M] \; h \; g' \qquad (5.12)$$

where g' is a geometric factor solely dependent on the fraction solid. Therefore, given a fixed growth geometry, the Newtonian interface velocity at a certain fraction solid is insensitive to changes in the droplet radius and can only be increased by increasing the heat transfer coefficient or lowering the cooling environment temperature.

It is evident from Equation (5.11) that the calculated velocities will be strongly dependent on the shape asigned to the interface. For example, if the interface is concentric with the droplet surface (concentric geometry in Figure 3) the

CONCENTRIC GEOMETRY
INTERFACE MOVES
TOWARD CENTER $\phi = 0$

AXISYMMETRIC GEOMETRY
INTERFACE MOVES FROM
$Z^* = -1$ TO $Z^* = 1$
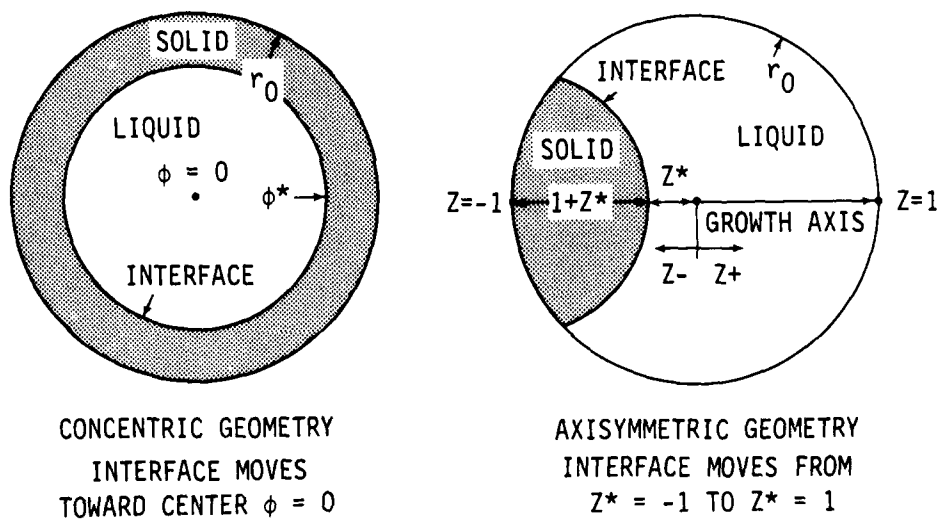
Figure 3.   Interface geometries used for the cases of
no-undercooled (concentric) and undercooled
(axisymmetric) solidification.

dimensionless interface velocity $\underline{R}$ is given by

$$\underline{R} = (d\phi^*/dFo) = Bi\ Ste\ \{(\phi^*)^{-2}\} \tag{5.13}$$

where ϕ^* is the dimensionless radial position of the liquid solid front $(0 < \phi^* < 1)$. However, if the interface is spherical in shape, with its center of curvature on the droplet surface (axisymmetric geometry in Figure 3) the dimensionless interface velocity is now

$$\underline{R} = (dZ^*/dFo) = Bi\ Ste\ \{4/[2(1+z^*)^2-(1+z^*)^3]\} \tag{5.14}$$

where Z^* is the dimensionless position of the solid front along the axis of symmetry for both spheres, henceforth called the growth axis $(-1 < Z^* < 1)$.

Normalized forms of Equations (5.13) and (5.14) are plotted in Figure 4, showing that quite different results may be obtained simply by assuming two different growth geometries. For example, at a fraction solid g = 0.1 the velocity predicted from the concentric pattern is 3.5 cm s^{-1} whereas that obtained from the axisymmetric geometry is 23.3 cm s^{-1} for Al droplets of any size ($h = 5 \times 10^4$ W m^{-2} K^{-1}, T_G = 300 K). It should also be noted that this figure is independent of the metal properties.
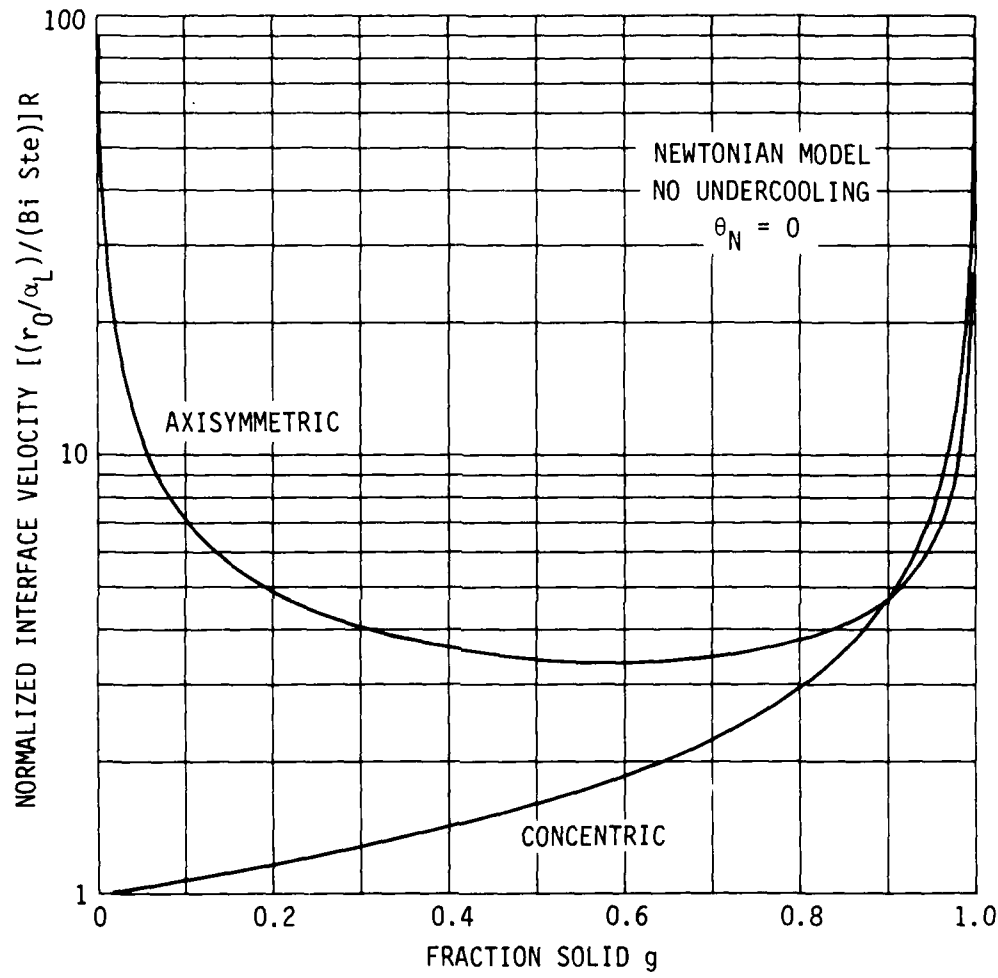
Figure 4. Normalized interface velocity as a function of fraction solid for Newtonian solidification without undercooling. Note that the values in the ordinate are equivalent to g´ in Equation (5.11) and therefore independent of the material.

5.3 Solidification with Undercooling

When a liquid droplet is substantially undercooled prior to nucleation, the solidification process cannot be assumed isothermal and the system acquires one more degree of freedom. Although the thermal history must still follow Equation (5.1), the problem cannot be easily solved analytically and a numerical approach is required.

5.3.1 Mathematical formulation

Equation (5.1) can be written in implicit finite difference form as follows

$$\psi_{k+1} + 3Bi\Delta Fo\ \theta_{k+1} = \psi_k - 3Bi\Delta Fo\ Ste \qquad (5.15)$$

where the subscripts k and k+1 indicate the previous and current time steps respectively, separated by an interval ΔFo. From the definition of enthalpy given by Equation (3.10) we obtain

$$\psi_{k+1} - (1+\Delta Cg_{k+1})\ \theta_{k+1} = 1 - g_{k+1} \qquad (5.16)$$

where

$$\Delta C = (C_S - C_L)/C_L \qquad (5.17)$$

Combining Equations (5.15) and (5.16) produces the basic

relationship of the Newtonian model for undercooled solidification:

$$(1+3Bi\Delta Fo)\theta_{k+1} + (\Delta C\theta_{k+1}-1)g_{k+1} - (\psi_k-1-3Bi\Delta FoSte) = 0 \qquad (5.18)$$

In order to solve this equation as a function of time we require a kinetic relationship between g and θ to account for the extra degree of freedom introduced in non-isothermal solidification. Since the kinetic models relate the undercooling to linear displacements, it is necessary to specify the number of nucleation events and the liquid-solid interfacial geometry to translate these displacements into changes of the fraction solid. If we assume that no temperature gradients exist in the droplet, and neglect any orientation dependence of the growth rate, the interface should preserve the original nucleus geometry.

In this section we will first develop the model for a single nucleation event and later approach the problem of massive nucleation that leads to a microcrystalline structure.

5.3.1.1 Single nucleation event

We now consider a nucleation event in the form of a spherical cap occurring at the droplet surface. The interface follows the axisymmetric geometry depicted in Figure 3. The fraction solidified is given by

$$g = 0.5(1+z^*)^3 - 0.1875(1+z^*)^4 \qquad (5.19)$$

where $(1+z^*)$ is the distance solidified along the growth axis.

For any kinetic expression, the interface position is

$$z_{k+1}^* = z_k^* + \underline{R}(\theta) \; \Delta Fo \qquad (5.20)$$

where $\underline{R}(\theta)$ is the temperature dependent dimensionless interface velocity. Substituting the above equation into (5.19) and rearranging, we obtain the relationship between g and θ which is of the form

$$g_{k+1} = \sum_{p=0}^{p=4} Y_p \; [\underline{R}(\theta)]^p \qquad (5.21)$$

where the coefficients Y_p are only functions of the time interval ΔFo and the interface position in the previous time step z_k^*.

5.3.1.2 Massive nucleation

For the simulation of the microcrystalline solidification we choose an array of close packed dodecahedral grains, each one originating from a spherical nucleus. If the spacing between two nearest neighbors is d_{MX}, the approximate number of grains in a droplet of radius r_0 is

$$N = (\pi/3\sqrt{2}) \; (2r_0/d_{MX})^3 \qquad (5.22)$$

Assuming that the spherical solid grows concentrically within the dodecahedral liquid volume, the fraction solid is given by

$$g = (\pi/\sqrt[3]{2}) \ (z^*/3) \qquad\qquad 0 \le z^* \le 1 \qquad (5.23)$$

$$g = (\pi/\sqrt[3]{2}) \ [-(5/3)(z^*)^3 + 3(z^*)^2 - 1] \qquad 1 \le z^* \le 2/\sqrt[3]{3} \qquad (5.24)$$

where z^* is now the distance between the interface and the nucleation point normalized by half the grain spacing d_{MX}.

Equation (5.23) applies when the spheres are growing freely inside the dodecahedra. Equation (5.24) applies from the moment when two neighbor spheres touch ($z^* = 1$) until 3 spheres touch and start forming a corner ($z^* = 2/\sqrt[3]{3}$). At this moment the value of g is approximately 0.96. *Since the mathematical expressions for the rest of the solidification problem are rather complex, the analysis was terminated at this point.*

The interfacial displacements are given in this case by

$$z^*_{k+1} = z^*_k + (2r_0/d_{MX}) \ \underline{R}(\theta) \ \Delta Fo \qquad (5.25)$$

which combined with Equations (5.23) or (5.24) yields an expression similar to (5.21)

$$g = \sum_{p=0}^{p=3} [(2r_0/d_{MX}) \ Y'_p] [\underline{R}(\theta)]^p \qquad (5.26)$$

where the coefficients Y_p' are only functions of Fo and the value of z_k^*.

Equation (5.18) can be solved with the aid of Equations (5.21) or (5.26) for the single and massive nucleation cases respectively, using a Newton-Raphson technique at each time step, starting with $_N$ as the initial condition. Calculations were performed with both the linear and exponential laws defined in Chapter 2. The solution procedure was set for an adjustable time increment to produce roughly uniform displacements of the liquid-solid interface.

Before entering the description of the results, it should be emphasized that the inherent assumption of Newtonian conditions during solidification precludes temperature gradients in the droplet. Therefore, no distinction can be made between droplet and interfacial temperature, and the motion of the solid front will be dictated by the overall undercooling.

5.3.2 Results and discussion

The general shape of the enthalpy-temperature (ψ-θ) curve has been sketched in Figure 2 (case 3) where two distinct solidification regimes can be identified. The first one is the recalescence or "rapid solidification" stage, where the supercooled droplet is absorbing most of the liberated heat of fusion and the heat loss to the surroundings is more or less irrelevant. The second regime is one of a slower growth, and

develops after the droplet undercooling has been largely
relieved, therby limiting the progress of solidification to the
conditions imposed by the external heat flow. This regime
usually involves temperatures close to the melting point of the
material and is roughly isothermal.

The thermal history reflects the competition between the
external rate of heat extraction and the recalescence rate
(release of latent heat) which is proportional to the
solidification rate (change in fraction solid with time, dg/dt).
The latter is in turn a product of the liquid solid interface
velocity times its area. Predominance of the recalescence rate
translates into a shallow negative slope. As the heat extraction
process is able to relieve some of the heat of fusion being
transformed into sensible heat, the slope of the curve becomes
steeper (more negative) and eventually positive if the heat flow
is dominant.

In addition to the two regimes noted above, there is usually
an initial transient in the ψ-θ curve, during which time the
cooling rate decreases rapidly from the liquid value at the
moment of nucleation until it changes sign and the overall
recalescence begins. At the start of solidification the velocity
is finite but the interfacial area is very small, and so is the
solidification rate. Therefore, the rate of heat extraction
dominates the rate of recalescence and the droplet temperature
drops further below θ_N. There is also a final transient, of
increasing cooling rate, due to the same competitive process.

If we consider that the enthalpy is only a function of the temperature and fraction solid, then

$$(d\psi/d\theta) = (\partial\psi/\partial\theta)_g + (\partial\psi/\partial g)_\theta \, (dg/d\theta) \tag{5.27}$$

and from Equation (3.10)

$$(\partial\psi/\partial\theta)_g = 1 + \Delta C \, g \tag{5.28}$$

$$(\partial\psi/\partial g)_\theta = \Delta C \, \theta - 1 \tag{5.29}$$

Equation (5.27) can also be written as

$$(d\psi/d\theta)[1-(\partial\psi/\partial g)_\theta (dg/dZ^*)(dZ^*/d\psi)] = (\partial\psi/\partial\theta)_g \tag{5.30}$$

dZ^* and $d\psi$ are given respectively by

$$dZ^* = \underline{R} \, dFo \tag{5.31}$$

$$d\psi = -3 \, Bi \, (\theta + Ste) \, dFo \tag{5.32}$$

Combining Equations (5.28) to (5.32) we obtain

$$(d\psi/d\theta)\{1+[(\Delta C\theta+1)/3(\theta+Ste)](dg/dZ^*)(\underline{R}/Bi)\}-1-\Delta Cg = 0 \tag{5.33}$$

Since the interface velocity $\underline{R}$ can be written in its general form as

$$\underline{R} = K \; \phi(\theta) \tag{5.34}$$

where K is a dimensionless kinetic coefficient at the melting point, and $\phi(\theta)$ is a function of temperature. K is related to the actual kinetic parameter K_M (i.e. the constant relating velocity and undercooling in the linear law, Equation (2.5)) by

$$K = (r_0/\alpha_L) \; (\Delta H_M/C_L) \; K_M \tag{5.35}$$

$$K_M = \beta(D_{LM}/\delta) \; (\Delta H_M/R' T_M^2) \tag{5.36}$$

Equation (5.33) can now be written as

$$(d\psi/d\theta)\{1+[(\Delta C\theta+1)/3(\theta+Ste)](dg/dZ^*)(K/Bi)\phi(\theta)\}-1-\Delta Cg = 0 \tag{5.37}$$

Since both K and Bi contain an r_0 factor, their ratio is independent of particle radius. In addition, (dg/dZ^*) is only a function of g for a fixed interfacial geometry. Therefore, the $\psi-\theta$ path described by the integration of Equation (5.37) is also independent of particle size. The only effect of r_0 is to increase or decrease proportionally the time scale of the process.

For a particular solidification geometry (e.g. concentric), the thermal history and the interface velocity at a given fraction solid are only functions of the initial temperature θ_N, and the dimensionless ratio K/Bi. This latter parameter measures the degree of predominance of the recalescence rate over the rate of heat loss to the environment. Appropriate substitution of the variables in Equation (5.36) yields an expression for the K/Bi ratio in terms of β and h, which is used throughout the calculations

$$(K/Bi) = 2 \times 10^7 \ (\beta/h) \tag{5.38}$$

Kinetic considerations generally limit β to within 1 and 10^2, while the heat transfer coefficients during atomization range from a minimum of 10 to about 10^6 W m^{-2} K^{-1}. Consequently, the parameter K/Bi can vary from about 20 to 2×10^8.

For the case of massive nucleation a third parameter, the ratio $2r_0/d_{MX}$ (or the number of grains), will appear in Equation (5.33) multiplying $\underline{R}$.

5.3.2.1 Solidification from a single nucleation event

Figure 5 shows the effect of the initial undercooling on the enthalpy-temperature curve for a constant K/Bi = 100, considering both linear and exponential kinetics. It is evident that increasing the undercooling prior to nucleation results in a
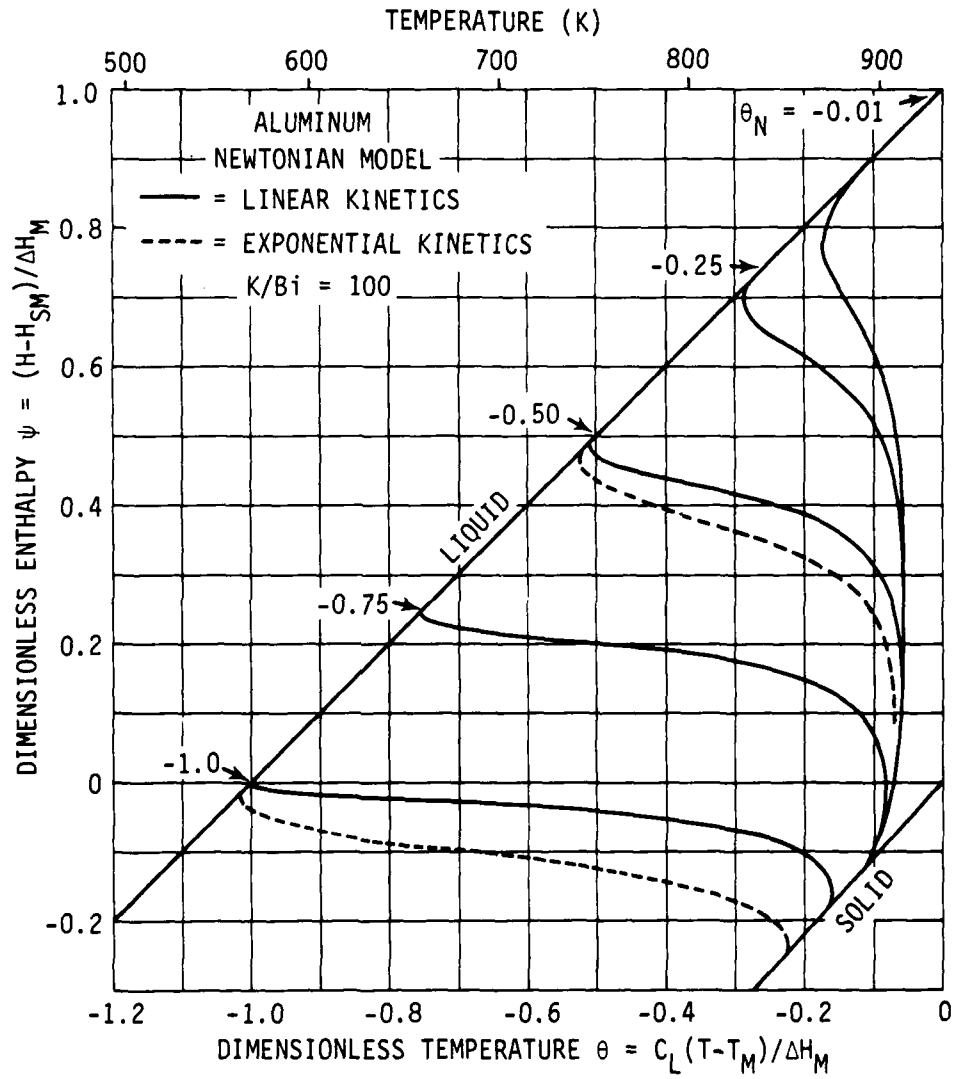
Figure 5. Effect of the nucleation temperature on the thermal history of undercooled droplets calculated from the Newtonian model.

corresponding increase in the solidification rate, thus reducing the initial transient and the relative contribution of the external heat extraction. The latter is also diminished due to the smaller temperature differences between the droplet and its environment. In addition, this figure also shows that the "slow growth" regime is gradually suppressed as θ_N decreases (or as fraction solid at the end of recalescence increases towards one).

Changing the kinetic model from linear to exponential (slower), has the effect of slightly extending the "rapid solidification" regime, as shown in Figure 5. This follows from a reduction in the solidification and recalescence rates due to the lower interface velocities predicted by the exponential law, therby enhancing the role of heat loss to the environment. The differences between the two models increase with undercooling, as expected from Figure 1.

The dependence of the thermal history on the ratio K/Bi for a constant initial temperature $\theta_N = -0.5$ ($\Delta T_N = 182$ K) is shown in Figure 6. Curves for K/Bi > 10^3 closely approach the limiting case of adiabatic (isenthalpic) rapid solidification followed by an isothermal slow growth regime at the melting temperature. As K/Bi decreases (slower kinetics or more efficient cooling), the curves show an increasing contribution of the heat extraction rate during recalescence. At the extreme, e.g. K/Bi=10, the regime of "rapid solidification" is extended to a point where the droplet temperature never goes beyond its initial value θ_N. However, even for a low kinetic coefficient $K_M = 2$ cm s^{-1} K^{-1}
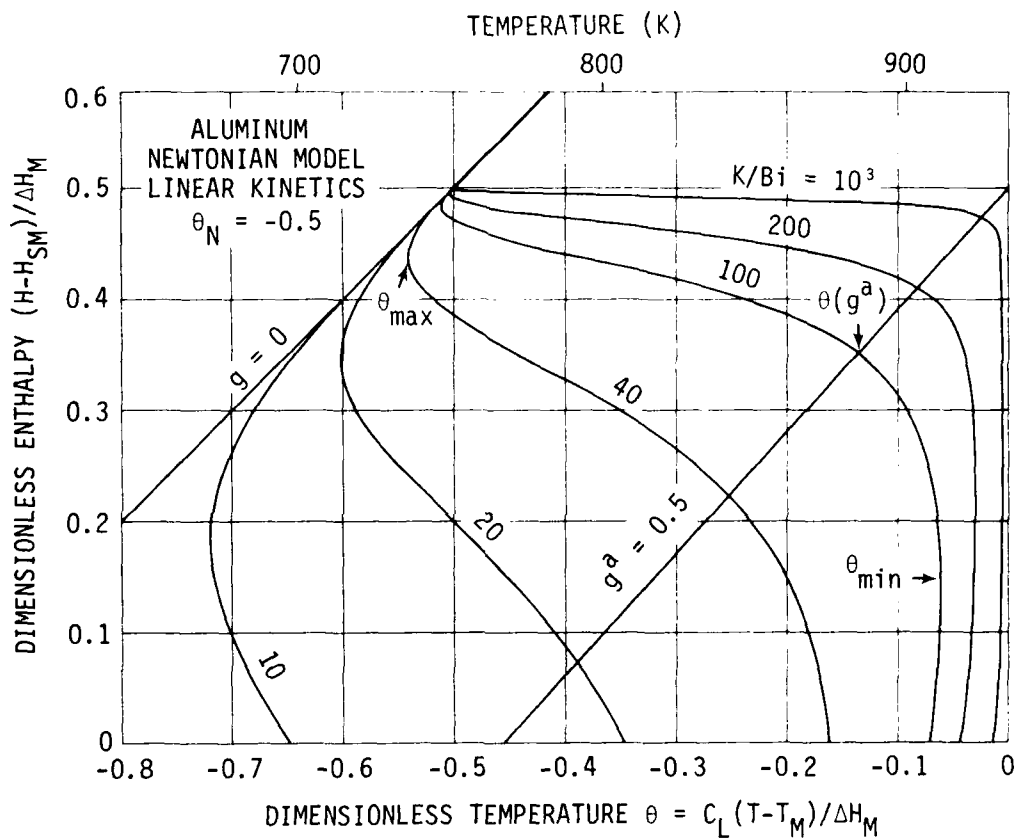
Figure 6. Effect of the ratio K/Bi on the thermal history of undercooled droplets for a fixed nucleation temperature. Note that for typical atomization conditions (K/Bi>100) the external cooling is not able to slow down recalescence to a significant extent.

(β=1), the heat transfer coefficient would have to be about 2×10^6 W m^{-2} K^{-1} in order to produce this effect. For a higher β such as the value of 100 suggested by Cahn et al. [56], we would require an h = 2×10^8 W m^{-2} K^{-1}, which is clearly above the typical values encountered in atomization.

Three characteristic undercooling values can be distinguished in the $\psi-\theta$ curves (see Figure 6)

a) The maximum undercooling at the end of the initial transient, ΔT_{max} (or θ_{max}). This parameter is of small importance since θ_{max} is close to θ_N for typical atomization conditions, i.e. K/Bi > 100.

b) The minimum undercooling, ΔT_{min} (or θ_{min}), corresponding to the "nose" that every $\psi-\theta$ curve exhibits after the recalescence regime. This point represents the maximum temperature reached by the droplet during solidification, where the external rate of heat extraction becomes again the dominant process, and changes the slope of the curve from negative to positive. If a certain metastable effect requires a critical undercooling ΔT_C during growth, the "nose" of the recalescence curve should always have a $\Delta T_{min} > \Delta T_C$.

c) The undercooling in the droplet at a given fraction solid $\Delta T(g)$ or $\theta(g)$. In the limiting case of adiabatic solidification (K/Bi$\rightarrow\infty$), the undercooling at the end of recalescence is zero and the fraction solidified is $g^a = -\theta_N$. The effect of heat extraction during

recalescence (finite K/Bi) can then be assessed by comparing the values of $\Delta T(g^a)$. The ratio of $\Delta T(g^a)/\Delta T_N$ indicates the fraction of the initial undercooling still present in the droplet when $g = g^a$, and therefore is a measure of how efficiently the external cooling is able to slow down the reheating process.

Table 3

Effect of the K/Bi Ratio on the Characteristic
Undercoolings of the Enthalpy-Temperature Curve (K) [†]

K/Bi	Linear		Exponential	
	$\Delta T(g^a)$	ΔT_{min}	$\Delta T(g^a)$	ΔT_{min}
10^2	51	23	65	26
200	31	11	38	12
400	18	5.4	22	5.4
1600	6.3	1.3	7.3	1.3
10^4	1.5	0.21	1.6	0.21
10^6	0.004	0.002	0.078	0.002

† $\angle T_N = 182$ K, $h = 5 \times 10^4$ $Wm^{-2}K^{-1}$, $K_M = 2$ $cms^{-1}K^{-1}$

Table 3 shows the characteristic ΔT values as a function of K/Bi for both the linear and exponential kinetic models. The results indicate that even for a very low K/Bi like 100, the heat flow can only produce an undercooling $\Delta T(g^a) = 65$ K. This means that about one third of the liberated heat of fusion may be lost to the environment before the droplet reaches a fraction solid of $g^a = 0.5$. One can then conclude from the Newtonian analysis that

the external cooling has little influence on the thermal history of the droplet during recalescence.

A further conclusion from Figures 5 and 6 is that the K/Bi ratio is more influential in shifting the "nose" of the $\psi-\theta$ curve than the initial undercooling θ_N. If ΔT_C is relatively small rapid solidification effects may be obtained throughout the droplet with moderate ΔT_N, provided the value of K/Bi is sufficiently small to keep ΔT_{min} above ΔT_C. However, if ΔT_C is large, the extent of rapid solidification will be essentially limited by the undercooling prior to nucleation.

Although the thermal history is uniquely defined for a given θ_N and K/Bi, (i.e., the undercooling is fixed for every fraction solid), the Newtonian interface velocities depend on the specific values of K_M, h and the prescribed kinetic model. This is due to the assumption of infinite heat conductance inside the droplet, making the interface motion independent of the thermal field in its vicinity. For the Newtonian case, then, the interface will move as fast as the overall undercooling of the droplet allows it to go, rather than adjust its undercooling to comply with the heat flow conditions around it.

The assumption of an axisymmetric solidification geometry influences the calculated growth rates, as previously discussed for the case of no undercooling. In order to isolate the geometric effects from those imposed by the kinetics and heat flow conditions, a normalized interface velocity is defined as the ratio of undercooled (R_U) to the no undercooled (R_{NU})

interface velocities for the same fraction solid g. This ratio is independent of particle size, as shown before, as well as of the kinetic coefficient K_M, making it a single valued function of g for constant θ_N and K/Bi.

Figure 7 shows the effect of θ_N on the normalized interface velocity for a fixed K/Bi = 10^3, whereas Figure 8 describes the effect of K/Bi for a constant $\theta_N = -0.5$. The curves in these figures consist of a "hump" where $R_U >> R_{NU}$ reflecting the undercooling driven velocity, and the flat portion where $R_U \cong R_{NU}$ characteristic of the heat flow driven velocity. The initial and final transients are geometric effects since the no-undercooling model predicts infinite velocities at the beginning and at the end of solidification (see Figure 4) but the kinetics will limit the interfacial motion. It should be emphasized that these velocities will only be meaningful if Newtonian conditions are fulfilled. Results of the Enthalpy model for undercooled solidification, discussed in Chapter 8, reveal that substantial temperature differences during recalescence may arise in the droplet even for Bi numbers as low as 10^{-4}. Therefore, care should be exercised in using the Newtonian model for rapid solidification of undercooled metals. Better guidelines are necessary to determine its applicability, since compliance with the condition of Bi < 0.1 does not seem to be a satisfactory criterion.

The dependence of the solidification times on the K/Bi ratio for a linear kinetic model and different nucleation temperatures
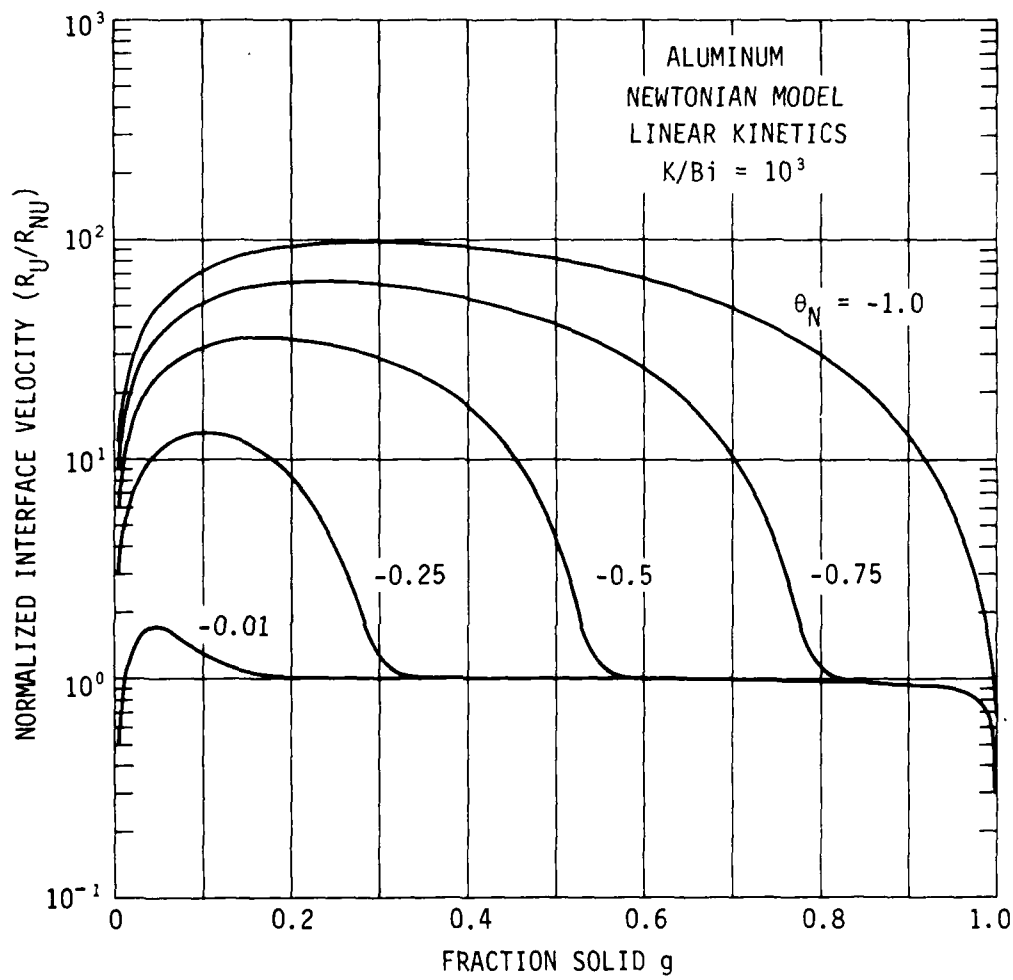
Figure 7. Normalized interface velocity for undercooled
Newtonian solidification, as a function of fraction
solidified and nucleation temperature. When
$R_U/R_{NU} = 1$ the interface motion is solely controlled
by the heat flow.
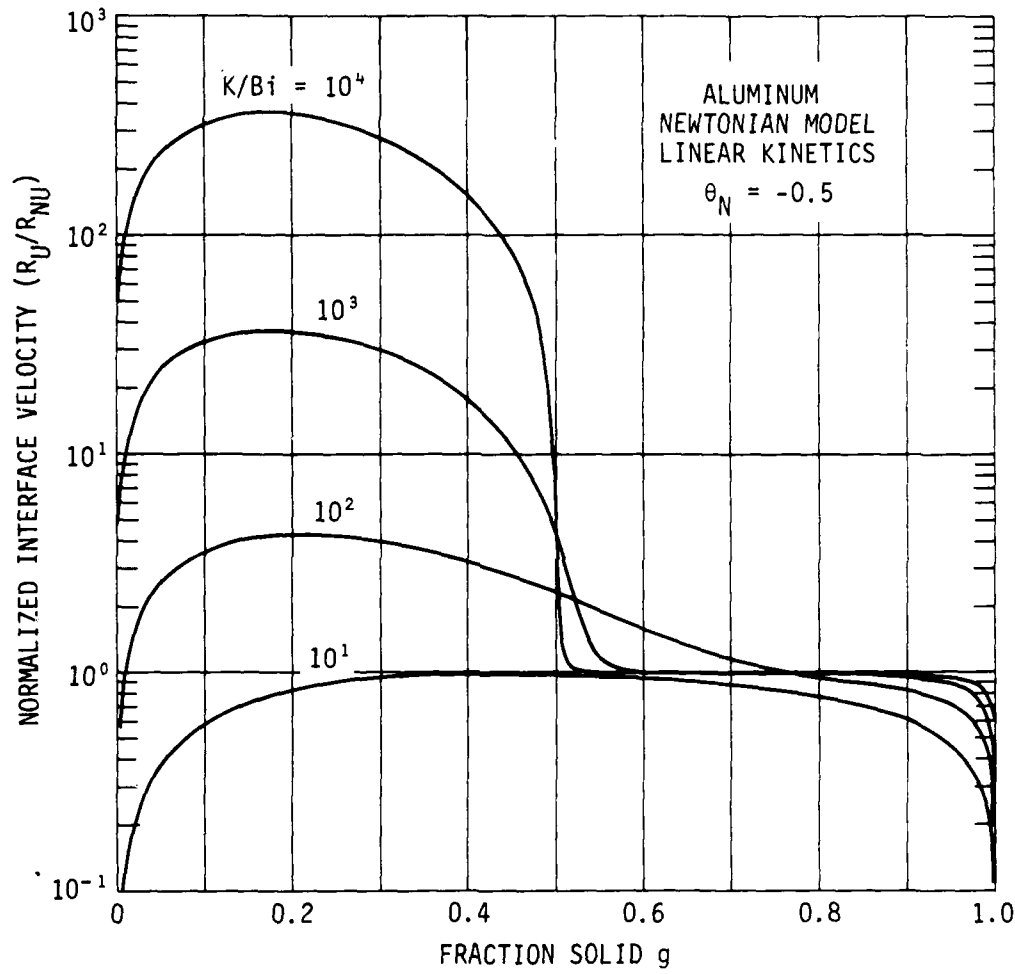
Figure 8. Normalized interface velocity for undercooled
Newtonian solidification, as a function of fraction
solidified and (K/Bi). Note that for K/Bi>10³ the
interface falls under pure heat flow control shortly
after g surpases the adiabatic value $g^a = -\theta_N$.
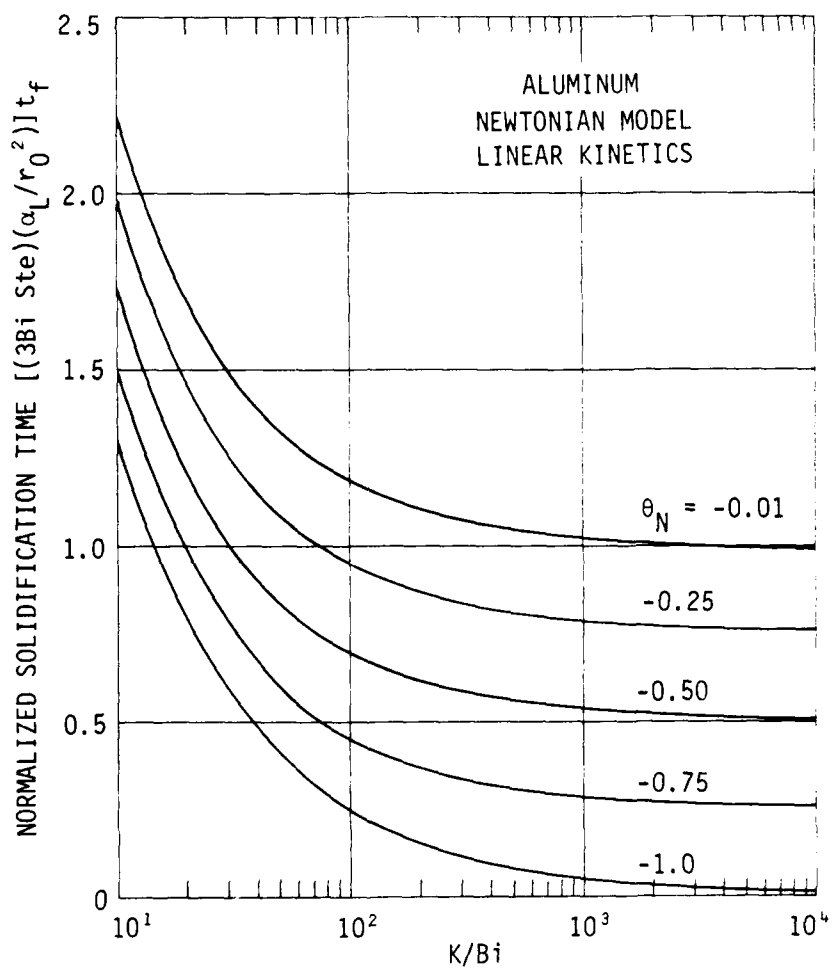
Figure 9. Normalized solidification time as a function of K/Bi and initial undercooling. This plot is independent of particle radius and the particular values of K_M and h.

is presented in Figure 9. The calculated times have been
normalized by the solidification time for a no-undercooled
situation, $(t_f)_{NU}$ given by Equation (5.10), making the plotted
values independent of particle size and the individual values of
K and Bi. The effect of an exponential kinetic model would be to
shift the curves to the right (higher time values) but it is only
noticeable in the low range of K/Bi ($<10^2$) and high
undercoolings.

Figure 9 shows that as K/Bi increases the curves approach
asymptotically the value predicted from the limiting case of
adiabatic solidification

$$(t_f)_U = (1 - g^a) \ (t_f)_{NU} \qquad (5.39)$$

which implies an instantaneous recalescence after nucleation. As
the rate of the heat flow increases (K/Bi is reduced) the time
values become larger than those predicted by Equation (5.39).
Examples of calculated solidification times for 5 μm Al droplets
are reported in Table 4. Increasing r_0 will proportionally
increase the values in this table.

Table 5 shows the effect of the nucleation temperature on
the overall time scale. Although the solidification time
decreases with larger undercoolings, this reduction is offset by
a corresponding increase of the cooling time (i.e. the time
spent in the liquid state before reaching the nucleation
temperature). Therefore, the time it takes to form a solid

powder from a liquid droplet at or above its melting temperature increases with increasing undercooling prior to nucleation. This is a significant observation in determining whether the flight time available in a given atomizer will be sufficient for complete solidification.

Table 4

Solidification Times for 10 μm Aluminum Droplets (μs)

K_M	h	$(t_f)_{NU}$	Nucleation Temperature θ_N		
$(cms^{-1}K^{-1})$	$(Wm^{-2}K^{-1})$	(μs)	−0.01	−0.5	−1.00
2	2×10^5	12.8	15.2	8.9	3.2
2	10^5	25.6	28.3	15.7	3.9
2	5×10^4	51.2	54.2	29.1	4.8
8	5×10^4	51.2	51.9	26.9	1.8
50	5×10^4	51.2	51.0	25.9	0.5

Table 5

Effect of the Nucleation Temperature
on the Time Scale (μs) [†]

θ_N	t_f	t_N	$t_N + t_f$
0	51.2	−	51.2
−0.01	54.2	0.5	54.7
−0.25	41.9	13.8	55.7
−0.50	29.1	30.2	59.3
−0.75	16.3	50.3	66.6
−1.00	4.8	103.7	108.5

[†] $2r_0 = 10$ μm, $T_0 = T_M$

$h = 5 \times 10^4$ $Wm^{-2}K^{-1}$, $K_M = 2$ $cms^{-1}K^{-1}$

5.3.2.2 Solidification from massive nucleation

The net effect of increasing the number of nucleation events (or $2r_0/d_{MX}$) manifests itself as an apparently higher K/Bi due to the increase in the interfacial area, which in turn increases the solidification rate (dg/dt). Therefore, the thermal history is now dependent on θ_N and the product $(2r_0/d_{MX})(K/Bi)$ and must be unique as long as these parameters remain constant. It should be noted that every twofold increase in $2r_0/d_{MX}$ translates into an eight-fold increase in the number of grains.

Figure 10 shows the enthalpy-temperature curves for a fixed $\theta_N = -0.5$ and several values of the product $(2r_0/d_{MX})(K/Bi)$. If one takes a low K/Bi value of 50 (e.g. $K_M = 2$ cm s^{-1} K^{-1} and $h = 4 \times 10^5$ W m^{-2} K^{-1}) these curves will represent the thermal histories of droplets with 1, 8, 64 and 1000 nucleation events respectively. As expected, increasing the number of grains reduces the role of the heat transfer during recalescence, and consequently the extent of the "rapid solidification" regime. However, the occurrence of multiple nucleation does not have a critical effect at values of K/Bi > 10^3 because the role of the heat flow is already small even for solidification from a single nucleus.

Although numerical calculations for this case were not performed due to the geometrical complexity of the problem, it is anticipated that the validity of the Newtonian approximation is enhanced as the number of nuclei increases. This is due to the
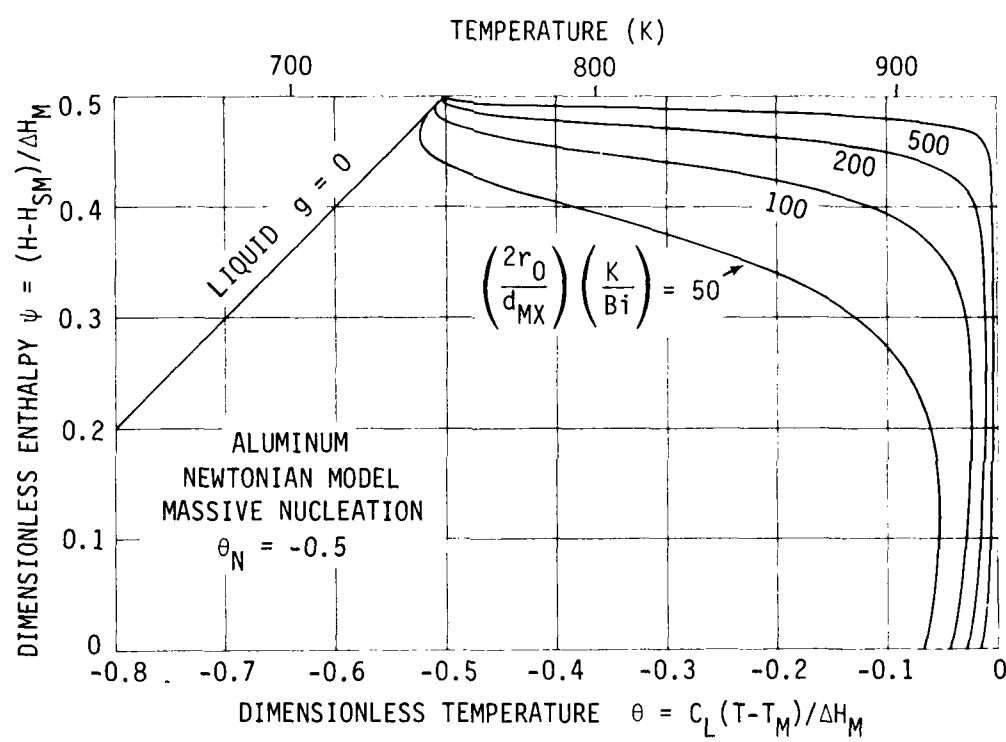
Figure 10. Effect of the number of nucleation events on the
thermal history of undercooled droplets solidifying
under Newtonian conditions.

reduction in the scale of the heat transfer problem (from r_0 to $d_{MX}/2$) which hinders the development of temperature differences inside the droplet. Furthermore it is expected that other solidification morphologies which increase the liquid solid interfacial area (and therefore dg/dt) such as dendritic vs. plane front structures, should have an effect on the thermal history similar to the occurrence of multiple nucleation.

CHAPTER 6

LIQUID COOLING STAGE: NON-NEWTONIAN SOLUTION

The following section is devoted to the analysis of the pre-solidification period allowing for a non-uniform temperature distribution to develop inside the droplet. We consider the cooling of a superheated liquid sphere from an initially uniform temperature θ_0 until its surface reaches some prescribed nucleation temperature θ_N. Assuming that only conductive heat transfer takes place in the metal and that the surface conductance is constant in space and time, we obtain a concentric-isotherm temperature distribution given by [88]

$$(\theta + Ste)/(\theta_0 + Ste) = 2Bi \sum_p L_p [\sin(\lambda_p \phi)/\phi] \exp(-\lambda_p^2 Fo) \qquad (6.1)$$

$$L_p = \sin(\lambda_p)/[\lambda_p^2 - (1-Bi)\sin^2(\lambda_p)] \qquad (6.2)$$

where $\phi = (r/r_0)$ is the dimensionless radial position and λ_p are the eigenvalues defined by

$$\lambda_p \cos(\lambda_p) - (1-Bi)\sin(\lambda_p) = 0 \qquad (6.3)$$

The analytical solution given above can now be used to evaluate the characteristic parameters of this period.

It has been shown elsewhere that the achievable supercooling in a liquid is determined by the activity of the heterogeneous nucleants [47-55] and the cooling rate [46,74]. The expression for the instantaneous average cooling rate obtained from Equation (6.1) was found to be identical to that obtained from the Newtonian model when the surface temperature T_s is substituted for T in Equation (5.5)

$$\varepsilon_L = 3 \ (\alpha_L/k_L) \ (h/r_0) \ (T_S - T_G) \tag{6.4}$$

Examples of calculated cooling rates for 50 μm droplets of Al, Fe and Ni, assuming a high heat transfer coefficient of 5×10^4 W m^{-2} K^{-1} are given in Table 6.

Table 6

Average Cooling Rates in 50 μm Liquid Metal Droplets (MK s^{-1})[†]

	Al	Fe	Ni
Biot Number, hr_0/k_L	0.014	0.031	0.032
Initial cooling rate ($\theta_s = \theta_0 = 0.2$Ste)	1.7	1.9	1.7
at the melting point ($\theta_s = \theta_M = 0$)	1.4	1.6	1.4
at the onset of hypercooling ($\bar{\psi}_N = 0$)	0.6	1.2	1.0

† h = 5×10^4 Wm^{-2}K^{-1}

Cooling times can also be estimated from Equation (6.1) setting $\theta = \theta_N$, $\phi = 1$, and looking for the corresponding Fo value via Newton-Raphson or any other root searching technique. Figure 11 shows the dependence of the cooling time for a droplet nucleating at its melting point, t_M, on the Biot number and initial superheat. The time calculated from the analytical solution has been normalized for purposes of representation, dividing it by the Newtonian cooling time obtained from Equation (5.7). The values in the ordinate of Figure 11 indicate the divergence between the two models and may be interpreted as correction factors to the Newtonian equation.

Table 7

Cooling Times for Atomized Metal Droplets (μs)[†]

θ_0/Ste	$2r_0$ (μm)	Al	Fe	Ni
0.3	50	41 (42)	84 (90)	87 (93)
	500	304 (417)	445 (900)	453 (935)
0.3	50	114 (115)	243 (248)	252 (257)
	500	1053 (1148)	2002 (2476)	2063 (2572)

† $h = 5 \times 10^4 \ Wm^{-2}K^{-1}$
Values in parenthesis are from the Newtonian model.

Examples of cooling times calculated from Figure 11 for droplets of Al, Fe and Ni are given in Table 7. As expected, at
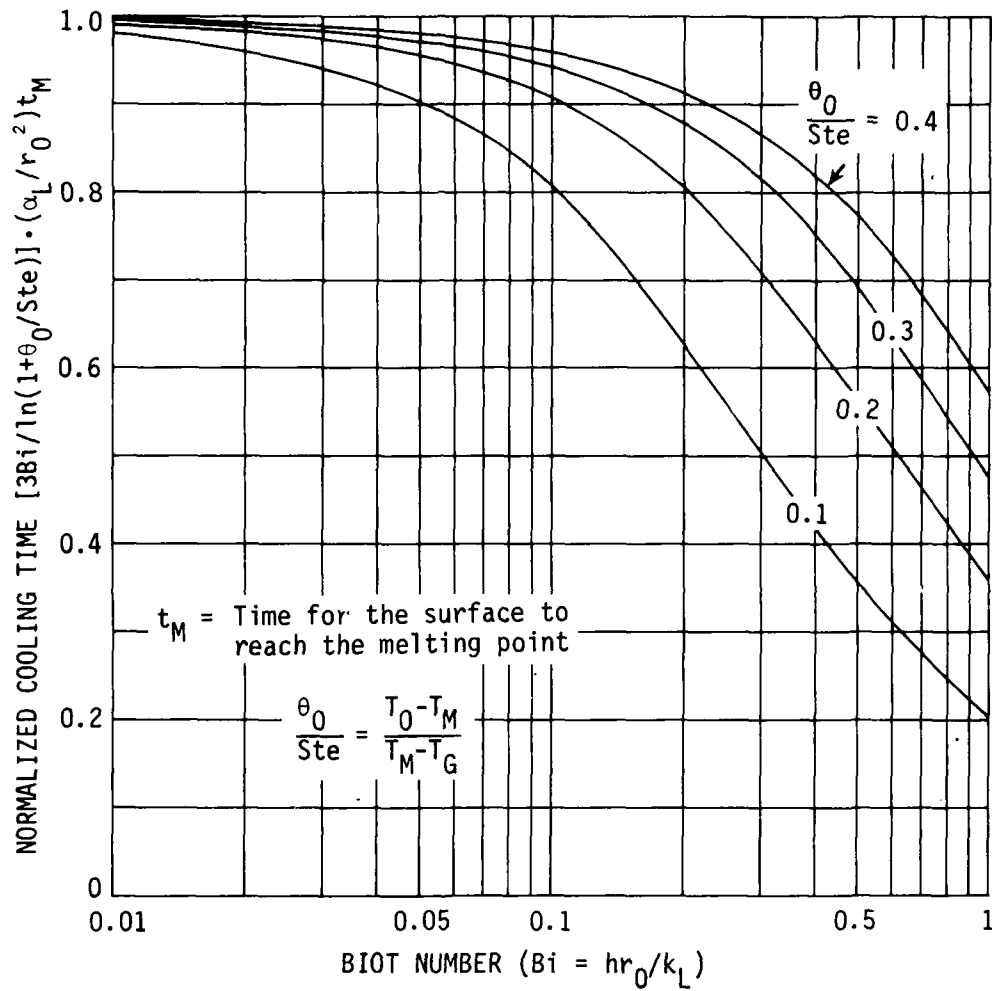
Figure 11. Normalized time for the surface of a liquid droplet to cool from an initial temperature T_0 to its melting temperature T_M by convection to an environment with constant temperature T_G, as a function of Biot number and initial superheat.

equivalent initial superheats the time for non-Newtonian cooling is shorter because not all the sensible heat in the droplet is removed before its surface reaches the nucleation temperature. Note also that reducing the droplet diameter will result in a smaller reduction in t_M than that predicted by the Newtonian model. On the other hand, increasing the heat transfer coefficient will have a larger effect in reducing the cooling time than the inverse proportionality expected from Equation (5.7).

Normalized temperature distributions in liquid droplets when their surfaces reach the melting point, for different Biot numbers and initial temperatures are shown in Figure 12. The largest gradient occurs at the surface and is given by the boundary condition

$$(\partial T/\partial r)_s = (h/k_L) \ (T_s - T_G) \tag{6.5}$$

Appropriate substitution of the variables in this equation reveal that significant gradients may exist within the droplet even for Biot numbers of 0.01 or lower. For example, a heat transfer coefficient of 5×10^4 W m^{-2} K^{-1} (Bi=0.014 for $2r_0 = 50$ μm) produces a maximum gradient of 3.5×10^5 K m^{-1} in Al droplets when $T_s = T_M$.

Although the surface gradient is independent of superheat and particle size, as concluded from Equation (6.5), these variables have an important effect on the internal temperature

$\dfrac{T_0-T_M}{T_M-T_G}$	BIOT NUMBER Bi = hr_0/k_L			
	1.0	0.5	0.1	0.01
0.1	A	B	F	I
0.2	B	D	G	J
0.3	C	E	H	K
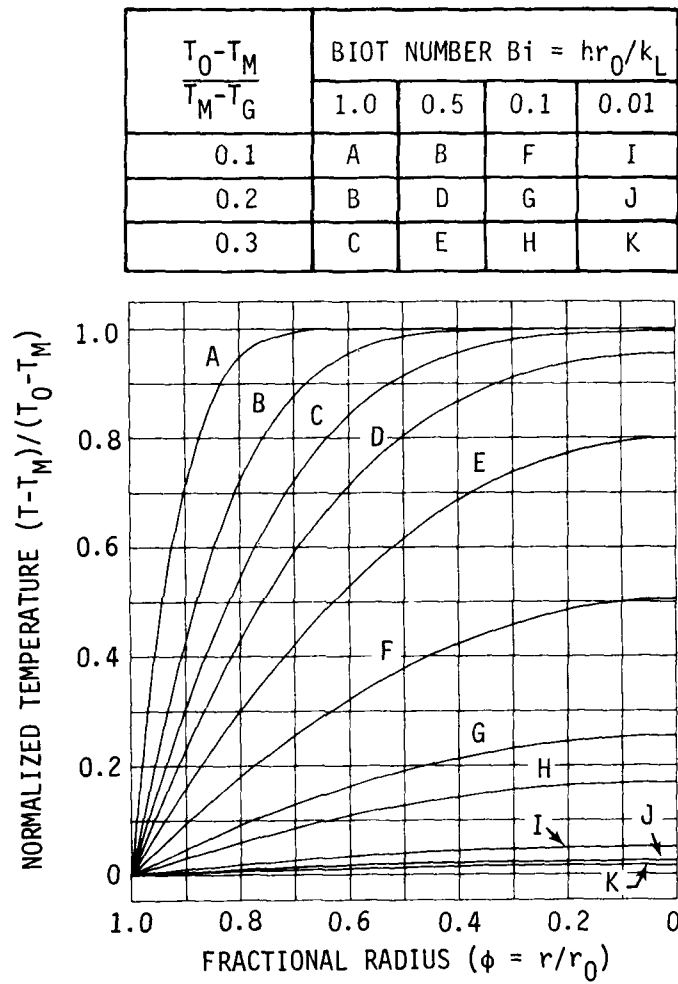
Figure 12. Normalized temperature distributions in a liquid droplet when its surface reaches the melting temperature T_M, for different Biot numbers and initial superheats.

profiles. For example, maximum temperature differences $\Delta(T)$ of 4.4 and 45 K between the center and the surface were estimated from Equation (6.1) for 50 and 500 μm Aluminum droplets respectively, using the h and T_s values given above and an initial superheat of 190 K. Thus, the basic assumption that temperature differences inside the body are negligible (and hence that the Newtonian model is a valid approximation) for Bi < 0.1 may not always be justified. The original superheat was found to influence only slightly the temperature distributions for Bi < 0.01.

During metal atomization one wishes to suppress nucleation until a certain level of enthalpy is reached in the liquid, since this enthalpy is essentially a measure of the volume fraction that can be solidified before the droplet recalesces to the "slow growth" regime, as indicated in Chapter 5. Because the surface is always cooler than the rest of the droplet, the volume averaged enthalpy of the latter, $\bar{\psi}$, is always larger than that corresponding to the surface temperature. $\bar{\psi}$ is related to the average temperature $\bar{\theta}$ through Equation (3.10) for g = 0, ($\bar{\psi} = 1+\bar{\theta}$), and can be calculated from the following expression

$$(\bar{\psi}-1+\text{Ste})/(\theta_0+\text{Ste}) = 6\text{Bi}^2 \sum_p L_p' \exp(-\lambda_p^2 \text{Fo}) \tag{6.6}$$

$$L_p' = [\sin(\lambda_p)/\lambda_p^2] \, L_p \tag{6.7}$$

We now define $\bar{\psi}_N$ as the average enthalpy of the droplet at the

moment of nucleation; $\bar{\psi}_N$ represents the minimum amount of heat
that must be withdrawn by the cooling environment during
solidification. Heat extraction after nucleation will then be
necessary in all cases where $\bar{\psi}_N > 0$.

Table 8

Undercooling Required at the Surface for the
Droplet to Reach the Hypercooled Regime, (K)[†]

Diameter (μm)	Al	Fe	Ni
500	372	415	474
50	365	353	418
Newtonian	364	345	411

† $h = 5 \times 10^4 \ Wm^{-2}K^{-1}$, $\theta_0 = 0.2Ste$

Combining Equations (6.1) and (6.6) yields a relationship
between the desired $\bar{\psi}_N$ value and the required θ_N at the surface,
($\phi = 1$), which represents the maximum allowable nucleation
temperature. This relationship is plotted in Figure 13 as a
function of the Biot number for two levels of enthalpy. $\bar{\psi}_N = 1$
is the point where all the superheat has been removed from the
droplet, and $\bar{\psi}_N = 0$ is the enthalpy where the droplet reaches the
hypercooled regime. Values of the undercooling required at the
surface when $\bar{\psi}_N = 0$ for droplets of Al, Fe and Ni are reported in
Table 8. Note that as r_0 increases, nucleation must be suppressed
to lower temperatures in order to reach the hypercooled regime,
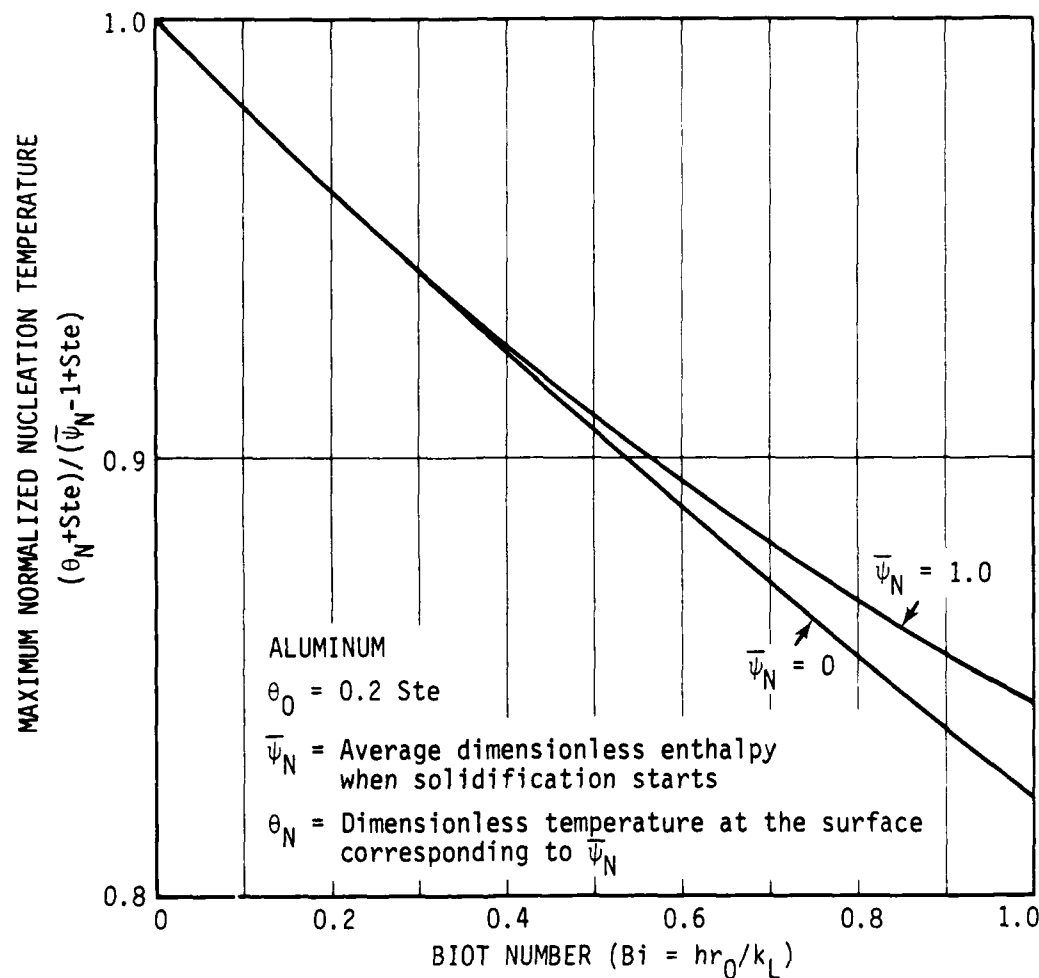
Figure 13. Effect of the Biot number on the temperature to which
nucleation must be suppressed at the surface in order
to reach an average dimensionless enthalpy of $\overline{\psi}_N$ in
the droplet.

but the cooling rates (and the likeliness to achieve larger undercoolings prior to solidification) decrease in an inverse proportion, as indicated by Equation (6.4). One can then conclude that the achievement of large undercoolings is not only hindered kinetically but also thermally when the particle size increases. The effects are more noticeable in Fe and Ni due to their lower thermal conductivity.

The time required to reach an enthalpy $\bar{\psi}_N$ can be calculated from Equation (6.6) using the Newton-Raphson formulation as before. Results for Al are reported in Figure 14, where the values have been normalized by their Newtonian equivalent, (see Equation (5.7) for $\theta_N = \bar{\psi}_N - 1$). The times calculated from the series solution are now higher than the corresponding Newtonian values since the ratio of the cooling rates at the same average enthalpy is given by

$$\epsilon(\text{Newtonian})/\epsilon(\text{non-Newtonian}) = (\theta + \text{Ste})/(\theta_s + \text{Ste}) \qquad (6.8)$$

and this ratio is always larger than one for $\theta = \theta_s$. For example, the non-Newtonian and Newtonian times to reach the hypercooled regime in a 50 μm droplet of Al with $h = 5 \times 10^4$ W m^{-2} K^{-1} and an initial superheat of 190 K are 490 and 455 μs respectively.
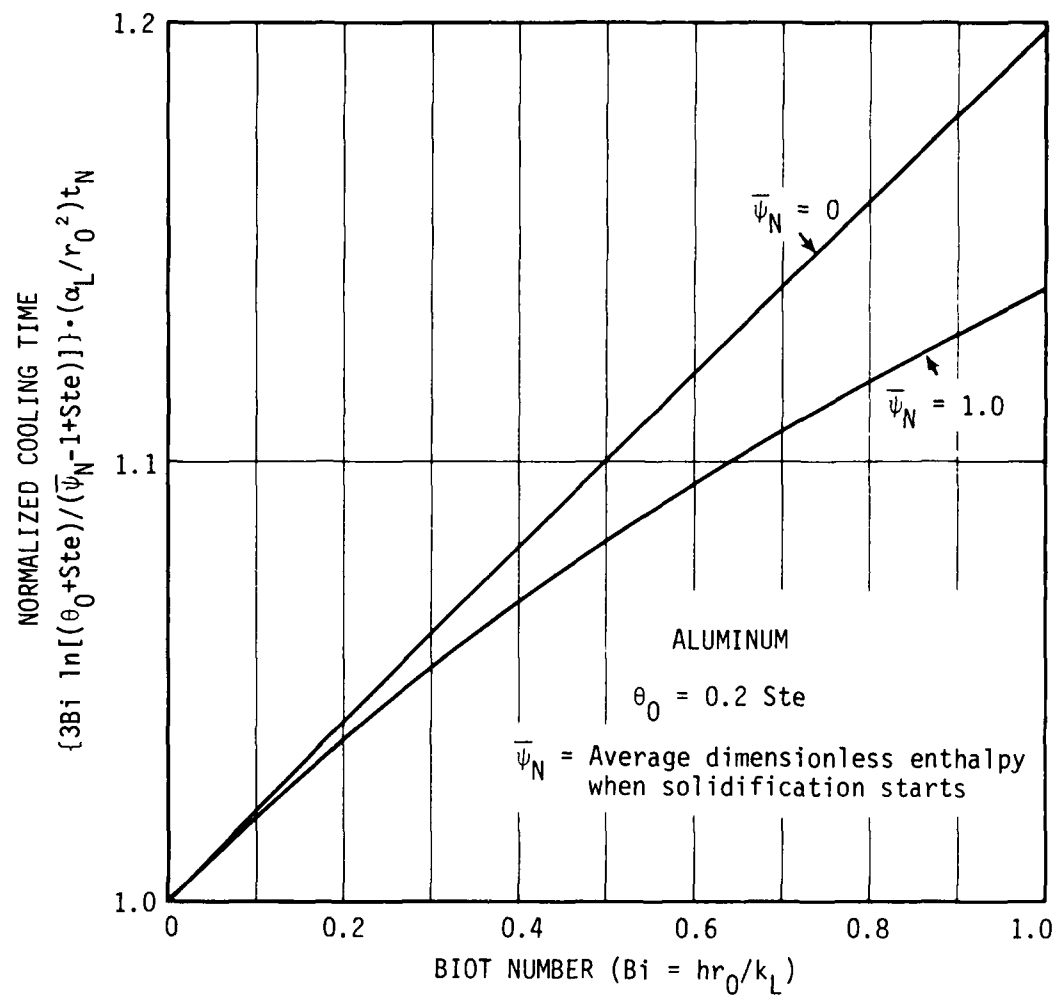
Figure 14. Normalized cooling time, for the droplet to reach an average enthalpy content of $\overline{\psi}_N$, as a function of Biot number.

CHAPTER 7

SOLIDIFICATION WITHOUT UNDERCOOLING: ENTHALPY MODEL

We now address the solidification problem where no
significant undercooling is required for either nucleation or
growth. This situation resembles the case where active catalysts
limit the achievable undercooling to a few degrees. As in the
previous chapter, we assume that only conductive heat flow takes
place inside the droplet and that the heat transfer coefficient
is constant in time and space, resulting in a concentric isotherm
geometry. Since all the points on the surface have the same
enthalpy (or temperature), solidification must start
simultaneously as a thin shell, and the interface follows at any
time the spherical shape of the isotherms. We further assume
that the interface configuration is stable through the entire
solidification process (no breakdown to cells or dendrites).

7.1 Mathematical Formulation

For this part of the problem the spherical droplet is
divided into a fixed number of concentric shell domains of
thickness Δr for the internal nodes ($1 < i < n$) and $\Delta r/2$ for the
center ($i = 1$) and the surface ($i = n$) nodes, as shown in
Figure 15. An enthalpy balance for an element of volume V_i and
surface area A_i can be written as

DROPLET
SURFACE

INTERFACE   SOLID
$\psi_\ell = 1-g_\ell$ $\psi_i < 0$

LIQUID
$\psi_i > 1.0$

r_o

$r*$

1   2   i-1   i   i+1 ℓ-1 ℓ ℓ+1   n

$\phi_1^- = 0$

ϕ_i

$\phi*$

$\Delta\phi$

$\phi_i^- = \phi_i - \dfrac{\Delta\phi}{2}$

$\phi_i^+ = \phi_i + \dfrac{\Delta\phi}{2}$

$\phi_n^+ = 1$
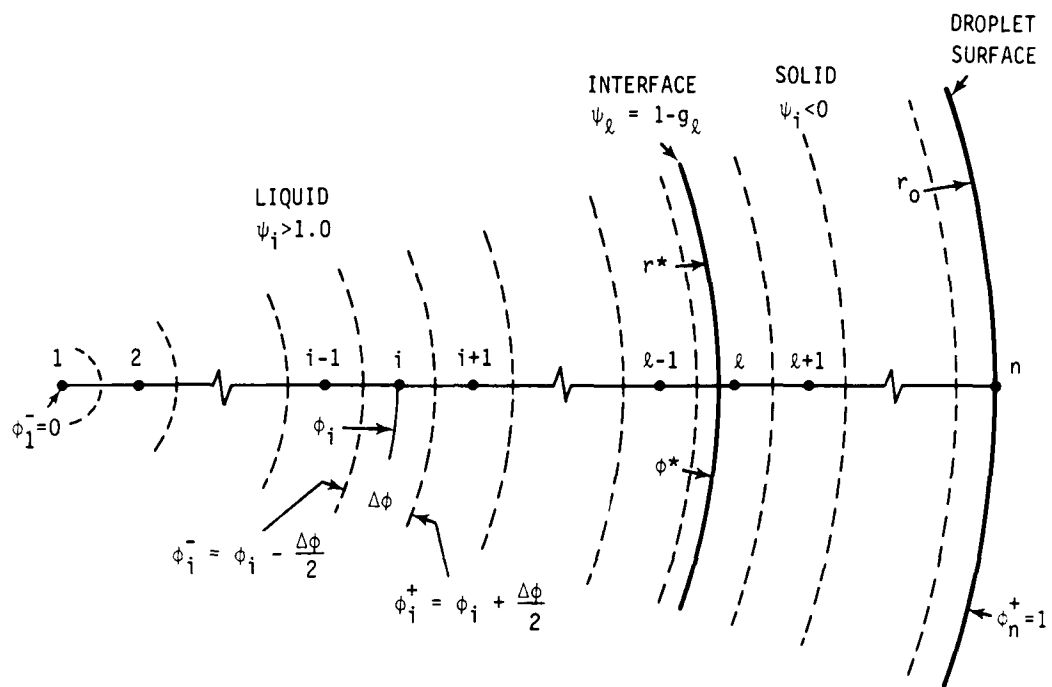
$$A_i^- = (\phi_i^-)^2 \qquad\qquad k^+ = k^- = k_L \quad \text{if } i < \ell$$

$$A_i^+ = (\phi_i^+)^2 \qquad\qquad k^+ = k^- = k_S \quad \text{if } i > \ell$$

$$V_i = (\phi_i^+)^3 - (\phi_i^-)^3 \qquad k^+ = k_S, \; k^- = k_L \quad \text{if } i = \ell$$

Figure 15. Mesh defined for the Enthalpy model of solidification
without undercooling. The interface position is
determined from the overall fraction solid.

$$(d/dt) \int_{V_i} \rho \, H \, dV = \int_{A_i} (k \, \nabla T) \cdot (\tilde{e} \, dA) \qquad (7.1)$$

where $\tilde{e}$ is the unit vector normal to the bounding surface of the element. The resulting expression for an internal node is

$$(dH_i/dt) = k^+(A_i^+/V_i)(\partial T/\partial r)_i^+ - k^-(A_i^-/V_i)(\partial T/\partial r)_i^- \qquad (7.2)$$

where A_i^-, A_i^+ and V_i denote the inner and outer surface areas and the volume of the spherical shell i respectively. The superscripts (+) or (−) refer to the positive and negative r directions.

In general, H_i in Equation (7.2) refers to the specific enthalpy of the volume element i and assumes different forms when the node is in the liquid, the solid, or contains the liquid-solid interface. k is the thermal conductivity of the liquid or the solid; $k^+ = k^-$ for all nodes except that containing the interface, $i = \ell$, where $k^+ = k_S$ and $k^- = k_L$ (see Figure 15).

Equation (7.2) can now be put in terms of the dimensionless nodal enthalpy ψ_i, temperature θ_i, distance ϕ and time Fo, and becomes

$$(d\psi_i/dFo) = (r_0^3/V_i)(Q_i^- - Q_i^+) \qquad (7.3)$$

where

$$Q_i^+ = -(k^+/k_L)(A_i^+/r_0^2)(\partial\theta/\partial\phi)_i^+ \qquad i \neq n \qquad (7.4)$$

$$Q_i^- = - (k^-/k_L)(A_i^-/r_0^2) \; (\partial\theta/\partial\phi)_i^- \qquad\qquad i \neq 1 \qquad (7.5)$$

For the center node, $i = 1$, the term Q^- on the right hand side of Equation (7.3) becomes zero. For the surface node, $i = n$, an energy balance similar to expression (7.2) is written, modifying the (+) term to account for the heat loss to the environment. Appropriate manipulation of this equation using the definitions of dimensionless nodal enthalpy and temperature yields the following expression for Q_n^+

$$Q_n^+ = (A_n^+/r_0^2) \; Bi \; (\theta_n + Ste) \qquad\qquad (7.6)$$

As concluded from the discussion of the enthalpy-temperature diagram, Figure 2, the dimensionless nodal enthalpy is always negative in the solid region ($g_i = 1$, $\theta_i < 0$), whereas in the superheated liquid region ψ_i is larger than unity, ($g_i = 0$, $\theta_i > 0$). A volume element containing the liquid solid interface ($i = \ell$) is at the melting point of the metal; therefore, the value of ψ_ℓ is equal to the volume fraction of the element which is in the liquid state, $1-g_\ell$.

Equations (7.3) to (7.6) were put into their equivalent fully-implicit finite difference forms. The resulting system of simultaneous equations for the different nodes was solved using the Gauss-Seidel iterative technique starting with the temperature distribution obtained from the analytical solution

for the pre-solidification stage, Equation (6.1), when the surface reaches the melting temperature ($\theta_N = 0$). The convergence criterion used for each iteration cycle was

$$\sum_{i=1}^{i=n+1} |(\psi_{i,k+1}^{t}/\psi_{i,k+1}^{c}) - 1| \leq 10^{-4} \tag{7.7}$$

where the superscripts t and c denote the trial and calculated values respectively.

The dimensionless time interval, ΔFo, was adjusted in every step k to give roughly uniform displacements of the liquid-solid interface. Trial runs were performed changing the number of nodes N, and the length of the interface displacements $\Delta\phi^*$, (i.e. the length of the time steps). It was observed that for the metals investigated, increasing the number of nodes above 21 does not significantly affect the results. On the other hand, some parameters like G_L/R, cooling rates in the liquid and interface velocities at the beginning ($\phi^* \to 1$) and at the end ($\phi^* \to 0$) of solidification are particularly sensitive to the time step size, especially in the low range of Biot numbers. For these calculations the time step sizes were appropriately selected until convergence was reached. Calculations were performed on a CDC CYBER 175 computer.

7.2 Results and Discussion

The computer heat flow model was used to calculate the important cooling and solidification parameters (e.g. cooling rates, interface velocities, temperature gradients, etc.) as a function of time and the dimensionless variables--mainly Biot number--governing the rate of heat extraction from the droplets.

Curves relating the net solidification time for droplets of Al, Fe and Ni to the Biot number and dimensionless initial superheat are presented in Figure 16. The time resulting from the numerical solution of the Enthalpy model has been normalized dividing it by the time calculated for solidification in a Newtonian regime, given by Equation (5.10).

Table 9

Net Solidification Times for Atomized
Metal Droplets: no Undercooling, (µs)[+]

$2r_0$ (µm)	θ_0/Ste	Al	Fe	Ni
50	0.3	263	274	317
	0	257	265	305
	Newtonian	252	216	283
500	0.3	3172	5405	4898
	0	3047	4795	4267
	Newtonian	2518	2160	2826

+ $h = 5 \times 10^4 \text{ Wm}^{-2}\text{K}^{-1}$

Examples of calculated solidification times for droplets of the three metals investigated are shown in Table 9 and compared
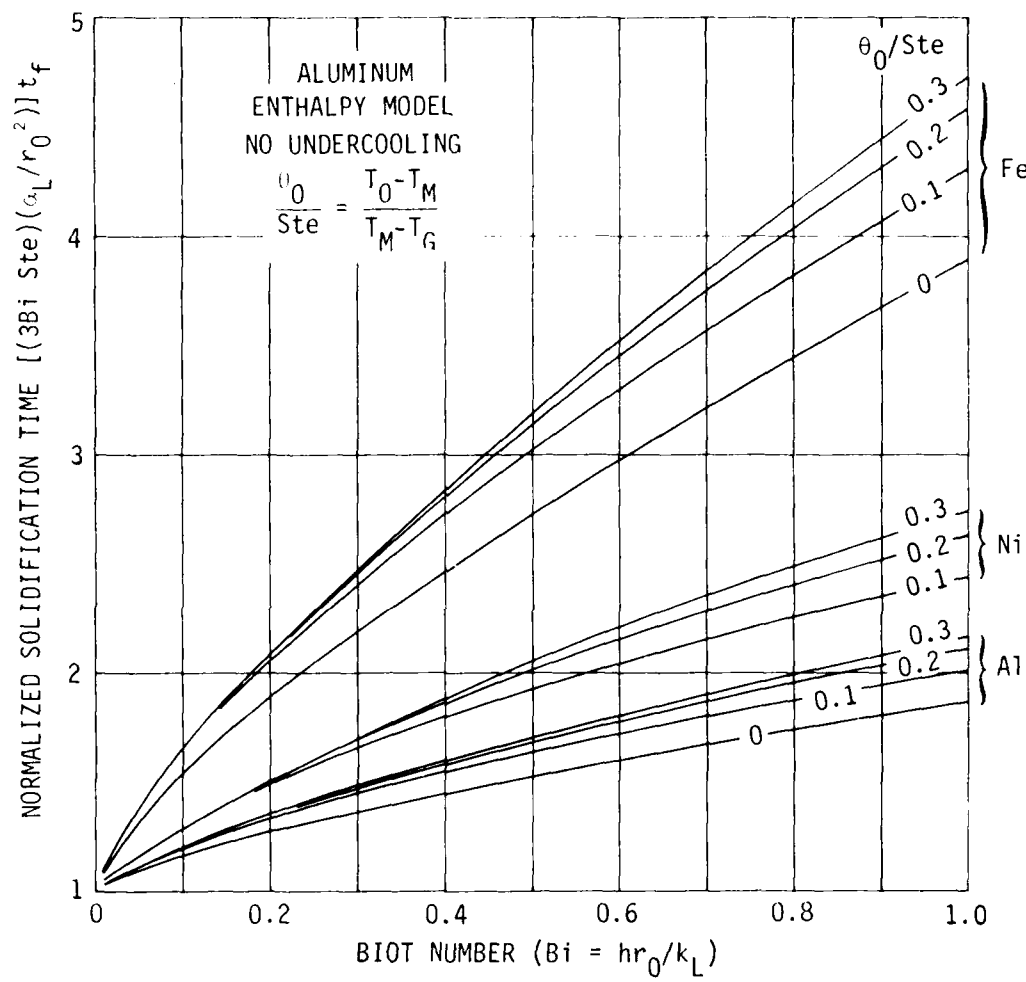
Figure 16. Normalized solidification time for liquid droplets of aluminum, iron and nickel, as a function of Biot number and dimensionless initial superheat θ_0. The calculated curve for nickel with no superheat closely follows that of aluminum for $\theta_0 = 0.3$Ste.

to the corresponding Newtonian predictions. As anticipated, increasing initial superheat prolongs solidification; the sensible heat retained in the liquid portion of the droplet increases resulting in longer times from initiation to completion of solidification. Note also that the effect of superheat on the solidification time diminishes with decreasing Biot number, in agreement with our previous observation that θ_0 has a negligible influence on the temperature distributions at the start of solidification for Bi < 0.01.

Figure 17 shows the effect of Biot number and initial superheat on the liquid-solid interface velocity in Al droplets as solidification progresses (i.e. ϕ^* decreases). As in previous figures, the values reported are the ratios of non-Newtonian to Newtonian velocities calculated *for the concentric geometry,* Equation (5.13). Note that in all cases the Newtonian results represent an upper boundary to the achievable growth velocites predicted by the Enthalpy model.

Some of the trends observed in this figure can be better understood from the boundary condition

$$R = (Q^+ - Q^-)/\Delta H_M = (k_S G_S - k_L G_L)/\Delta H_M \qquad (7.8)$$

which relates the interface velocity R to the heat fluxes on the liquid (Q^-) and solid (Q^+) sides respectively. In the absence of initial superheat ($\theta_0 = 0$), both models dictate the same velocity at the start of solidification ($\phi^* = 1$) regardless of Biot
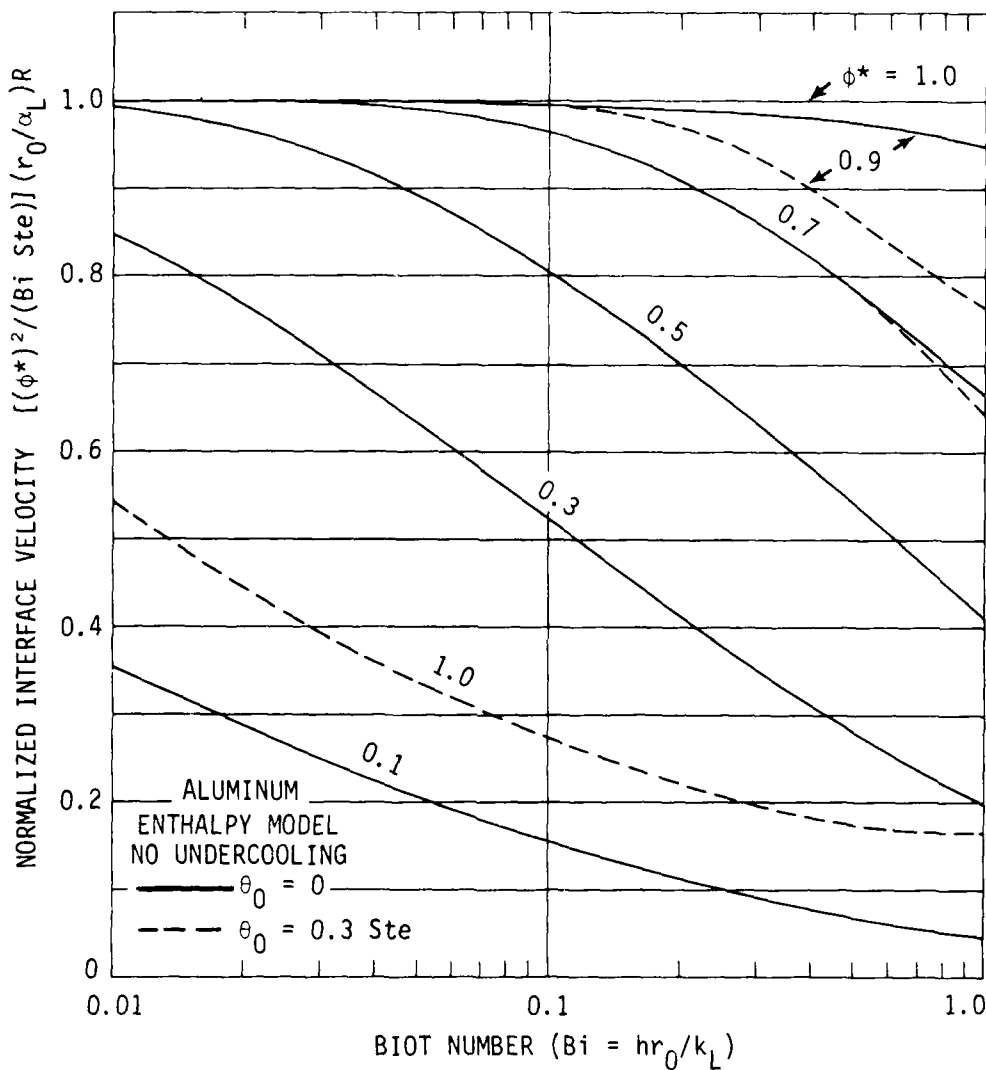
Figure 17. Normalized interface velocity as a function of Biot number and initial superheat. Note that the Newtonian model gives always the limit to the achievable velocity as calculated from the enthalpy model.

number. This results arises when no gradient G_L exists prior to solidification (hence $Q^- = 0$ in the above equation), and the Q^+ term is given by the surface heat flow

$$Q^+ = h \ (T_M - T_G) \tag{7.9}$$

which is identical for the Newtonian and numerical solutions. For a finite superheat ($\theta_0 > 0$) there is a positive temperature gradient G_L in front of the interface which slows down growth by opposing the G_S term in Equation (7.8). For example, an initial superheat of 190 K ($\theta_0 = 0.3$Ste) may cut the initial velocity to less than half the value calculated for $\theta_0 = 0$ (see Figure 17). It is also clear that this effect decays rapidly as fraction *solid increases, due to the elimination of the liquid residual* superheat in the early stages of solidification.

Examples of interface velocities calculated with the Enthalpy model for Al, Fe and Ni droplets, and their corresponding Newtonian values are given in Table 10. As anticipated, the two solutions diverge with increasing Biot number and the progress of solidification. Furthermore, the Enthalpy model predicts a reduction in velocity as the particle size increases, whereas the Newtonian model indicated no such effect. On the other hand, increasing the heat transfer coefficient at constant r_0 will increase R at any location.

Table 10

Interface Velocities for Concentric Solidification
Enthalpy Model: No Undercooling, (cm s^{-1})†

ϕ^*:(g)	$2r_0$ (μm)	Al	Fe	Ni
0.9	500	4.0	3.7	3.0
(0.271)	50	4.1	4.7	3.6
	Newtonian	4.1	4.8	3.6
0.5	500	10.0	5.3	6.5
(0.875)	50	13.0	11.3	10.5
	Newtonian	13.2	15.4	11.8
0.1	500	44.5	12.8	21.0
(0.999)	50	107.0	46.6	61.1
	Newtonian	330.9	385.8	295.1

† $h = 5 \times 10^4$ Wm^{-2}K^{-1}, $\theta_0 = 0.3$Ste.

The results of normalized ratio of temperature gradient in
the liquid side of the interface, G_L, to interface velocity R for
the three metals investigated, are presented in Figure 18. G_L at
the beginning of solidification is approximately given by the
boundary condition at the surface

$$\lim_{\phi^* \to 1} G_L = (h/k_L)\ (T_M - T_G) \tag{7.10}$$

while the initial interface velocity is close to that calculated
from Equation (5.13), hence, the initial G_L/R ratio should
asymptotically approach a constant value with decreasing Biot
number
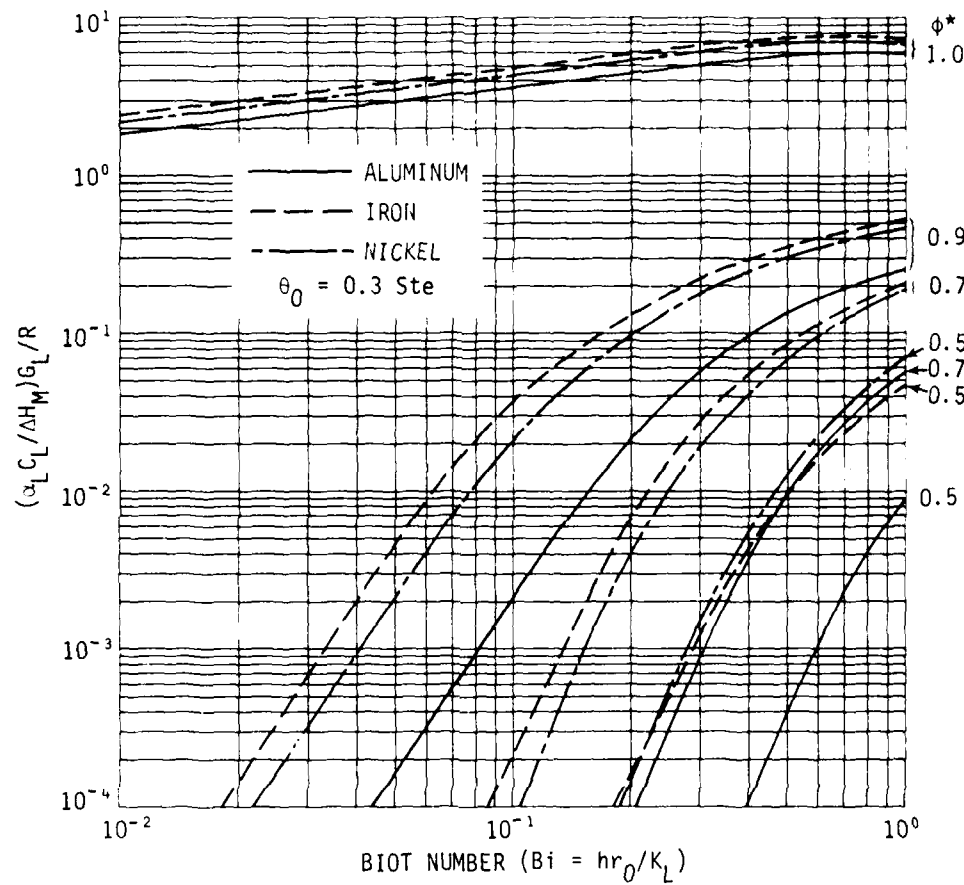
Figure 18. Normalized ratio of the temperature gradient in the
liquid at the liquid-solid interface, G_L, to the
interface velocity R, during solidification of Al, Fe
and Ni droplets.

$$\lim_{Bi \to 0} (G_L/R)_{\phi^*=1} = \Delta H_M/(\alpha_L \, C_L) \tag{7.11}$$

For example, G_L/R ratios of 2×10^7 and 4.3×10^7 K s m^{-2} were calculated for 50 and 500 μm Al droplets respectively, at the start of solidification. The limiting value given by Equation (7.11) is 1.1×10^7 K s m^{-2}. As noted in Figure 18, G_L/R decreases markedly with increasing fraction solid, especially at low Bi, since the liquid superheat is rapidly dissipated ($G_L \to 0$) and the interface velocity increases.

Normalized values of the calculated average cooling rates in the solid and liquid during solidification of Aluminum droplets are shown in Figure 19 and Figure 20 respectively. Note that the part of the normalizing factor inside the brackets is the Newtonian solidification time obtained from Equation (5.9), which is directly proportional to r_0 and inversely proportional to h. Therefore, increasing the Biot number by increasing the droplet size r_0, will increase the actual cooling rate only if the slope of the curve at that point is larger than unity. On the other hand, increasing the heat transfer coefficient h will always increase the cooling rate. Finally, decreasing the initial superheat will increase the achievable cooling rates in the solid, but the effect is only felt at the initial stages of solidification. The average cooling rate in the liquid , $\bar{\varepsilon}_L$, decreases with the progress of solidification, the effect being more pronounced at small Biot numbers (Figure 20).
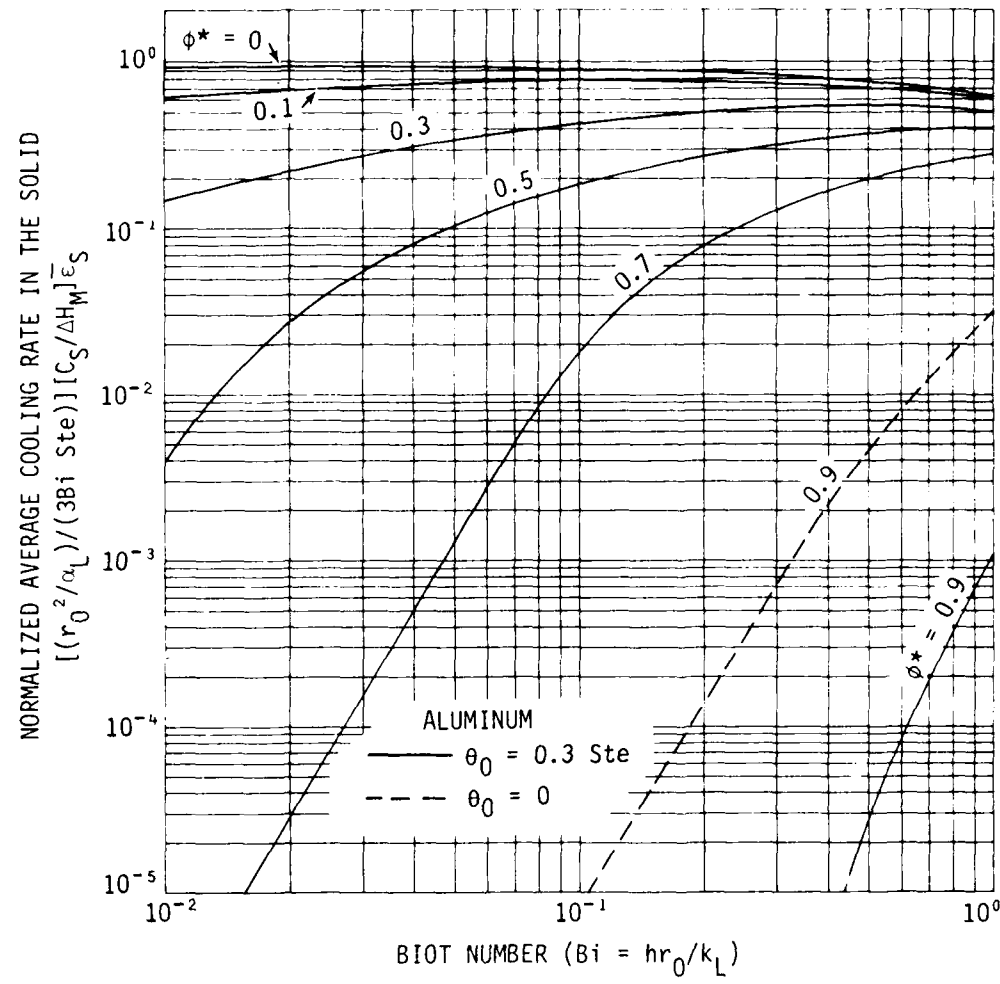
Figure 19. Normalized instantaneous average cooling rate in the solid during solidification of aluminum droplets, as a function of Biot number and fractional position of the liquid-solid interface ϕ^*. θ_0 and Ste denote the dimensionless initial temperature and Stefan number, respectively.
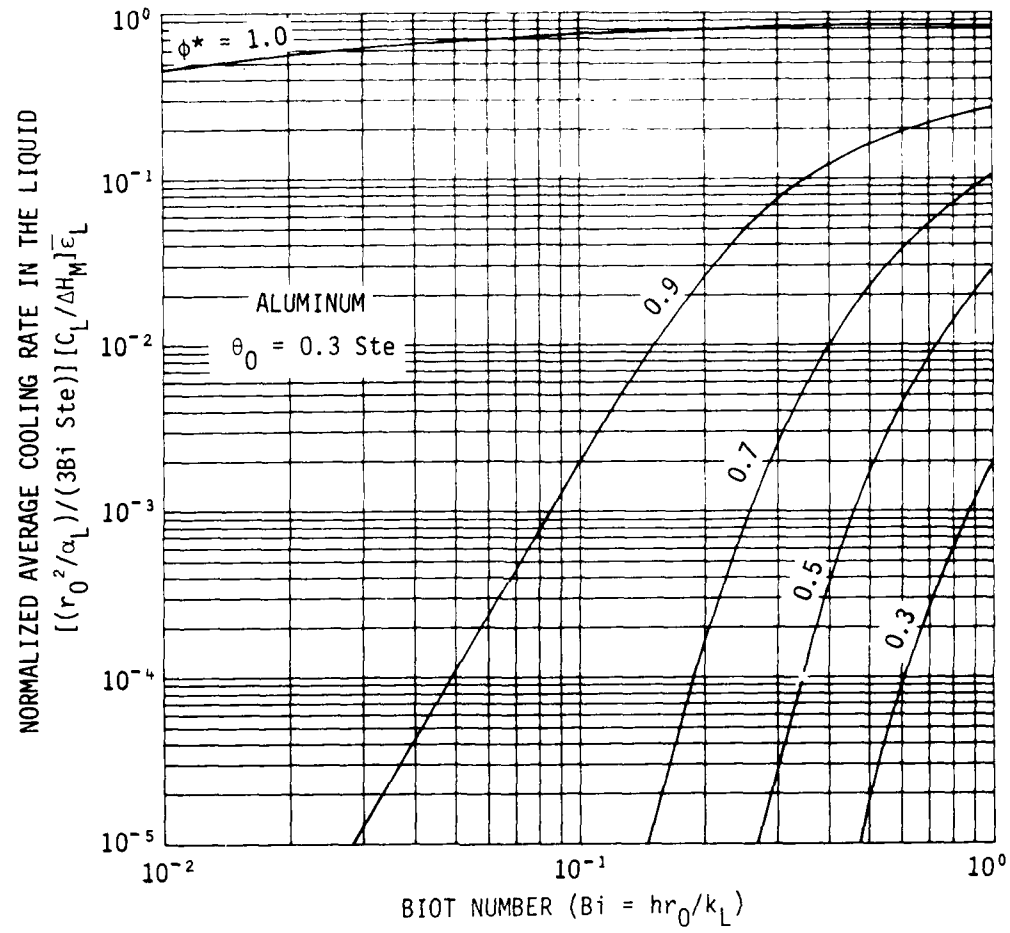
Figure 20. Normalized instantaneous average cooling rate in the liquid during solidification of aluminum droplets, as a function of Biot number and fractional position of the liquid-solid interface ϕ^*. θ_0 and Ste denote the dimensionless initial temperature and Stefan number, respectively.

Table 11

Average Cooling Rates During Solidification of Aluminum Droplets (K s^{-1})[†]

	ϕ*	Diameter (μm) 50	500
$\bar{\epsilon}_L$	1.0	7.3×10^5	1.1×10^5
	0.9	2.2	1.2×10^3
	0.7	–	1.2
$\bar{\epsilon}_S$	0.7	22.0	5.3×10^3
	0.3	2.4×10^5	6.1×10^4
	0	1.3×10^6	1.2×10^5

[†] $h = 5 \times 10^4$ Wm^{-2}K^{-1}, $\theta_0 = 0.3$Ste

Examples of cooling rates during solidification of Al droplets without undercooling are given in Table 11. It is important to mention that the relatively low values obtained from this model are due in part to the prescription of a discrete melting temperature. When a liquid-solid temperature range exists, as in the case of an alloy, and no substantial undercooling is considered, the solidification times will be similar to those of the pure metal (provided the heat of fusion is reasonably constant). Since solidification of an alloy is not isothermal, the cooling rates should therefore be higher throughout the process.

CHAPTER 8

SOLIDIFICATION WITH UNDERCOOLING: ENTHALPY MODEL

This final chapter of the non-Newtonian heat flow analysis deals with the modelling of the solidification process in an undercooled droplet from a single nucleation event occuring at its surface. The assumptions of constant heat transfer coefficient, cooling environment temperature and pure conduction inside the droplet are held through this model, but since the solid grows from one point on the surface, the isotherms are no longer concentric and the problem becomes two-dimensional. Furthermore, the thermal field is symmetrical around the growth axis, i.e. the line that joins the nucleation point on the surface with its antipode.

Since temperature gradients may now exist inside the droplet, the liquid-solid interface is likely to develop different thermal conditions at different locations. Therefore, the undercoolings and velocities vary along the interface and its shape departs from the spherical configuration prescribed in the Newtonian analysis for axisymmetric solidification, Figure 3.

8.1 Mathematical Formulation

We divide the spherical droplet into volume elements defined on a superimposed bispherical (bipolar rotational) coordinate

system (u,v,w) [89]. By making the rotational axis coincident with the growth axis and following a pattern similar to the Wulff net we obtain the mesh shown in Figure 21. The coordinate surface $u = \pi/2$ represents the droplet surface, $u = \pi$ is the growth axis, $v = -\infty$ is the nucleation point and $(\pi,0)$ is the droplet center. A typical node i,j ($1 \leq i \leq n$, $1 \leq j \leq m$) with coordinates

$$u_i = (\pi/2)[1+(i-1)/(n-1)] \tag{8.1}$$

$$v_j = 0.5 \ln\{\cot^2[(1-(2j-1)/2m)(\pi/2)]\} \tag{8.2}$$

is depicted in Figure 21. The volume element about this node is bound by the coordinate surfaces

$$u_i^E = u_{i+1}^W = (\pi/2)[1+(2i-1)/2(n-1)] \qquad i \neq n \tag{8.3}$$

$$u_n^E = \pi \tag{8.4}$$

$$u_1^W = \pi/2 \tag{8.5}$$

$$v_j^N = v_{j+1}^S = 0.5 \ln\{\cot^2[(1-j/m)(\pi/2)] \qquad j \neq m \tag{8.6}$$

$$v_m^N = \infty \tag{8.7}$$

$$v_1^S = -\infty \tag{8.8}$$
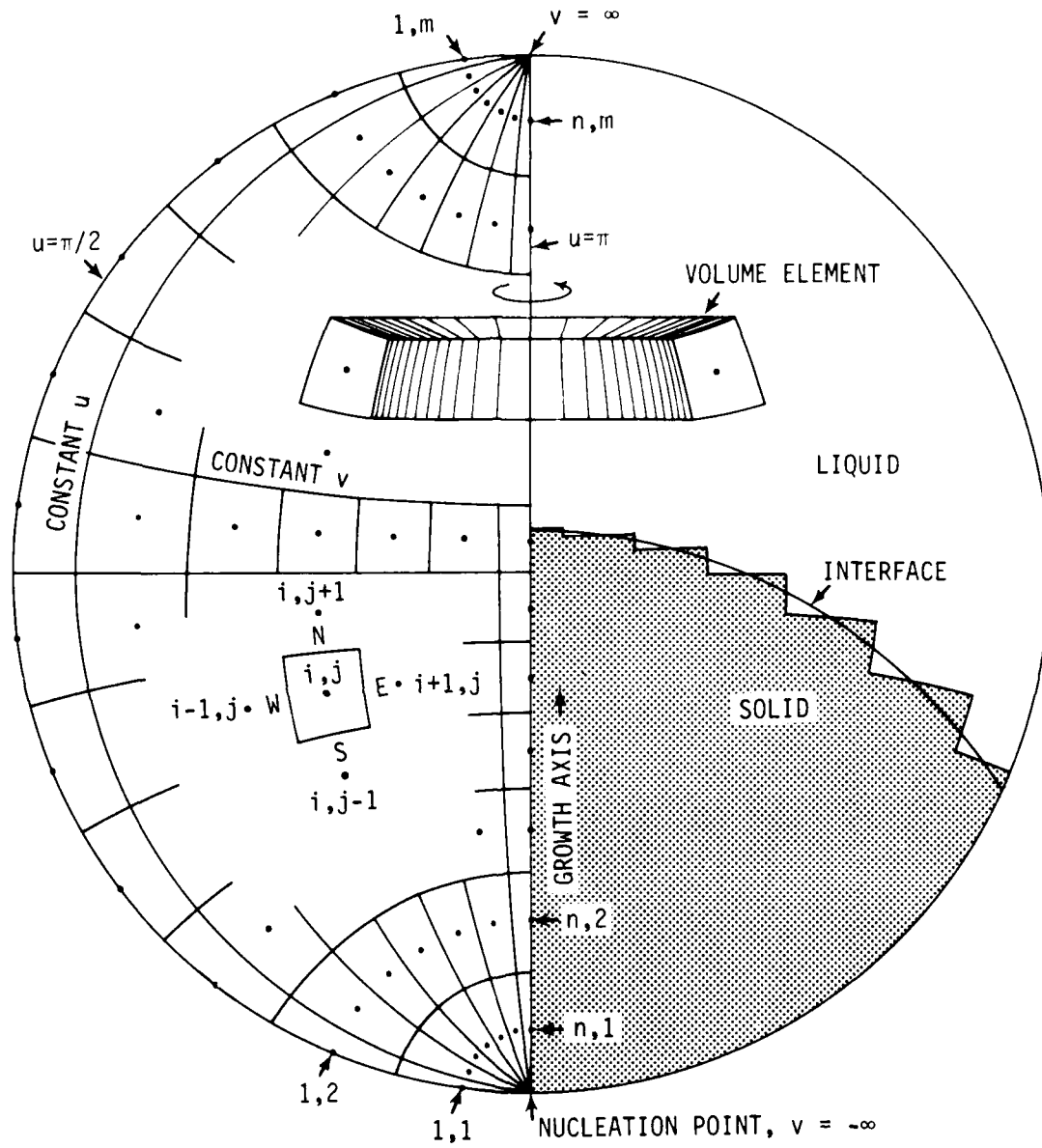
Figure 21. Mesh defined in bispherical coordinates for the
Enthalpy model of undercooled solidification. The
mesh has rotational symmetry about the growth axis,
and the interface is approximated by a series of
annular steps following a constant v surface for each
u_i.

where the superscripts N and S indicate the positive and negative
v directions respectively (v and j increase from S to N), E and W
indicate the positive and negative u directions respectively (u
and i increase from W to E).

The volume for the element with limits $u_i^W \leq u \leq u_i^E$,
$v_j^S \leq v \leq v_j^N$, may be calculated from the following expression

$$V_{i,j} = r_0^3 (V_{i,j}^W - V_{i,j}^E) \tag{8.9}$$

where

$$V_{i,j}^W = \csc(u_i^W) \{B_{i,j}^{W,N} - B_{i,j}^{W,S}$$
$$+ \cot(u_i^W)[\text{asin}(B_{i,j}^{W,N}\sin(u_i^W)) - \text{asin}(B_{i,j}^{W,S}\sin(u_i^W))]\} \tag{8.10}$$

$$V_{i,j}^E = V_{i+1,j}^W \qquad\qquad i \neq n \tag{8.11}$$

$$V_{n,j}^E = [\tanh(v_j^N/2) - \tanh(v_j^S/2)]/2$$
$$- [\tanh^3(v_j^N/2) - \tanh^3(v_j^S/2)]/6 \tag{8.12}$$

The coefficients B in Equation (8.10) are defined by

$$B_{i,j} = \sinh(v_j)/[\cosh(v_j) - \cos(u_i)] \tag{8.13}$$

and are evaluated by replacing the values of u_i and v_j
corresponding to the superscripts N, S, E or W for each case.
Note that for $v_1^S = -\infty$

$$B_{i,1}^{W,S} = B_{i,1}^{E,S} = \tanh(v_1^S/2) = -1 \qquad (8.14)$$

also, for $v_m^N = \infty$

$$B_{i,m}^{W,N} = B_{i,m}^{E,N} = \tanh(v_m^N/2) = 1 \qquad (8.15)$$

We now recall the general expression for the nodal enthalpy balance, Equation (7.1), and replace the gradient

$$\nabla T = (\tilde{e}_1/\sqrt[2]{m_{11}})\ (\partial T/\partial u) + (\tilde{e}_2/\sqrt[2]{m_{22}})\ (\partial T/\partial v) \qquad (8.16)$$

and the differentials of the heat transfer areas, namely

$$dA = \sqrt[2]{m_{22}\ m_{33}} \qquad (8.17)$$

for the E and W surfaces, and

$$dA = \sqrt[2]{m_{11}\ m_{33}} \qquad (8.18)$$

for the N and S surfaces. m_{11} and m_{22} are the metric coefficients defined by

$$m_{11} = m_{22} = r_0^2/[\cosh(v)-\cos(u)]^2 \qquad (8.19)$$

$$m_{33} = [r_0\sin(u)]^2/[\cosh(v)-\cos(u)]^2 \qquad (8.20)$$

and $\tilde{e}$ is given by $-\tilde{e}_1$, $\tilde{e}_1$, $-\tilde{e}_2$ and $\tilde{e}_2$ for the W, E, S and N surfaces respectively. Appropriate rearrangement and integration of Equation (7.1) yields the dimensionless form of the nodal enthalpy balance in bispherical coordinates

$$(d\psi_{i,j}/dFo) = (2\pi r_0^3/V_{i,j})\ (Q_{i,j}^N + Q_{i,j}^N + Q_{i,j}^E + Q_{i,j}^W) \qquad (8.21)$$

where

$$Q_{i,j}^N = -Q_{i,j+1}^S = (k^N/k_L)\ (\partial\theta/\partial v)^N$$
$$\ln\{[\cosh(v_j^N)-\cos(u_i^E)]/[\cosh(v_j^N)-\cos(u_i^W)]\}\ \ j \neq m \qquad (8.22)$$

$$Q_{i,m}^N = 0 \qquad (8.23)$$

$$Q_{i,1}^S = 0 \qquad (8.24)$$

$$Q_{i,j}^E = -Q_{i+1,j}^W = (k^E/k_L)\ (\partial\theta/\partial u)^E$$
$$[a\sin(B_{i,j}^{E,N}\sin(u_i^E))-a\sin(B_{i,j}^{E,S}\sin(u_i^E))] \qquad i \neq n \qquad (8.25)$$

$$Q_{n,j}^E = 0 \qquad (8.26)$$

$$Q_{1,j}^W = -Bi(\theta_{i,j}+Ste)[\tanh(v_j^N)-\tanh(v_j^S)] \qquad (8.27)$$

ψ, θ, Bi, Ste and Fo are defined as before. k in Equations (8.22) to (8.27) is assigned the value of k_S or k_L if the volume element is solid or liquid and is surrounded by nodes

of the same phase. If either the volume element or the nearest
neighbor involved in the particular Q term under evaluation is
undergoing solidification, or if they are not of the same phase,
k is asigned a weighted average between k_S and k_L.

Writing Equation (8.21) in its implicit finite-difference
form we obtain an expression of the type

$$\psi_{i,j,k+1} + C_{i,j,k+1}\,\theta_{i,j,k+1} = RHS \qquad (8.28)$$

The right hand side RHS of this equation is a function of the
nodal enthalpy in the previous time step $\psi_{i,j,k}$, the temperatures
of the surrounding nodes and the conductivity ratios k/k_L in the
current time step. The coefficient of $\theta_{i,j,k+1}$ in the left hand
side is also unknown for the time Fo_{k+1} since it contains a
series of (k/k_L) factors. Substituting the definition of
enthalpy, Equation (3.10), into (8.28) we obtain the expression
for the nodal temperature

$$\theta_{i,j,k+1} = (RHS-1+g_{i,j,k+1})/(C_{i,j,k+1}+1+\triangle Cg_{i,j,k+1}) \qquad (8.29)$$

For a mesh with N = n x m nodes there are N equations like this,
each one with two unknowns (θ and g). Since g is known for the
nodes that are completely liquid (g = 0) or solid (g = 1) at time
Fo_{k+1}, we only need to define a set of relationships between g
and θ for those nodes undergoing solidification at a particular
time. As in Chapter 5, it is necessary to prescribe a certain

interfacial geometry for each node in order to translate the
linear displacements dictated by the kinetic model into changes
in nodal fraction solid.

We now assume that the interface is divided into a series of
n annular steps, each one propagating along a line of nodes of
constant u_i, as indicated in Figure 21. The interface takes the
shape of a constant v coordinate surface for each level i, which
is identified by v_i^*. The dimensionless interface velocity is then

$$\underline{R}_i = [\cosh(v_i^*) - \cos(u_i)]^{-1} \, (\partial v_i^*/\partial Fo) \tag{8.30}$$

and for a time interval ΔFo the initial and final positions of
the interface are related through the following equations

$$v_{i,k+1}^* = \ln[-b+(b^2 + c)^{1/2}] \qquad\qquad i \neq n \tag{8.31}$$

$$b = B_{i,k+1}^* \cos(u_i)/(1-B_{i,k+1}^*) \tag{8.32}$$

$$c = (1+B_{i,k+1}^*)/(1-B_{i,k+1}^*) \tag{8.33}$$

$$B_{i,k+1}^* = \csc(u_i)\sin\{\underline{R}\Delta Fo\sin(u_i)+a\sin[B_{i,k}^*\sin(u_i)]\} \tag{8.34}$$

$$B_i^* = \sinh(v_i^*)/[\cosh(v_i^*)-\cos(u_i)] \tag{8.35}$$

For the nodes located about the growth axis, i = n

$$v^*_{n,k+1} = \ln[(1+B^*_{n,k+1})/(1-B^*_{n,k+1})] \tag{8.36}$$

$$B^*_{n,k+1} = \underline{R}\Delta Fo + B^*_{n,k} \tag{8.37}$$

$$B^*_n = \tanh(v^*_n/2) \tag{8.38}$$

Note that for the initial step $B^*_{i,j} = -1$ for all nodes.

The nodal fraction solidified can now be easily calculated from Equation (8.9) to (8.13) by substituting v^*_i for v^N_j and dividing the resulting solid volume by the total nodal volume $V_{i,j}$.

Since the interface velocity $\underline{R}_i$ and its undercooling θ^*_i are related by a kinetic law of the type discussed in Chapter 2, the last step in the analysis is to establish the relationship between θ^*_i and the temperature of the solidifying node $\theta_{i,\ell(i)}$. If one simply assigns to θ^*_i the value of $\theta_{i,\ell(i)}$, problems arise because of the steep negative temperature gradient developed in front of the growing solid. When the interface moves from a node $i,\ell(i)$ to $i,\ell(i)+1$, Figure 22, it encounters a much cooler environment (hence a larger driving force) because the temperature $\theta_{i,\ell(i)+1}$ is usually much lower than $\theta_{i,\ell(i)}$, especially in the early stages of recalescence. This condition would translate into rather large peaks in the velocity distribution every time an interfacial step crosses a node boundary.
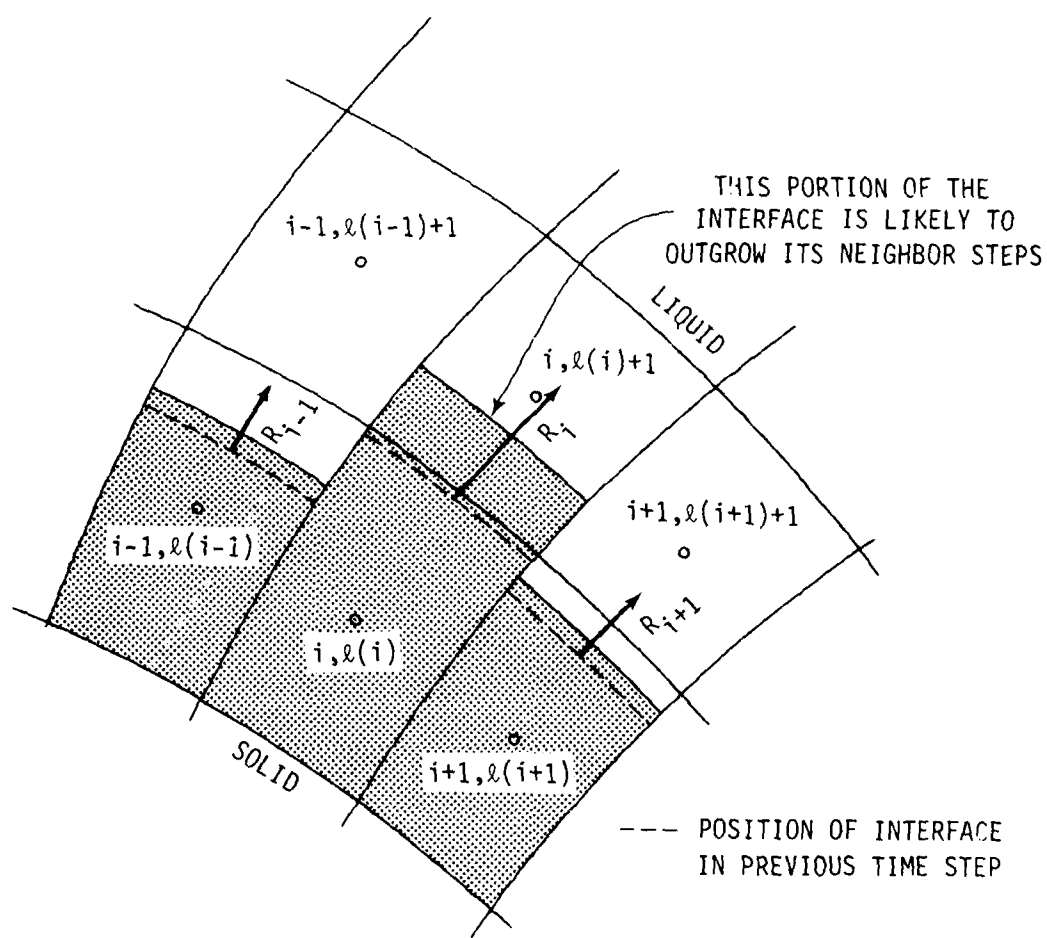
Figure 22. Schematic of the stability problem originated when the
interface temperature is assigned the value
corresponding to the volume element in which it is.

A further complication arises because the interface is not coincident with the same v coordinate surface for all nodes, see Figure 22. If such were the case, most of the latent heat released by the node $i, \ell(i)$ would be dumped into the liquid node in front of it, $i, \ell(i)+1$. However, if the interface in node $i, \ell(i)$ crosses the v_j^N boundary before its neighbors $i-1, \ell(i-1)$ or $i+1, \ell(i+1)$, it finds itself into a node $i, \ell(i)+1$ that has two extra heat sinks, namely $i-1, \ell(i-1)+1$ and $i+1, \ell(i+1)+1$. Since the driving force is increased and the heat can be dissipated more easily for the step i, the interface is likely to develop a "perturbation" that grows faster into the undercooled liquid and slows the growth of the neighbor steps.

The stability problem described above is mathematical in nature, caused by the introduction of a localized interface into the Enthalpy model. The behavior of the resulting "breakdown" may be compared to the thermal instability predicted for interfaces moving into undercooled liquids ($G_L < 0$), as discussed in Chapter 2.

It was found after different trials that the best way to maintain the interface stable was to restrict the temperature gradient on the solid side, G_S, to positive values (or zero), effectively making

$$\theta_i^* = \theta_{i, \ell(i)-1} \quad \text{if} \quad \theta_{i, \ell(i)} < \theta_{i, \ell(i)-1} \tag{8.39}$$

$$\theta_i^* = \theta_{i, \ell(i)} \quad \text{if} \quad \theta_{i, \ell(i)} \geq \theta_{i, \ell(i)-1} \tag{8.40}$$

This assumption is consistent with the physical situation. A negative G_S is not likely to occur in a recalescing droplet since it requires that the liquid enhances its capacity as a heat sink during solidification, whereas in reality it is exhausted. The above restriction on θ_i^* manifests as an averaging of the growth velocities throughout the node, although it has the side effect of slightly slowing the kinetics of the process. To partially avoid this problem, Equation (8.39) was only applied in the first half of the node, that is, before the interface crosses the nodal coordinate v_ℓ. Note also that the above restriction does not affect directly the temperatures of the solid nodes behind the interface.

Equation (8.29) can now be solved with the aid of Equations (8.30) to (8.40). Trial runs were performed for 84 (12 x 7), 180 (18 x 10) and 210 (20 x 11) nodes in the mesh. The convergence criterion used for each iteration cycle was

$$\sum_{1,1}^{n,m} |\theta_{i,j}^t/\theta_{i,j}^c - 1| + \sum_{i}^{n} |g_{i,\ell(i)}^t/g_{i,\ell(i)}^c - 1| \leq 10^{-3} \quad (8.41)$$

It was found that the results did not differ significantly among the three cases but the computation time was approximately quadrupled for a twofold increase in the number of nodes. The computation time was also increased by going to a lower undercooling, a smaller particle size, heat transfer or kinetic coefficients. It was concluded that for the range of values of

interest a mesh with 84 nodes produced satisfactory results in a reasonable time. As in the previous cases, calculations were performed on a CDC Cyber 175 computer.

8.2 Results and Discussion

The computer model was used to study the solidification of undercooled liquid aluminum droplets, focusing on the departure from the Newtonian trends established in Chapter 5 and the interfacial behavior during solidification. A series of calculations with both linear and exponential kinetics, Equations (2.4) and (2.5) respectively, were carried out for different undercoolings. Since temperature gradients were allowed inside the droplet, the enthalpy temperature curve was evaluated in terms of the weighted averages of these properties over the entire particle.

As expected from the Newtonian analysis, the thermal history was found to be strongly dependent on the initial undercooling, but instead of being unique for a constant K/Bi ratio, it was affected by the particular values of the dimensionless kinetic coefficient and the Biot number. The variables involved in these dimensionless paramenters, namely r_0, K_M and h, were therefore considered individually in terms of their effect on the solidification behavior.

8.2.1 Effects of the particle size

Although the K/Bi ratio is independent of the droplet dimensions, increasing r_0 will progressively shift the $\bar{\psi}-\bar{\theta}$ curve away from the Newtonian case, as shown in Figure 23. The Enthalpy model consistently predicts larger average undercoolings than the corresponding Newtonian (same K/Bi) at equivalent fractions solidified. This is due to the "local" recalescence of the interface which reduces the growth rate at a given g and consequently enhances the role of the heat flow during the "rapid solidification" stage. As the particle radius increases, the external heat extraction is less able to influence the withdrawal of latent heat released at the moving solid-liquid front. The interface then reduces its undercooling at an earlier stage, and the amount of rapidly solidified material, as determined from the growth rate, is diminished. However, the "recalesced" zone is actually a smaller fraction of the overall volume, and therefore the average droplet undercooling is likely to be higher. It is then concluded that the $\bar{\psi}-\bar{\theta}$ path will be truly indicative of the extent of rapid solidification only when the droplet satisfies the Newtonian condition of negligible temperature differences during recalescence.

Figure 23 also shows that as r_0 decreases the curves approach a limit slightly different from the Newtonian case, probably due to the differences in geometry and the "reduced" kinetics discussed in the previous section. For example,
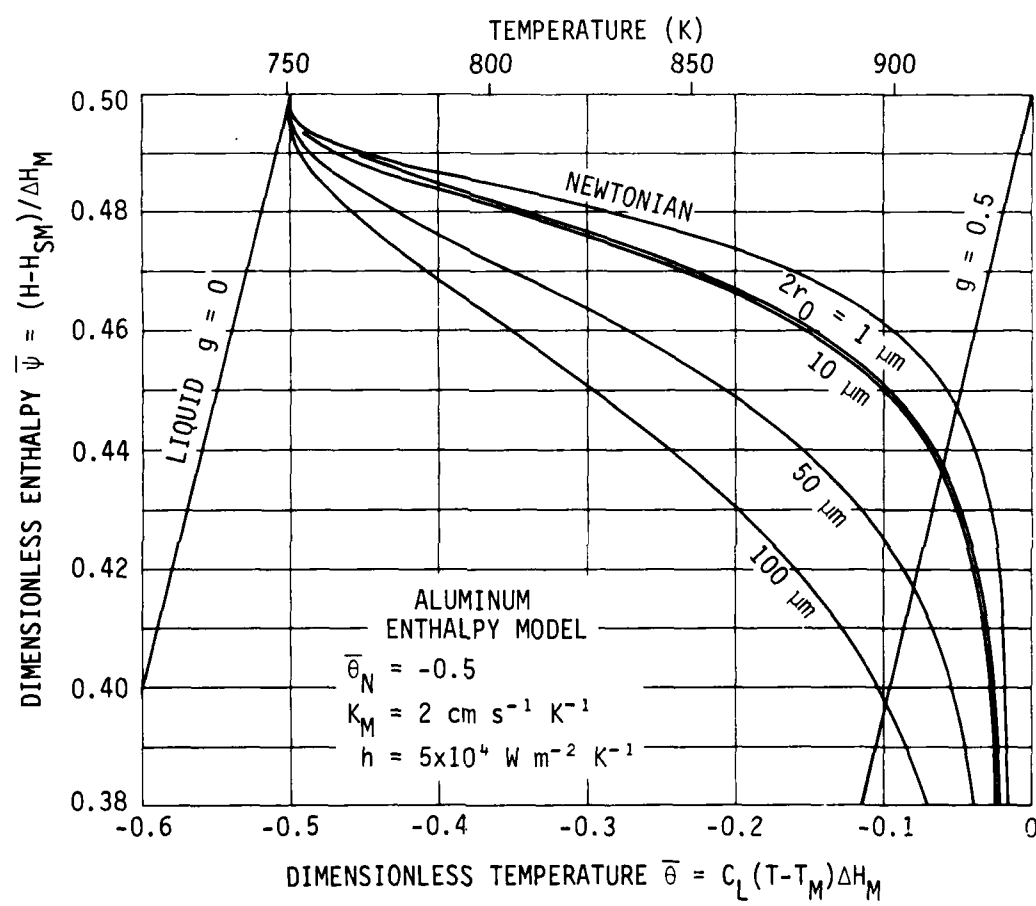
Figure 23. Departure from the Newtonian thermal history as
particle size increases. Note that the enthalpy and
temperature are now averaged over the entire droplet.

characteristic undercoolings $\Delta T(g^a)$ of 35.7, 22.2 and 21.8 K were calculated from this figure for 100, 10 and 1 μm Al droplets respectively, whereas the corresponding Newtonian value is 18 K.

Figure 24 shows the temperature profiles along the growth axis (i = n), as a function of fraction sol . for a fixed diameter of 10 μm. The corresponding drop. temperatures and interface positions calculated from the Newtonian model are given for comparison. Note that the internal temperature differences $\Delta(T)$ go through a maximum during recalescence. For example, maximum $\Delta(T)$ values of 7, 52 and 148 K occuring at fractions solid of 0.08, 0.108 and 0.126 were calculated for Al droplets of 1, 10 and 100 μm in diameter, respectively, under the conditions of this figure.

Figure 25 shows the effect of particle size on the temperature profiles for a constant fraction solid g = 0.1. It is evident from this figure that decreasing the particle size drastically reduces $\Delta(T)$, the profile being almost flat for droplets of about 1 μm in diameter or less. Further analysis of Figure 25 reveals that as the droplet size increases, the liquid away from the nucleation point becomes less sensitive to the recalescing interface, and may even cool slightly below the original θ_N. Since the time scale of the solidification process is roughly proportional to r_0, it can be concluded that the larger particles can maintain liquid regions undercooled for longer times, and therefore are more likely to develop multiple nucleation events and polycrystalline structures.
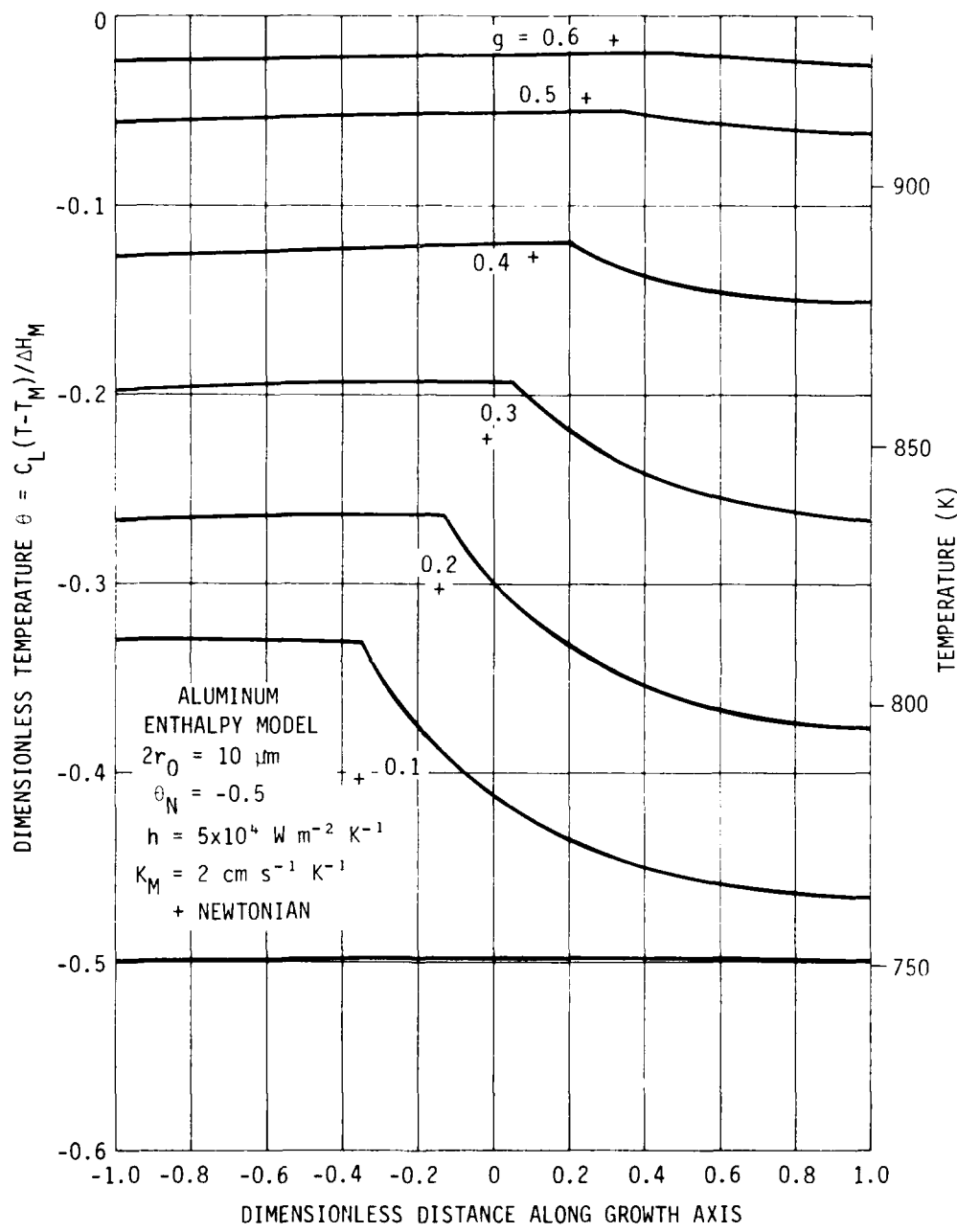
Figure 24. Thermal profiles developed inside the droplet as solidification progresses, for a constant particle diameter of 10 μm.
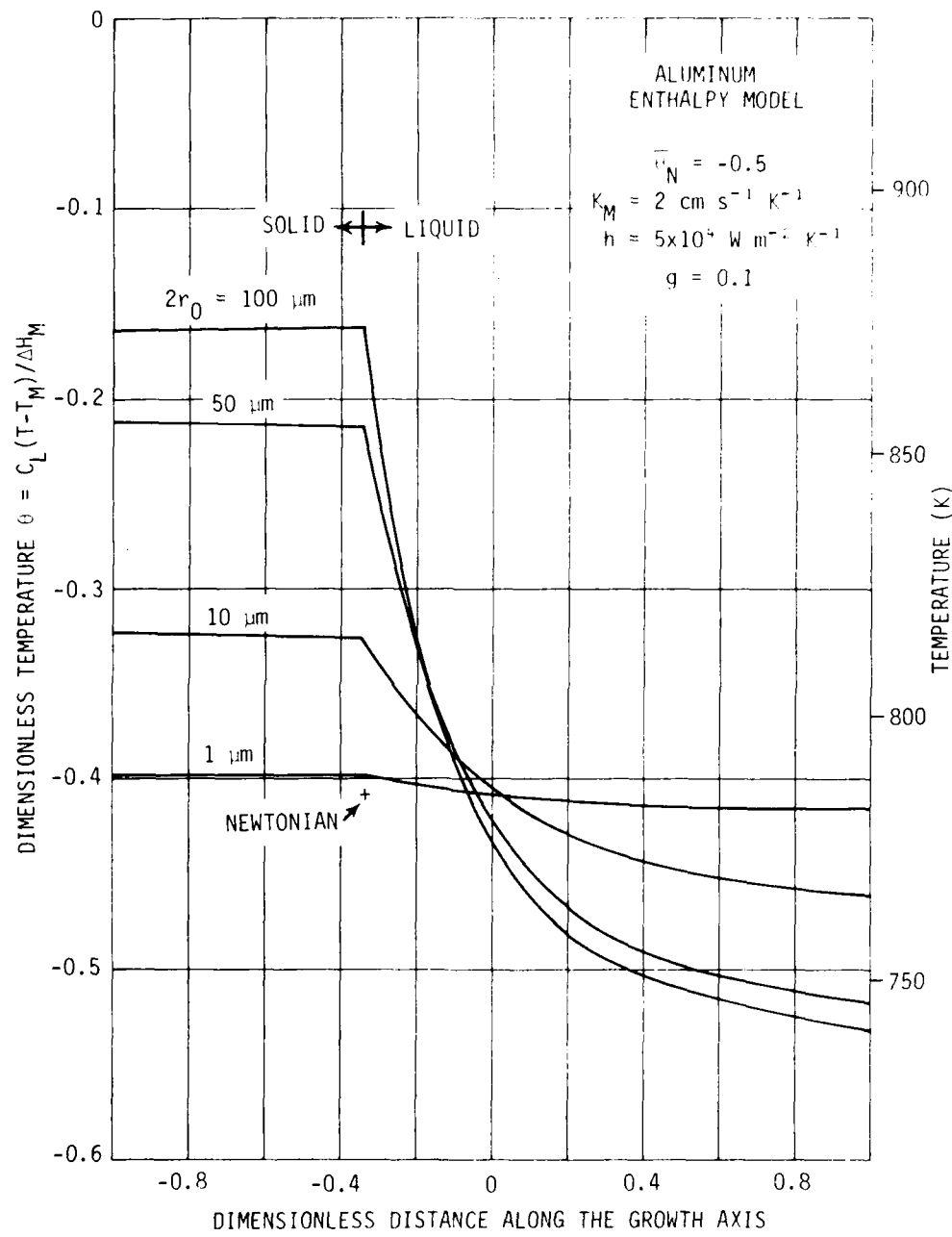
Figure 25. Thermal profiles developed inside the droplet as a function of particle size for a constant fraction solid g=0.1.

Although the temperature differences are reduced inside the droplet as the radius decreases, the average temperature gradient at the interface,

$$G_{SL} = 2\ (k_S G_S + k_L G_L)/(k_S + k_L) \tag{2.7}$$

for a given fraction solid does not change significantly in actual magnitude, as shown in Table 12. As a matter of fact, the temperature gradients at the interface should increase in the smaller particles in order to sustain the larger velocities expected in them, at least in the early stages of recalescence.

Table 12

Average Gradients at the Interface During
Solidification of Undercooled Aluminum Droplets (K μm^{-1})[†]

Fraction solid, g	Diameter (μm)		
	1	10	100
0.1	-15.3	-12.4	-4.7
0.2	-11.6	-11.0	-4.5
0.3	- 6.7	- 6.7	-4.3
0.4	- 2.5	- 3.6	-4.0
0.5	- 0.7	- 1.2	-1.9

[†] $\Delta T_N = 182$ K, $h = 5 \times 10^4$ Wm^{-2}K^{-1}, $K_M = 2$ cms^{-1}K^{-1}

The average gradient G_{SL} is always negative during recalescence because it is dominated by the largely negative G_L term in Equation (2.7). It then follows from the discussion on morphological stability in section 2.2.2 that the thermal

field promotes interface breakdown during solidification of undercooled droplets. As the liquid undercooling is exhausted G_L and G_{SL} increase towards zero, as indicated in Table 12, and the latter may even become slightly positive near the end of solidification, therby reducing its destabilizing influence on the interface. A note of caution is necessary with regard to the gradient values calculated *from this program*, since we have introduced a localized interface in a volume element which is assumed to have uniform properties. Therefore, the values will only be conceptually correct when the interface position coincides with the node ($v_i^* = v_{\ell(i)}$) and its temperature is equal to that of the node. It should be noted, however, that the variations in the gradients as the interface moves inside a node are within an order of magnitude.

Figure 26 shows the effect of particle size on interfacial temperatures (hence velocities) at the growth axis, as a function of fraction solidified. As the radius increases, the interface recalesces at an earlier stage; its undercooling and velocity are reduced for an equivalent g. In addition, the curves tend to develop a plateau (e.g. $2r_0 = 100$ μm) of relatively constant velocity as they approach the limiting case of a solid growing into an infinite liquid bath. On the other hand, as r_0 decreases, the interface undercooliny should approach the Newtonian behavior.

The extent of rapid solidification can now be determined by the fraction solidified before the interface reaches a critical
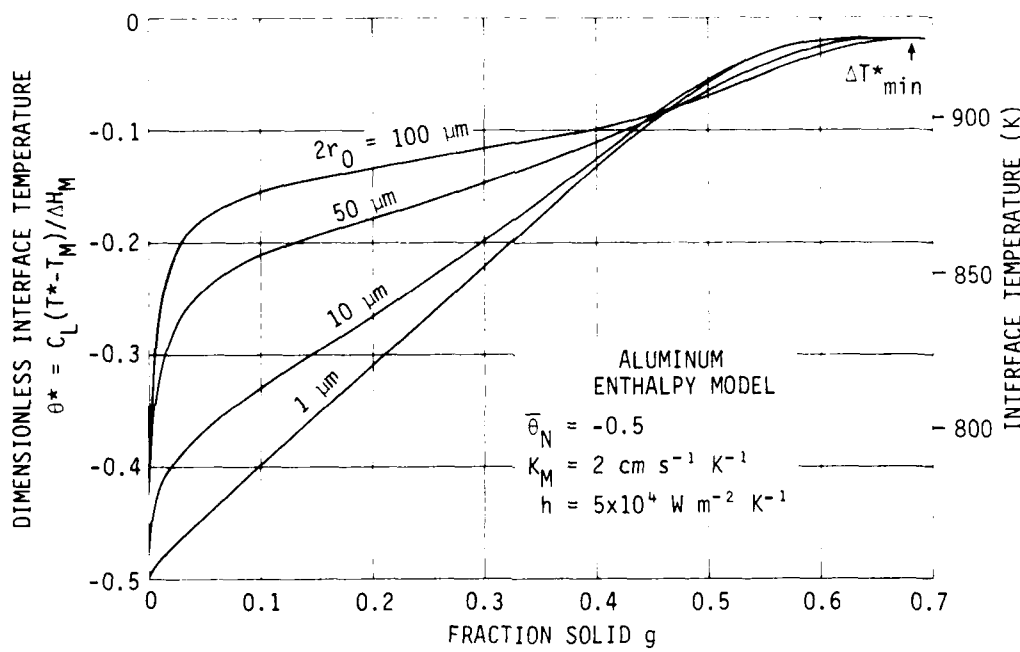
Figure 26. Effect of the particle size on the interface
temperature during solidification. As recalescence
progresses the influence of r_0 is diminished, and the
minimum undercooling is practically the same for all
particles.

undercooling ΔT_C necessary to produce the desired modification in the microstructure. The metastable effects will only be present throughout the particle if the minimum undercooling characteristic of the post-recalescence stage (i.e. ΔT^*_{min} in Figure 26) is always larger than ΔT_C. This minimum undercooling is fairly independent of particle size and close to the Newtonian value for $r_0 < 100$ μm.

Figure 27 compares the position, shape and velocity of the liquid solid interface as solidification progresses, for 1,10 and 100 μm Al droplets and the corresponding Newtonian limit. As expected, the growth velocities increase as the radius decreases, and the values for a 1 μm particle are almost identical to those calculated from the Newtonian model (the interface and droplet undercoolings have similar values). Note, however, that the Biot number at which this agreement occurs is 2.8 x 10^{-4}, far below the conventional criterion for the achievement of Newtonian conditions (Bi < 0.1). Analysis of this figure also reveals that the numerically calculated interface profiles are similar to the spherical configuration assumed in the Newtonian model.

The interfacial shape is basically dictated by the velocity distribution along the solid front. If the undercoolings are fairly uniform the interface is expected to be convex towards the liquid because the distances traveled from the nucleation point are basically constant for each time increment. However, if substantial temperature gradients are present in the droplet prior to nucleation, (e.g. large r_0 and h values), and the
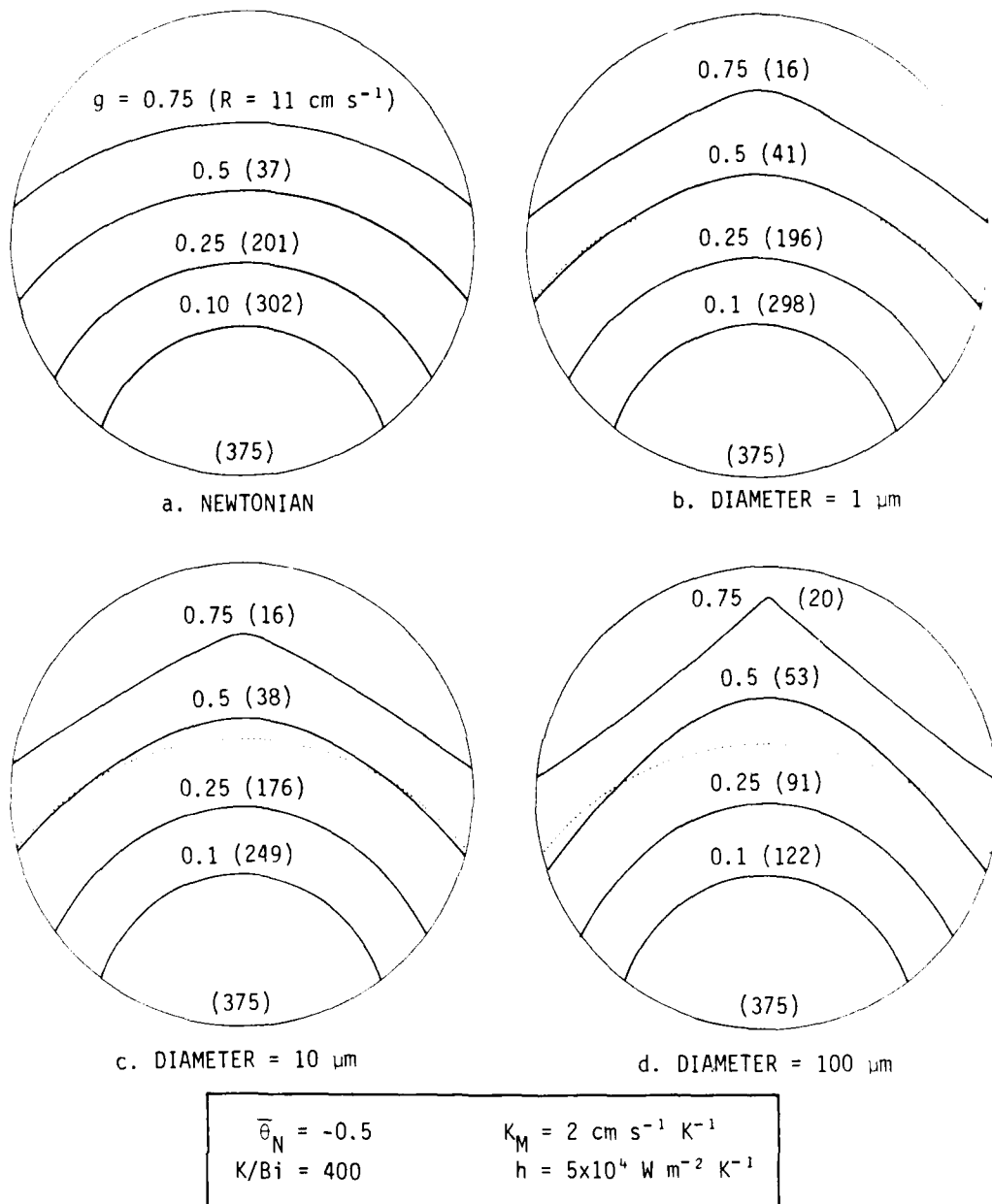
Figure 27. Interface profiles and velocities predicted from the Enthalpy model for undercooled solidification. The deviations from the Newtonian velocity limit increase with particle size, but the profiles for the recalescence stage are quite close in both models for $r_0 < 100$ μm.

initial undercooling is small, the solid growing along the symmetry axis faces a superheated liquid whereas that growing along the surface faces a supercooled liquid and also "feels" more the external cooling. It is then expected that the interface will become concave and eventually approach the case of no-undercooling analyzed in Chapter 7. Figure 28 shows the transition from a convex to a concave solid front as θ_N is reduced and r_0 is increased above 100 μm. In addition, increasing K_M will further magnify the concavity. In the limit, then, the droplet should get covered very rapidly with a solid "shell" after nucleation, and growth would proceed in the concentric pattern discussed before.

In closing this section, it should be noted that the same effects obtained by changing the particle radius are produced if the heat transfer and kinetic coefficients are proportionally increased or decreased, keeping the K/Bi ratio constant. Furthermore, the Biot number at which the numerical and Newtonian velocities converge will be dependent on the kinetic coefficient and initial undercooling.

8.2.2 Effects of the heat transfer coefficient

Increasing the heat transfer coefficient at constant K_M and r_0 enhances the role of the external cooling during recalescence, and displaces the $\bar{\psi}-\bar{\theta}$ curve following the trend established in the Newtonian analysis. As previously indicated, the two models

a. $2r_0 = 100$ μm
   $\overline{\theta}_N = -0.25$
   $K_M = 2$ cm s^{-1} K^{-1}

b. $2r_0 = 1000$ μm
   $\overline{\theta}_N = -0.25$
   $K_M = 2$ cm s^{-1} K^{-1}

c. $2r_0 = 1000$ μm
   $\overline{\theta}_N = -0.01$
   $K_M = 2$ cm s^{-1} K^{-1}

d. $2r_0 = 1000$ μm
   $\overline{\theta}_N = -0.01$
   $K_M = 50$ cm s^{-1} K^{-1}
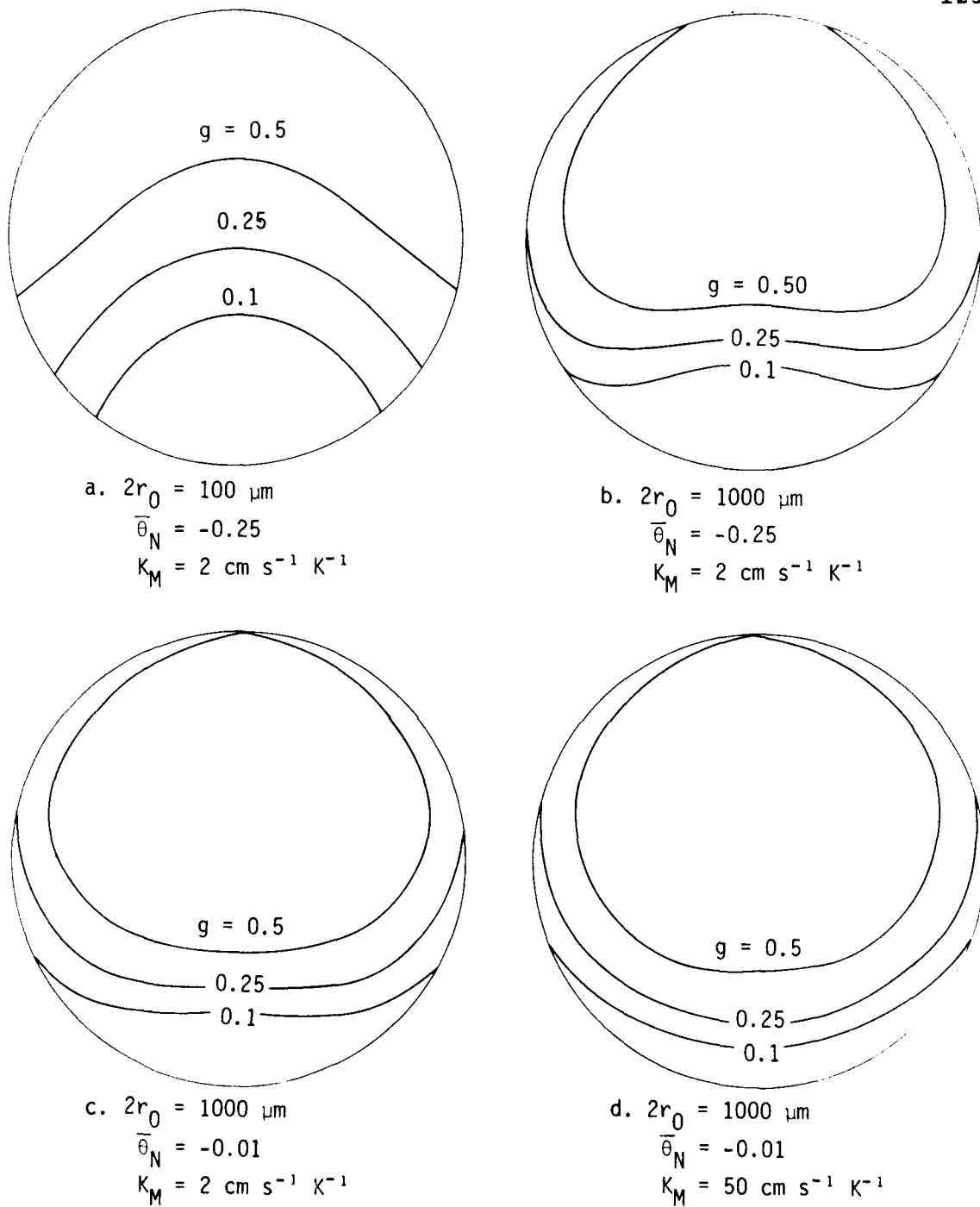
Figure 28. Transition from convex to concave interface profiles is produced by increasing the particle size (a-b), reducing the initial undercooling (b-c) and increasing the kinetic coefficient (c-d). In the limit, the interface tends to the concentric shape assumed in the no-undercooled solidification model.

diverge in their prediction of the thermal history, but the magnitude of this deviation becomes relatively insensitive to h as r_0 decreases below 100 μm. It was also noted that changes in the heat transfer coefficient do not alter significantly the maximum temperature differences $\Delta(T)$ developed inside the droplet. For example, the maximum $\Delta(T)$ in a 10 μm Al droplet with an initial undercooling of 182 K ($\theta_N = -0.5$) and a kinetic coefficient $K_M = 2$ cm s^{-1} K^{-1} decreases from 54 to 47 as h is reduced from 2×10^5 to 2×10^3 W m^{-2} K^{-1} (K/Bi = 10^2 and 10^4 respectively).

Table 13

Effect of the Heat Transfer Coefficient on the Interface Velocities (cm s^{-1}) [†]

Fraction solid, g	h (kW m^{-2} K^{-1})		
	200	20	2
0.1	266 (323)	236 (292)	233 (289)
0.3	192 (204)	135 (149)	126 (142)
0.5	111 (102)	21 (18)	3.1 (3.1)
Minimum velocity	62 (46)	5.4 (4.3)	0.5 (0.4)

[†] $2r_0 = 10$ μm, $\Delta T_N = 182$ K, $K_M = 2$ cms^{-1}K^{-1}
Values in parenthesis are the Newtonian results.

Figure 29 illustrates the effect of h on interface undercooling as a function of fraction solid, whereas Table 13 gives examples of the corresponding interface velocities. As expected from the Newtonian analysis, the role of the heat transfer coefficient is larger as solidification progresses, because the growth rate (and hence the release of latent heat) is slowed down as the interface recalesces. In general, the fraction of material solidified above a certain velocity increases with h, but the effect is only important beyond a relatively large value (e.g. 2×10^4 W m^{-2} K^{-1} in this figure). Furthermore, the heat transfer coefficient is more influential on the minimum undercooling ΔT^*_{min}, which increases in a direct proportion to h. It is expected that the importance of h during recalescence will be magnified as the droplet size increases and the kinetic coefficient or initial undercooling are diminished.

8.2.3 Effects of the kinetic coefficient

Increasing the kinetic coefficient K_M at constant h and r_0 reduces the role of the external cooling on the thermal history, in agreement with the trend previously indicated by the Newtonian analysis. The differences between the $\bar{\psi}-\bar{\theta}$ curves predicted by the two models are small for the range of values of interest. However, it was found that changes in K_M significantly alter the temperature profiles and maximum $\Delta(T)$ developed during recalescence, as shown in Figure 30. For example, increasing the
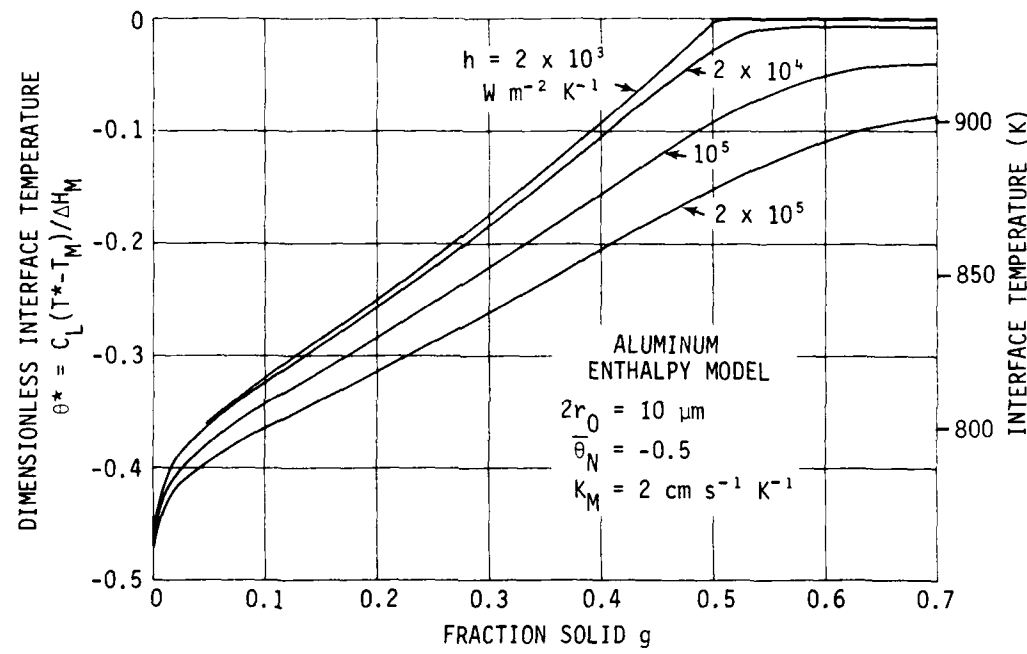
Figure 29. Dependence of the interface temperature on the heat transfer coefficient during solidification. The curves are insensitive to h below 2 kW m^{-2} K^{-1} for these particular values of r_0, θ_N and K_M. Note that h becomes more relevant in the post recalescence stage.
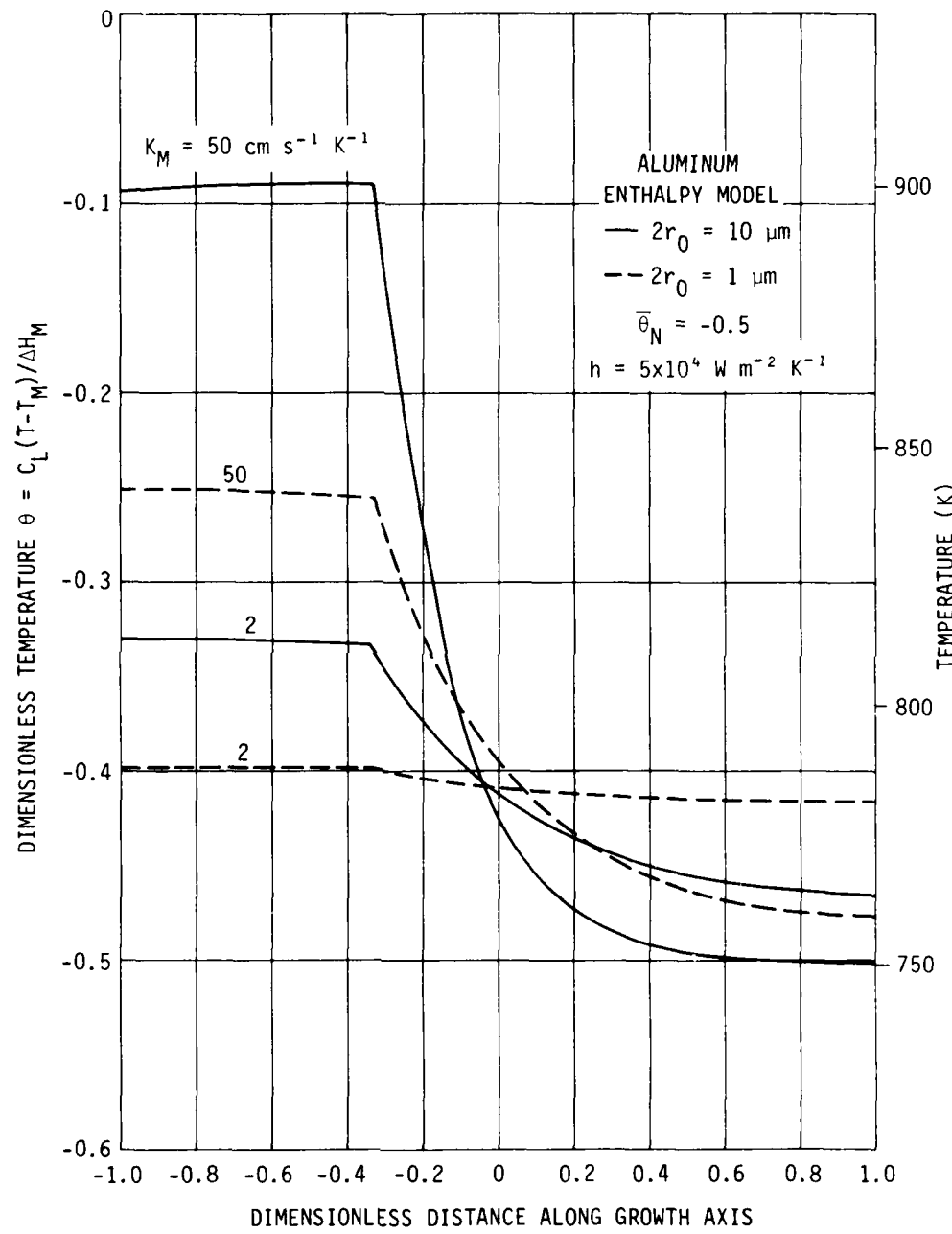
Figure 30. Temperature profiles as a function of the kinetic coefficient and particle radius for a constant fraction solid g=0.1.

kinetic coefficient from 2 to 50 cm s^{-1} K^{-1} increases the maximum

temperature difference inside a 1 μm droplet from 7 to 82 K, and

in a 10 μm droplet from 52 to 154 K, for an initial undercooling

of 182 K ($\theta_N = -0.5$).

The influence of K_M on the interfacial temperature during

solidification is shown in Figure 31, and the corresponding

velocities are given in Table 14.

Table 14

Effect of the Kinetic Coefficient
on the Interface Velocities (cm s^{-1}) [†]

Fraction solid, g	K_M (cm s^{-1} K^{-1})		
	2	8	50
0.1	240 (294)	640 (1163)	1456 (7221)
0.3	146 (159)	405 (548)	1074 (3555)
0.5	41 (37)	64 (51)	127 (79)
Minimum velocity	14 (11)	14 (11)	12 (11)

[†] $2r_0 = 10$ μm, $\Delta T_N = 182$ K, $h = 5 \times 10^4$ W$m^{-2}K^{-1}$
Values in parenthesis are the Newtonian results.

For a fixed ΔT_N the initial velocity is purely controlled by the

growth kinetics (i.e. K_M and kinetic model), and therefore

independent of the heat flow. On the other hand, the minimum

velocity characteristic of the post recalescence stage is nearly
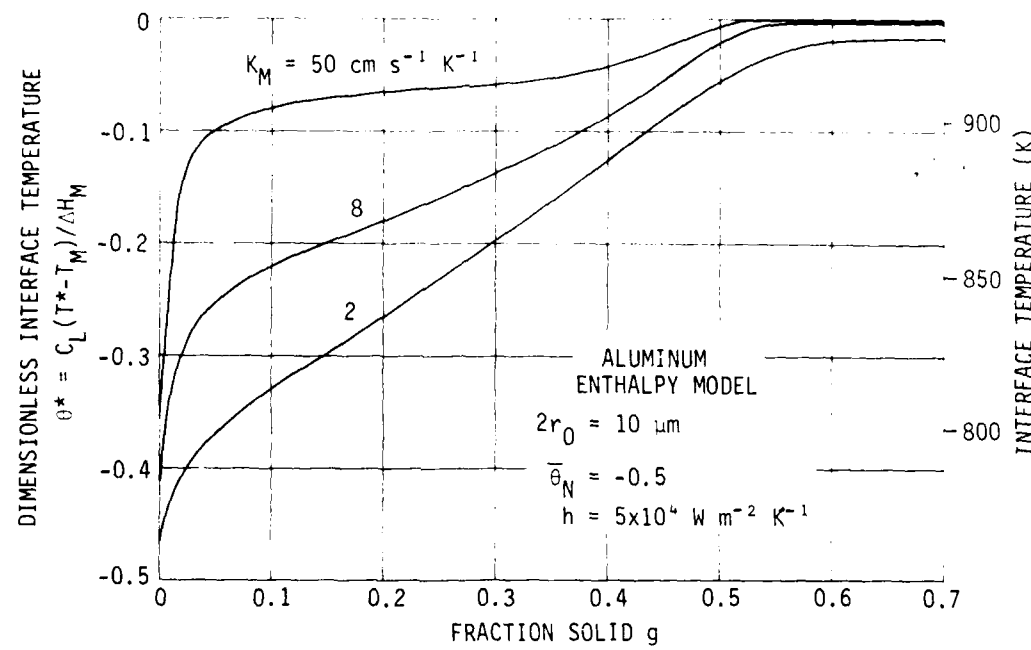
Figure 31. Effect of the kinetic parameter on the interface undercooling during solidification. Although K_M decreases ΔT^* at a particular fraction solid, the actual velocity increases.

independent of the K_M value and close to the Newtonian prediction, meaning that the interface adjusts its undercooling to satisfy the conditions prescribed by the surface cooling. During recalescence, the interface goes through a transition between the above situations. It alters both its undercooling and the thermal field in its vicinity (i.e G_L and G_S) in order to accomodate the latent heat released by the growth process.

Analysis of Table 14 reveals that the interface velocities calculated from the Enthalpy model are markedly less sensitive to the value of the kinetic coefficient than those obtained from the Newtonian simulation. This result arises from the limitations to heat flow inside the droplet (finite thermal conductance) which lead to the "local" recalescence of the interface. As K_M increases the system tends to develop a regime of steady state growth, resembling the case of solidification into an infinite liquid pool. It is then concluded that increasing K_M decreases the Biot number at which the Newtonian model provides a good estimate of the interface velocities. Furthermore, it is expected that the effects of K_M will be enhanced by reducing the particle size or increasing the initial undercooling and heat transfer coefficient.

8.2.4 Effects of the nucleation temperature

Increasing the undercooling level prior to nucleation is perhaps the most efficient way of improving the extent of rapid

solidification, as concluded from the Newtonian analysis. The $\bar{T}$-$\bar{n}$ curve calculated from the numerical model progressively shifts towards the corresponding Newtonian curves as ΔT_N decreases. Furthermore, increasing ΔT_N magnifies the temperature gradients inside the droplet at a given fraction solid during recalescence, as shown in Figure 32. Maximum temperature differences of 25 and 94 K were calculated for 10 μm Al droplets with initial undercoolings of 191 and 364 K respectively, given the K_M and h values of this figure.

Table 15

Effect of the Nucleation Temperature
on the Interface Velocities (cm s^{-1})[†]

Fraction solid, g	Average Nucleation Temperature		
	-0.25	-0.50	-1.0
0.01	154 (189)	306 (371)	634 (742)
0.25	45 (45)	169 (198)	466 (553)
0.50	13 (11)	41 (40)	341 (364)
1.00	95 (36)	95 (36)	110 (54)

[†] $2r_0 = 10$ um, h = 5×10^4 Wm^{-2}K^{-1}, $K_M = 2$ cms^{-1}K^{-1}
Values in parenthesis are the Newtonian results.

Figure 33 shows the interfacial undercoolings during solidification for several θ_N values and two kinetic models.
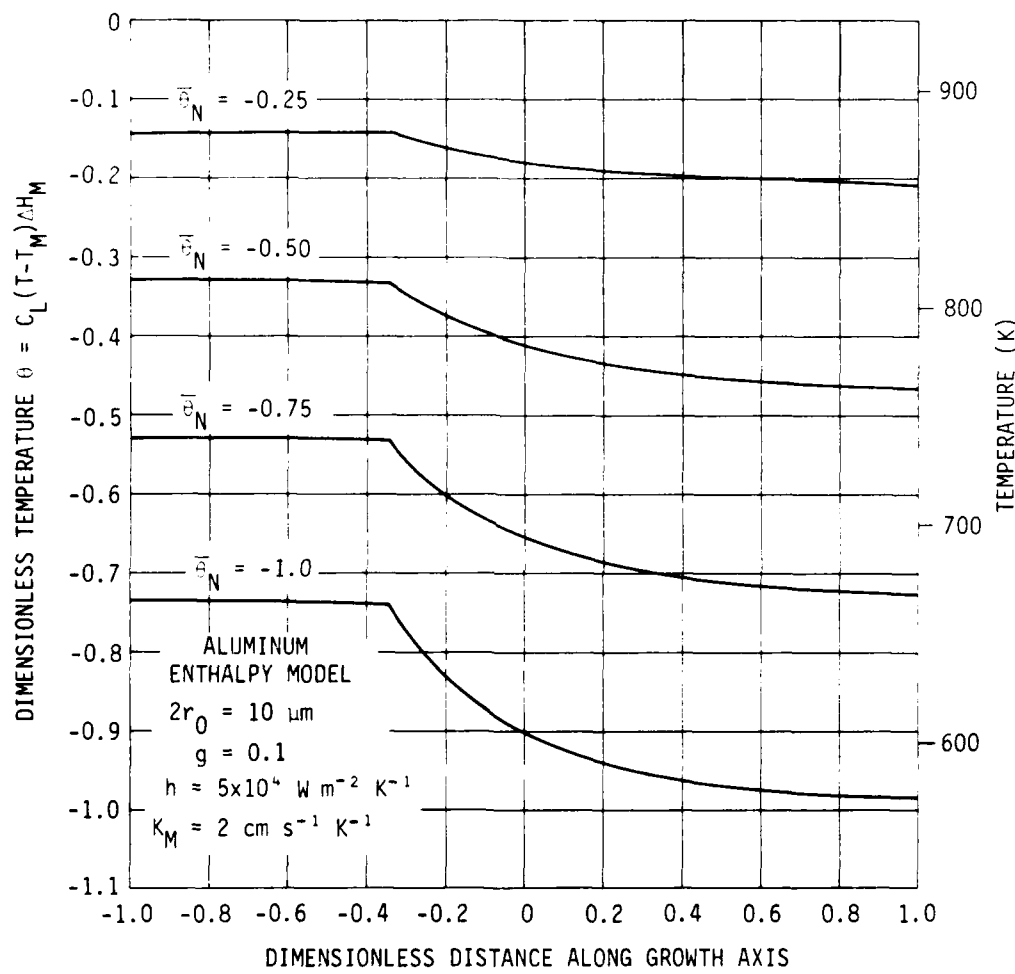
Figure 32. Temperature profiles as a function of initial
undercooling for a fraction solid g=0.1.
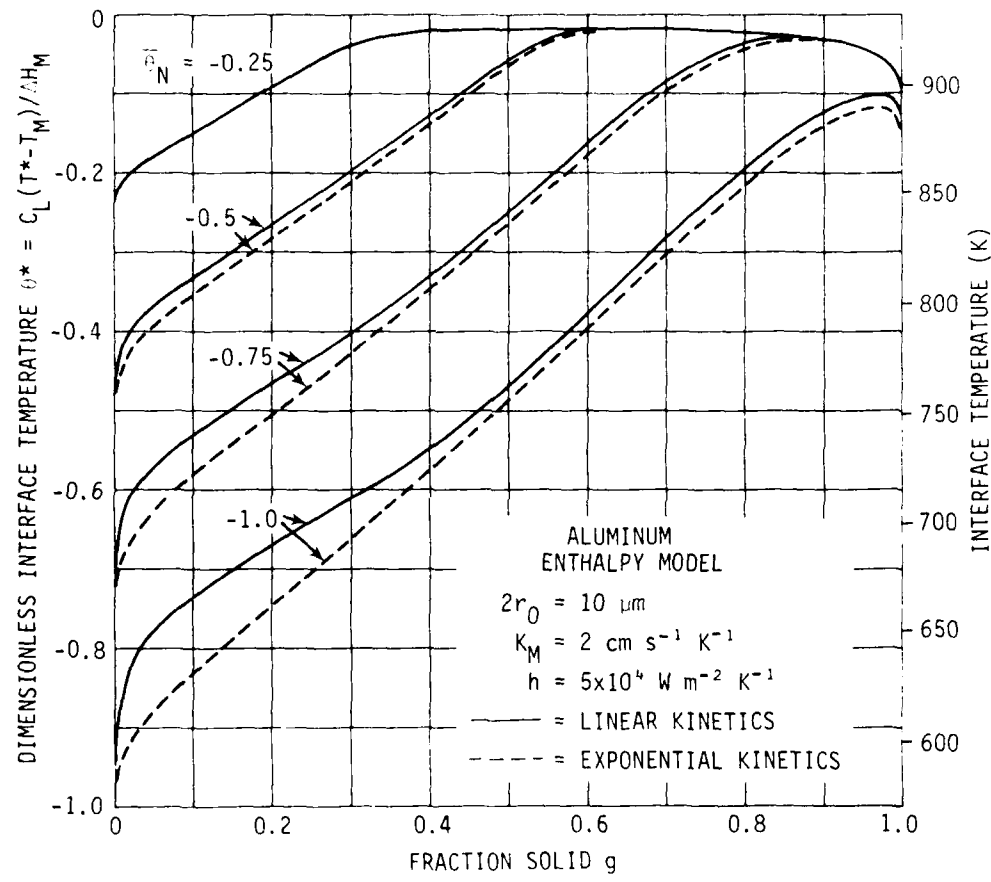
Figure 33. Effect of the initial undercooling and kinetic model
on the interface temperature during solidification.
Note that decreasing θ_N always increases the fraction
solidified below a certain temperature.

Examples of the corresponding interface velocities are given in Table 15. It is evident from this figure that the amount of material solidified above a critical undercooling ΔT_C markedly increases as nucleation is suppressed to larger undercoolings. The local recalescence is also faster as θ_N decreases due to the consequent increase in the driving force for solidification. However, the assumption of an exponential kinetic law reduces this effect because it consistently predicts lower velocities than the linear law for a given temperature. As in the Newtonian case, the kinetic models tend to produce similar results as the undercooling is reduced. Finally, it is expected that reducing K_M and r_0, as well as increasing h will enhance the role of the initial undercooling on the recalescence behavior of the droplets.

CHAPTER 9

MICROSTRUCTURAL ANALYSIS

Aluminum alloy powders were produced in external facilities
from ingots made in our laboratories, and their microstructures
examined by Transmission (TEM) and Scanning Electron Microscopy
(SEM). Determination of lattice parameters was also performed on
some samples by X-ray diffractometry.

Most of the studies were focused on the Al-Si system, using
alloys of 3 and 6% Si, as well as a high purity (99.999%)
aluminum standard. Some supplementary observations were made on
Al-4.5%Cu. The alloys were prepared from Al ingot (99.97%), Cu
plate (99.95%) and Si lumps (99.98%) by melting batches of 20 kg
in a clay-graphite crucible, degassing with chlorine and casting
in sand or graphite molds, depending on the projected atomization
technique.

9.1 Atomization

Powder samples were produced by two different methods,
namely, electrohydrodynamic atomization in vacuum (Phrasor
Scientific EHD process) and high speed centrifugal atomization in
helium (Pratt and Whitney RSR process). These techniques have
been extensively discussed elsewhere [77,90,91] and are briefly
described in what follows.

9.1.1 Electrohydrodynamic atomization (EHD)

The EHD method for droplet generation involves the application of very intense electric fields on a conductive liquid at the tip of a capillary nozzle (emitter). The molten metal, contained in a pressurized ceramic reservoir, is given a positive potential (usually +10kV) while delivered to the nozzle, typically of 50 μm in diameter. The emmiter is exposed to a negative (-1 kV) annular electrode (extractor), concentrating the electric field on the very small liquid meniscus. The interaction of the electrostatic stresses with the surface tension forces produces a liquid spike that breaks into charged droplets. These are then accelerated by the voltage difference and fly through the orifice in the extractor to be collected on a target after solidification. Velocities above 200 m s^{-1} have been reported for particles below 1 μm in diameter, with calculated times of flight lower than 2.5 ms [91].

The atomizer is enclosed in a vacuum chamber (10^{-5} torr), thereby restricting the heat loss from the droplets to radiation ($h \leq 100$ W m^{-2} K^{-1}). Maximum cooling rates prior to solidification are estimated to range from 9.6 x 10^4 K s^{-1} at the melting temperature, to 1.3 x 10^4 K s^{-1} at the onset of hypercooling, for a 1 μm droplet of aluminum with an emissivity e = 1. Actual values may be lower by more than one order of magnitude if we consider the e values reported in the literature and mentioned in Chapter 3. In addition, the cooling rates for a

100 μm particle will be two orders of magnitude lower, as indicated by Equation (6.4).

EHD powders range in size from less than 100 nm to about 100 μm. They were collected by deposition on a 125 μm thick plastic tape (of the type used to prepare electron microscopy replicas) placed on the target. By appropriate manipulation of the process variables, the substrate may be covered with a monolayer consisting mostly of submicron powders. Particles larger than ~10 μm are usually limited in number, presumably because they bounce off or are later detached from the tape. This loose material is gathered from the chamber at the end of the experiment.

Figure 34 shows a typical sample of powders as received on the plastic substrate. They are nearly spherical and have smooth surfaces, although some appear to have solidified on the tape. Mainly intended as a laboratory tool, this process is able to produce only a few grams of material per hour. Nevertheless, it has proven to yield a substantial number of samples under reproducible conditions, making it specially suitable for fundamental solidification studies.

9.1.2 Centrifugal atomization (RSR)

The RSR (for Rapid Solidification Rate) process for the production of metal powders is based on a turbine-driven atomizer capable of reaching velocities in excess of 24000 rpm. The
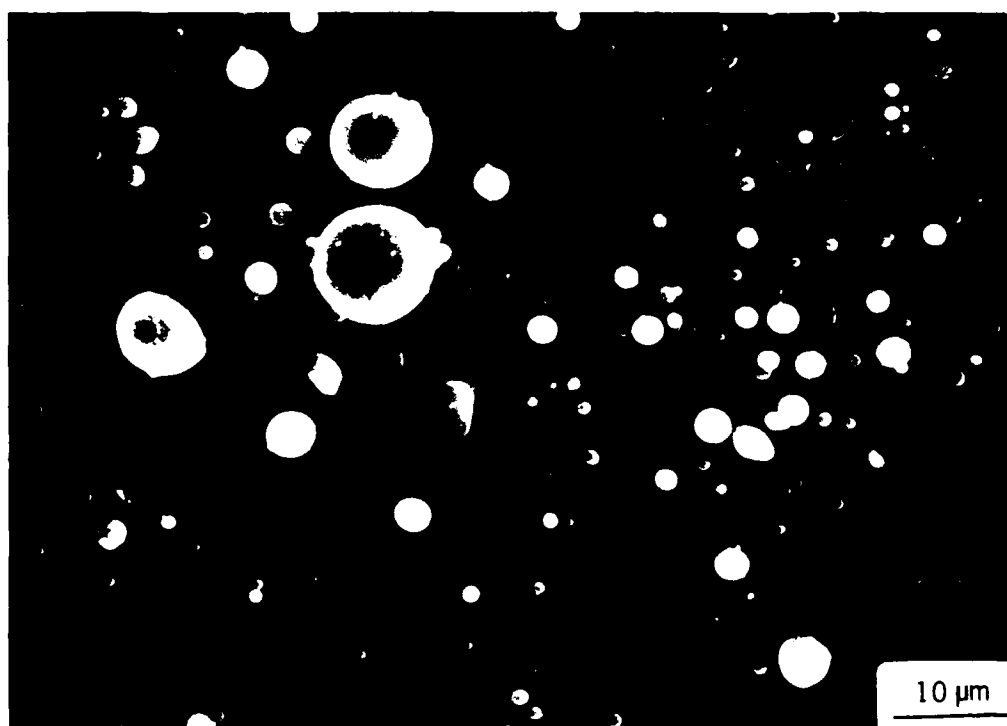
Figure 34. SEM view of Al-4.5%Cu powders produced by
electrohydrodynamic atomization.

atomizer consists of a water cooled copper disc, 7.5 cm in diameter, rotating about a vertical axis and enclosed into a helium filled chamber. A controlled stream of liquid metal is poured near the center of the disk, spreading into a layer due to the centrifugal acceleration. At the edge, the liquid breaks down into droplets with tangential velocities of the order of 100 m s^{-1}. These are then quenched by a large cross-flow of helium injected into the chamber, and the solid powders are collected from the gas exhaust line.

Convection is then the dominant mechanism of heat extraction in these powders, and heat transfer coefficients above 10^5 W m^{-2} K^{-1} are claimed to be achievable by this method. Cooling rates of 6.8 x 10^8 K s^{-1} at the melting temperature and 2.9 x 10^8 K s^{-1} at the onset of hypercooling were calculated for a 1 μm droplet using the h $\cong$ 4.8 x 10^5 W m^{-2} K^{-1} given in Table 2. Note in this table that increasing the particle size to 100 μm reduces h roughly by two orders of magnitude, hence decreasing the achievable cooling rates by four orders of magnitude, as indicated by Equation (6.4).

RSR powders, shown in Figure 35, are fairly spherical in shape but with rough surfaces (as if they had undergone collisions during or after solidification). They apparently lack the "orange peel" topography typical of materials produced by atomization [92] and range in size from slightly below 1 μm to above 100 μm. Standard size classification of the Al-Si powders reveals that about 80% of the material received is smaller than
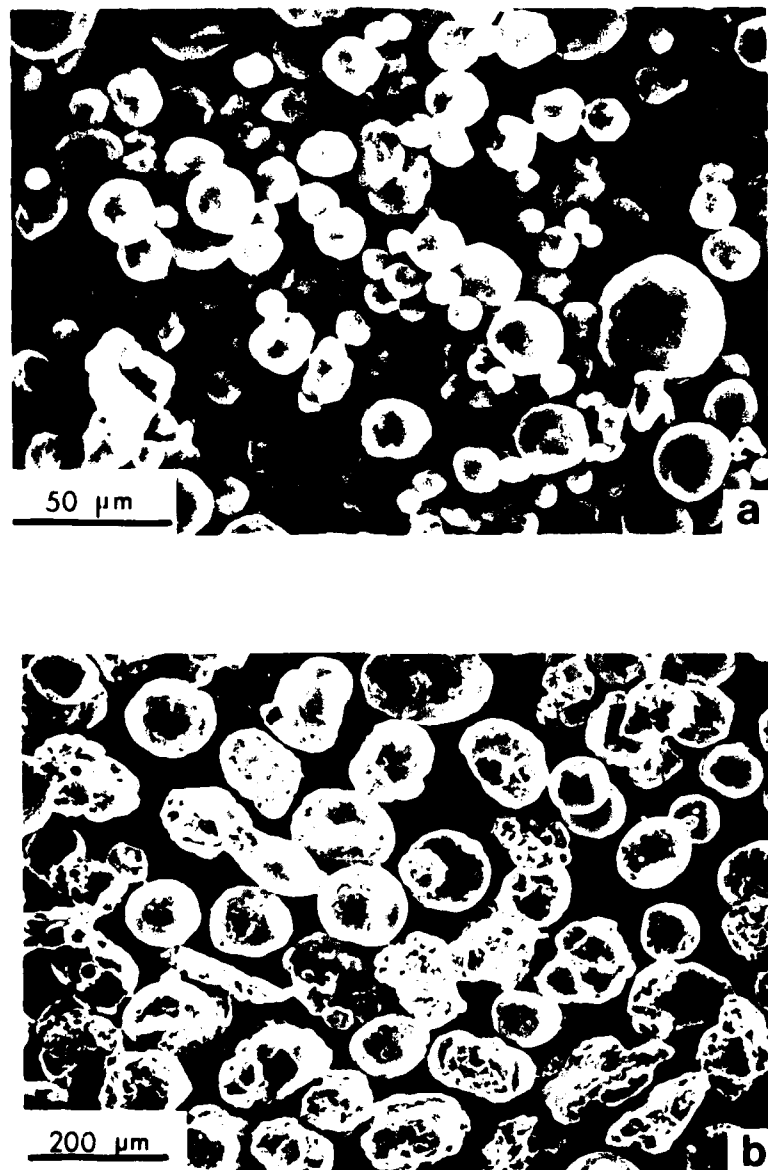
Figure 35. SEM view of Al-3%Si powders produced by centrifugal
atomization; (a) particle size below mesh 325
(<44 μm), (b) particle size between 100 and 120 mesh
(125-149 μm).

125 μm, and ~15% passes mesh 325 (<44 μm). However, SEM analysis revealed that the coarse fraction of the powders (+100 mesh) tend to be formed by conglomerates rather than individual particles. Yields of 1-2 kg are common for a batch aluminum run, but the process is aimed to produce 0.5 kg s^{-1} of material in a continuous fashion at commercial scale [77].

9.2 Specimen Preparation

Samples of pure aluminum and the three alloys were obtained from EHD atomization, but only the alloys were processed through the RSR technique. EHD powders were received on sections of the tape located on the target during atomization. Small quantities of loose particulate material containing both powders and splats were also provided for most runs. RSR powders were furnished in bulk form.

Aluminum powders below 1 μm in diameter are transparent to 200 keV electrons, and therefore lend themselves to conventional TEM analysis without further thinning. EHD specimens were prepared by cutting the tape into 3 mm discs and coating on the deposition side with a 20-50 nm film of evaporated carbon. The substrate was then dissolved in acetone and the powders remained attached to the carbon film. This was carefully rinsed in isopropyl alcohol and placed on a 3 mm, 400 mesh copper grid. The powder density was commonly about 100 particles per grid opening (~10^3 μm^2).

Preparation of TEM specimens of submicron RSR powders was achieved by separating the finest fraction (-325 mesh) from each alloy, suspending a small amount of this material in methanol, and allowing it to settle with time. Samples were taken with a thin pipet at regular intervals and a drop of each one was placed onto a 3 mm disc of blank replicating tape (previously treated to obtain a smooth surface). The operation was repeated a few times for each specimen. Once the methanol had evaporated, the discs were coated with carbon and the films recovered in the same manner described for the EHD powders. It should be noted that the density of electron-transparent material in these latter specimens was only of a few particles per disc.

Loose powders from both processes were mounted on resin, polished with diamond following standard metallographic practices and examined by SEM (25 keV). Since the atomic number contrast in the Al-Si alloys is rather poor, the as-polished sections were etched in 1% NaOH for 90 seconds to enhance the surface topography.

9.3 Results and Discussion

The powders were divided for their study in submicron and conventional (>10 μm) material. Although the former are not of commercial importance, their electron-transparency permits the three-dimensional examination of a complete solidification structure. Furthermore, our analysis revealed that substantial

undercolings were achieved in most submicron droplets prior to nucleation, and the resulting microstructures were in agreement with the trends predicted by the heat flow model.

9.3.1 *EHD submicron powders*

The observations resulting from the analysis of EHD powders will be presented depending on whether they pertain to their segregation or their nucleation behavior. For the purposes of the ensuing discussion, we will call segregates those second phases originating from the melt, whereas precipitates will refer to phases formed after solidification.

Most of the Al-Si EHD powders conform to a variant of the *basic segregation pattern shown in Figure 36.* The microstructure exhibits a region (A) containing a uniform distribution of very fine precipitates or clusters of Si which, according to the diffraction evidence, have an orientation relationship to the primary Al phase. Dark field imaging of precipitates slightly coarser than those in the present figure suggest that they are either needles or platelets on the {111} Al planes. This finding is consistent with the decomposition kinetics of Al-Si solid solutions; the plates evolve from spherical clusters and needles that form in the early stages of precipitation [31-36]. It was then concluded that this zone was originally a supersaturated solid solution.
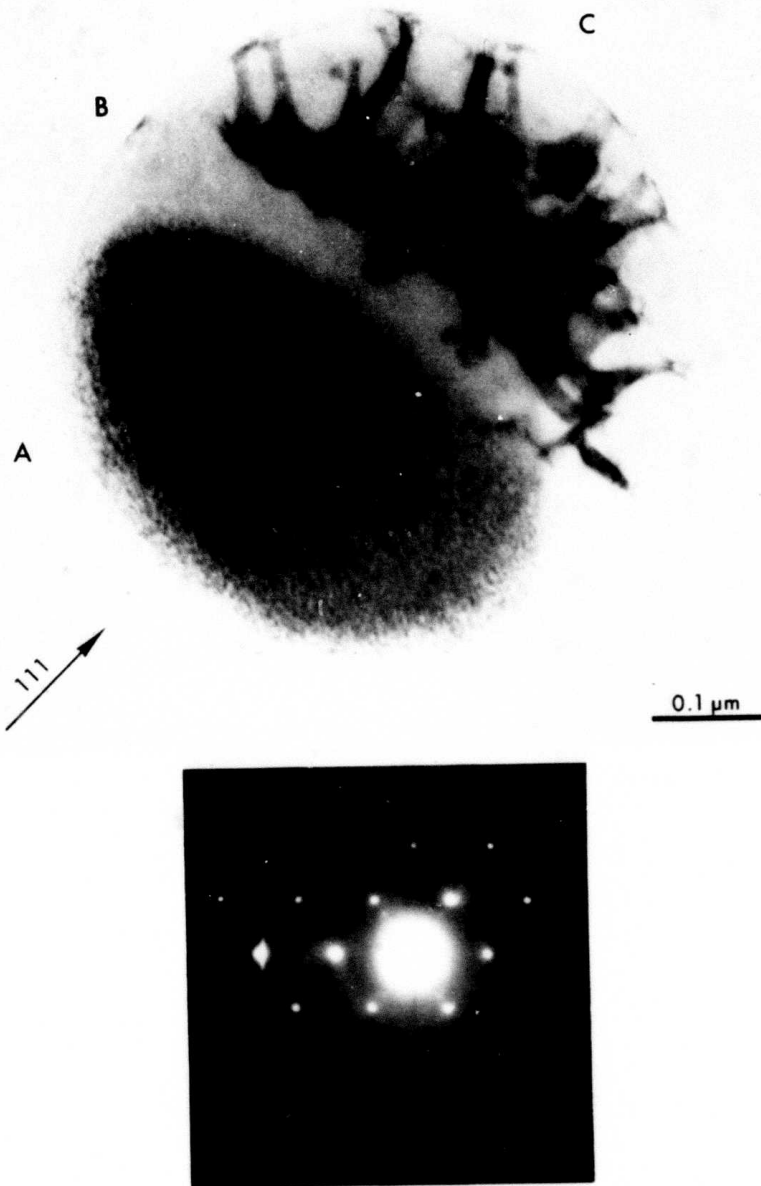
Figure 36. Typical segregation pattern for an Al-6%Si EHD submicron particle ($2r_0 > 0.5$ μm) showing 3 distinct regions. The initially rapid solidification produces a supersaturated zone (A), which breaks later into cells (C) after the droplet recalesces. (B) is a transition zone where solute builds up in front of the interface. The growth axis is close to a <111> direction.

Region (A) is followed by a precipitate-free zone (B), whose configuration closely resembles the axisymmetric geometry discussed in the heat flow analysis and depicted in Figure 27. The boundary between regions (A) and (B) corresponds to the trace of the solidification front, which is symmetric about the growth axis. The latter was consistently found to be close to a <111> direction.

Finally, the particle in Figure 36 also has a well developed cellular region (C), with segregate spacings in the order of 0.1 μm. Similar structures in Al-4.5%Cu, shown at a different angle in Figure 37, reveal more clearly the cellular pattern.

Figure 38 illustrates the effect of particle size on the extent of the different zones in the segregation pattern. As the diameter decreases, the cellular structure becomes less defined (b), and eventually disappears, leaving only a few segregates (c). At the lower end of the size distribution, the particles appear almost featureless (d), showing only the supersaturated region (A). The intensity of the silicon spots is also reduced with diminishing diameter, although the crystallographic relationship remains.

The structures in Figure 38 are by no means restricted to a particular size range. For example, segregate-free powders as large as 1 μm were found in some instances, and segregated Si was detected in some of the smallest particles. The trend illustrated in this figure was established from the TEM analysis of over 400 particles between 0.1 and 1.0 μm for each Al-Si

0.2 μm
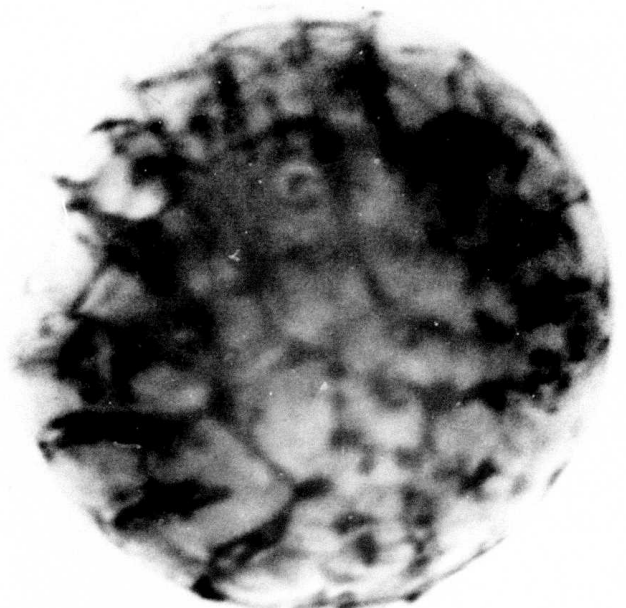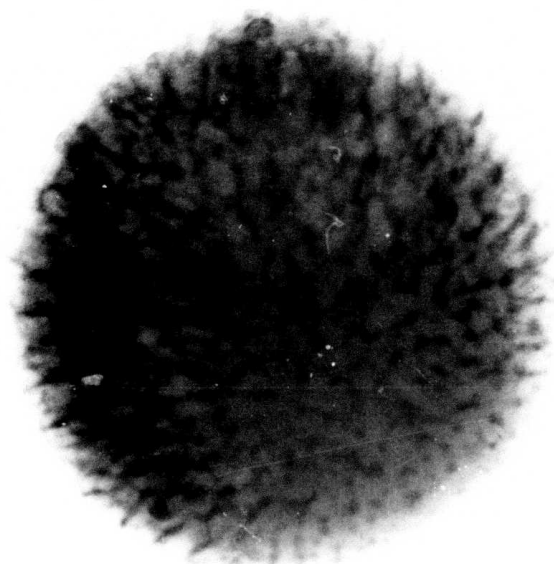
0.2 μm

Figure 37. Cellular structures observed in Al-4.5%Cu EHD powders by TEM.
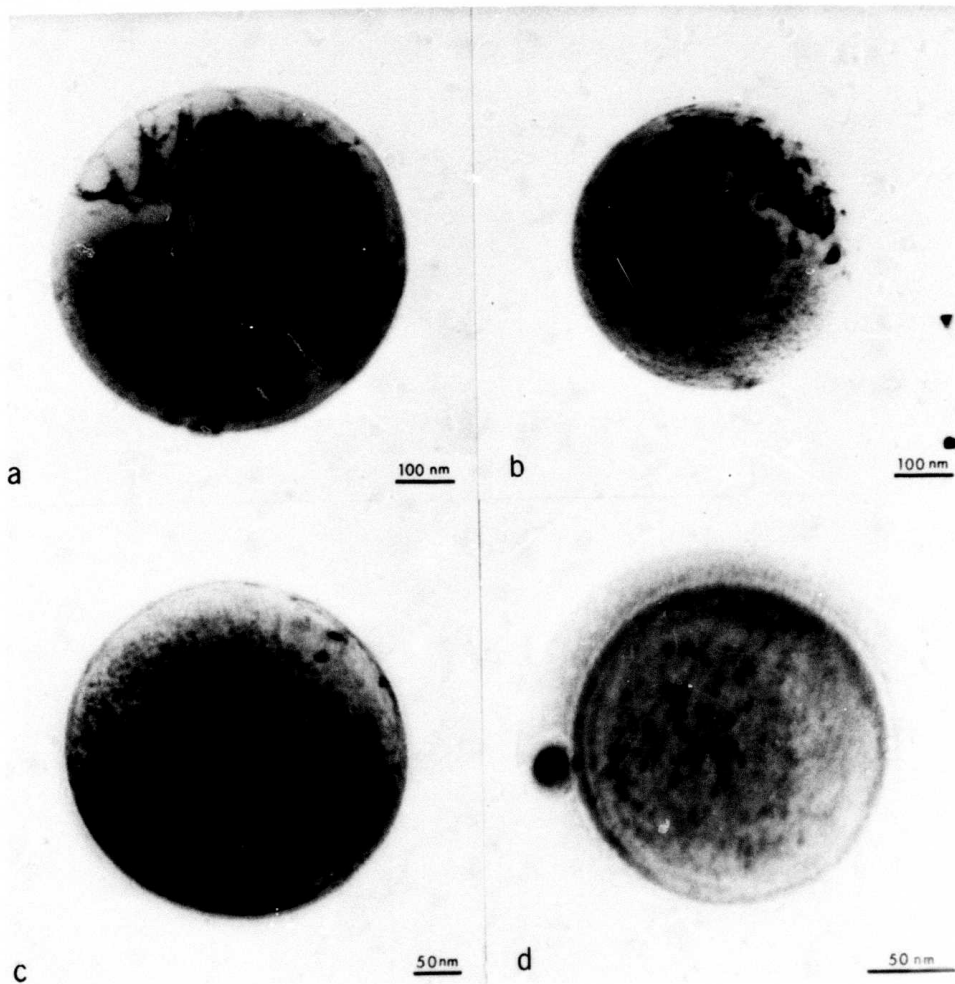
Figure 38. Transition from a partially segregated structure to a
homogeneous one as particle size decreases. The
diameters of the powders shown are (a) 570 nm,
(b) 470 nm, (c) 220 nm and (d) 170 nm.
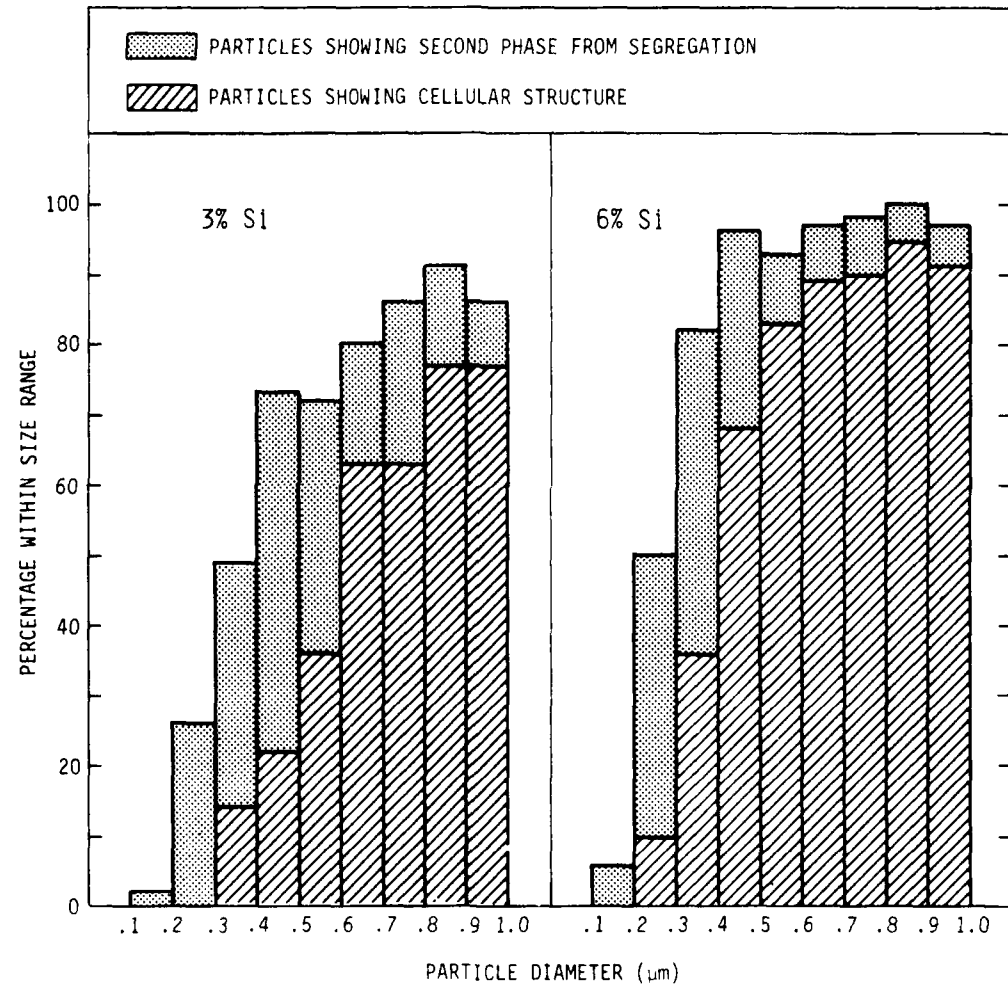
Figure 39. Segregation behavior of aluminum-silicon submicron powders produced by EHD. Results are from over 400 particles in each alloy composition.

composition. The results, given in Figure 39, confirm that increasing the particle size or the solute content enhance the incidence of segregation. Since not all of the segregated powders exhibit a cellular pattern (see, for example, Figures 38(c) and 40), the occurrence of the latter has been also plotted in Figure 39.

The previous microstructures reveal that substantial undercoolings must have been reached in the liquid droplets prior to solidification, which is believed to proceed as follows. In general, nucleation occurs at the surface, as evidenced by the growth direction. The subsequent rapid solidification into a highly undercooled liquid produces a homogeneous zone (A) of extended solubility. As the droplet recalesces, the interface velocity and undercooling are reduced, thereby decreasing the driving force for solute "trapping". When the interface temperature surpasses some critical temperature for the supersaturation process, T_c, solute is rejected ahead of the solidification front. The interface is eventually rendered unstable and breaks into cells.

The extent of homogeneous solidification can be rationalized in terms of the heat flow concepts previously developed. Assuming that the thermophysical properties are reasonably constant, the behavior of an alloy growing in a plane front mode without solute partitioning is expected to resemble that of the pure metal.

Equation (2.11) for constant specific heat indicates that the required nucleation temperature for adiabatic homogeneous solidification is

$$T_N \leq T_H = T_C - \Delta H_M/C_L \qquad (9.1)$$

where T_H is now the hypercooling temperature for an alloy.

As indicated in Chapter 2, the critical temperature for homogeneous solidification has a value between the solidus T_S and the T_O curve. For purposes of illustration, we have arbitrarily assigned to T_O the average value of T_L and T_S, and estimated on this basis an upper bound to the hypercooling temperature T_H; see Table 16. The lower bound to T_H corresponds to $T_C = T_S$. The values of θ were calculated by substituting T_L for T_M in Equation (3.12) and hence are proportional to the undercoolings.

Table 16

Effect of the Alloy Composition on the Critical and Hypercooling Temperatures[†]

		3% Si		6% Si	
		T	θ	T	θ
Liquidus	T_L	913	0	893	0
Critical	$T_C(T_O)$	848	-0.18	762	-0.36
	$T_C(T_S)$	782	-0.36	631	-0.72
Hypercooling	$T_H(T_O)$	484	-1.18	398	-1.36
	$T_H(T_S)$	418	-1.36	267	-1.72

† Estimated from the equilibrium phase diagram, T_S are from the metastable solidus. $T_O = (T_L + T_S)/2$

The values in this table indicate that dimensionless temperatures in the order of -1.18 ($\Delta T_N/T_L$ = 0.47) and -1.36 ($\Delta T_N/T_L$ = 0.55) may be necessary to eliminate segregation in aluminum alloys with 3 and 6% Si respectively. Note that the ratios of $\Delta T_N/T_L$ are much higher than the maximum of about 0.35 that has been obtained in the controlled undercooling experiments with emulsified metals [49-51].

Table 17

Extent of Rapid Solidification in Al-Si Alloys
as Fraction Solidified Below a Critical Temperature $g(\theta_C)$[†]

h ($Wm^{-2}K^{-1}$)	θ_N	Critical Temperature θ_C		
		-0.18	-0.36	-0.72
20	-1.0	0.80	0.62	0.26
(EHD)	-0.75	0.56	0.38	0.03
	-0.50	0.31	0.13	-
	-0.25	0.07	-	-
2×10^5	-1.0	0.92	0.67	0.28
(RSR)	-0.75	0.67	0.43	0.05
	-0.50	0.43	0.20	-
	-0.25	0.21	-	-

† Newtonian cooling, K_M = 2 $cms^{-1}K^{-1}$

Table 17 shows calculated Newtonian values of the fraction solidified below different critical temperatures, $g(\theta_C)$ (i.e., the extent of supersaturation), for different nucleation temperatures and heat transfer coefficients. For an h = 20 W m^{-2} K^{-1}, typical of EHD atomization, heat extraction from the droplet does not have a significant role during

recalescence, as previously shown. It is concluded from this table that the rapid solidification effects are diminished when the critical temperature decreases as a result of increasing the solute content. In addition, the achievable undercooling prior to nucleation is likely to increase as the droplet size decreases, and the initial zone of supersaturation is consequently extended until it covers the entire powder.

It should be noted that the present Newtonian data are upper limits to $g(\theta_C)$ and independent of particle size. Increasing r_0 or K_M will promote "local" recalescence of the interface and therefore reduce $g(\theta_C)$ for a given h and θ_N. Finally, one must also conclude that undercoolings near or into the hypercooled regime were obtained for those particles where segregation was absent.

Figure 39 also shows the existence of a large proportion of powders in the lower sizes that experienced segregation but no cellular breakdown. This phenomenon may simply reflect that the onset of segregation ($\Delta T^* < \Delta T_C$) occurred very late in the solidification process. Moreover, interface breakdown may also be prevented by the stabilization of short wavelength perturbations due to surface tension effects [64]; the smallest perturbation that can grow is of dimensions comparable to the particle size.

A minor proportion of the powders (<5%) exhibit quite a different type of segregation microstructure, where large faceted Si second phases appear distributed throughout the surface, as in

0.1 μm
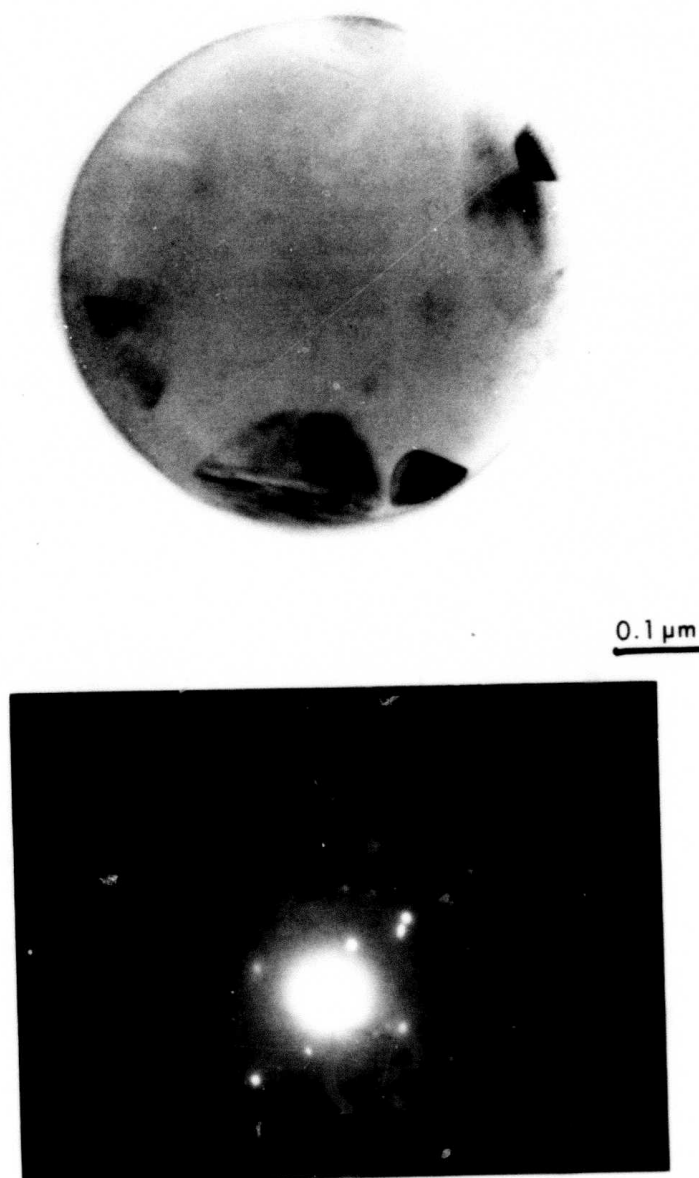
Figure 40. Anomalous morphology of Si segregates observed in some powders, especially at high Si content and large particle size.

Figure 40. Diffraction analysis did not reveal any particular orientation relationship with the matrix, but rather strong reflections of individual silicon crystals. The results indicate that these phases were probably segregation products, but the growth direction and geometry were not evident, and the supersaturated zone (A) typical of most submicron particles was apparently absent. Furthermore, this anomalous segregate morphology was not observed in the Al-Cu system, and its occurrence was more common in the larger particles and higher Si alloys.

It was concluded that powders showing the faceted silicon were unlikely to have reached substantial undercooling prior to nucleation, hence being extensively segregated. Although the absence of cells could be ascribed to interface stabilization by surface tension effects, it is not clear why most of the particles of equivalent sizes were cellular. In addition, the distribution of segregates was not consistent with an axisymmetric growth pattern, in which the Si should be accumulated on one side of the powder.

High purity aluminum submicron powders, such as those in Figure 41, do not exhibit any evidence of cellular structures that could have been originated from thermal instability due to the negative gradient in front of the interface. This observation lends support to the fact that the breakdown observed in the alloys was mainly of constitutional nature. It could also be argued that thermal cells in a pure metal would be
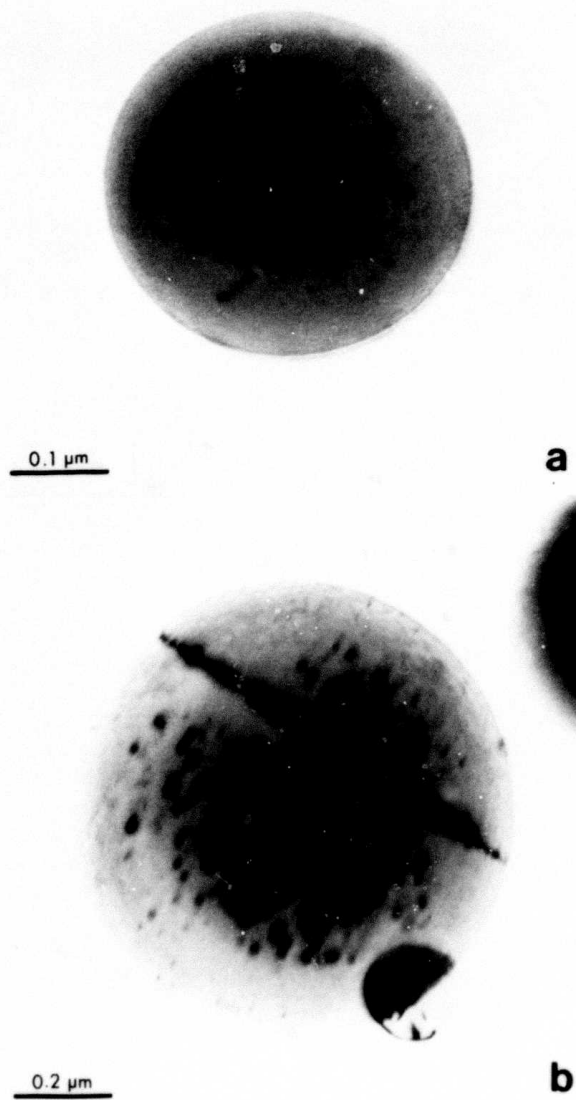
Figure 41. Typical structures in high purity aluminum (99.999%)
EHD submicron powders. (a) shows a monocrystalline
particle and (b) a set of twin crystals.

indistinguishable after solidification, unless they are decorated by impurities or strained areas caused by crystalline misorientation. Nevertheless, pure aluminum particles show some platelike features that can be interpreted either as clusters of impurities or vacancy condensation loops. The existence of denuded zones near the surface and crystal boundaries suggests that vacancies are involved in the formation of these features.

The microstructural analysis also revealed that most EHD powders are monocrystalline, indicating that nucleation was usually limited to a single event per droplet. A substantial proportion of them, however, consist of two or more crystals which could be either randomly oriented with incoherent boundaries, as in Figure 42, or twins, as in Figure 43. It was concluded that each random grain originates from an independent nucleation event, and its boundaries result from impingement with other growing crystals. On the other hand, twin crystals normally exhibit {111} coherent boundaries and are believed unlikely to be independently nucleated.

The nucleation behavior of Al-Si EHD submicron powders is quantitatively summarized in Figure 44. In general, the proportion of polycrystalline material, the number of nucleation events per particle and the incidence of twinning all increase as the powder diameter decreases below 1 μm. It was therefore concluded that larger undercoolings promote the occurrence of twins and multiple nucleation. This is consistent with the qualitative observation that polycrystalline powders are commonly

0.1 µm
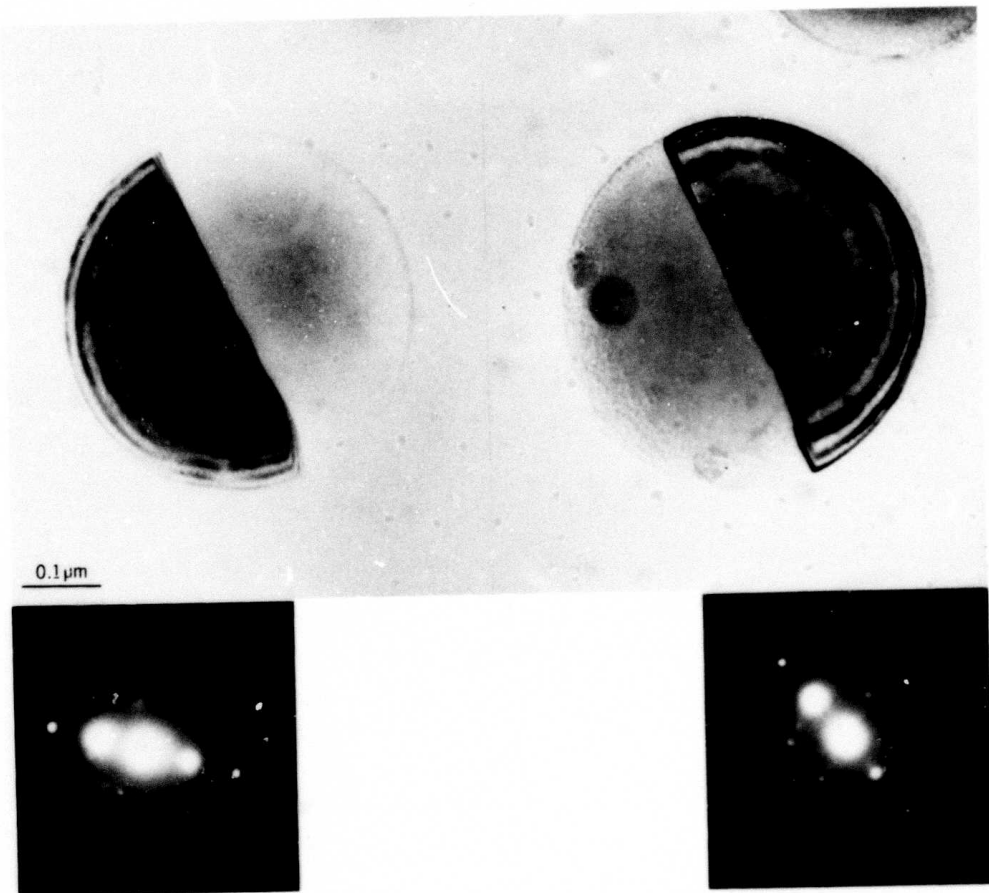
Figure 42. Typical polycrystalline powder in Al-3%Si where two
nucleation events occurred simultaneously in the
droplet and formed an impingement boundary.
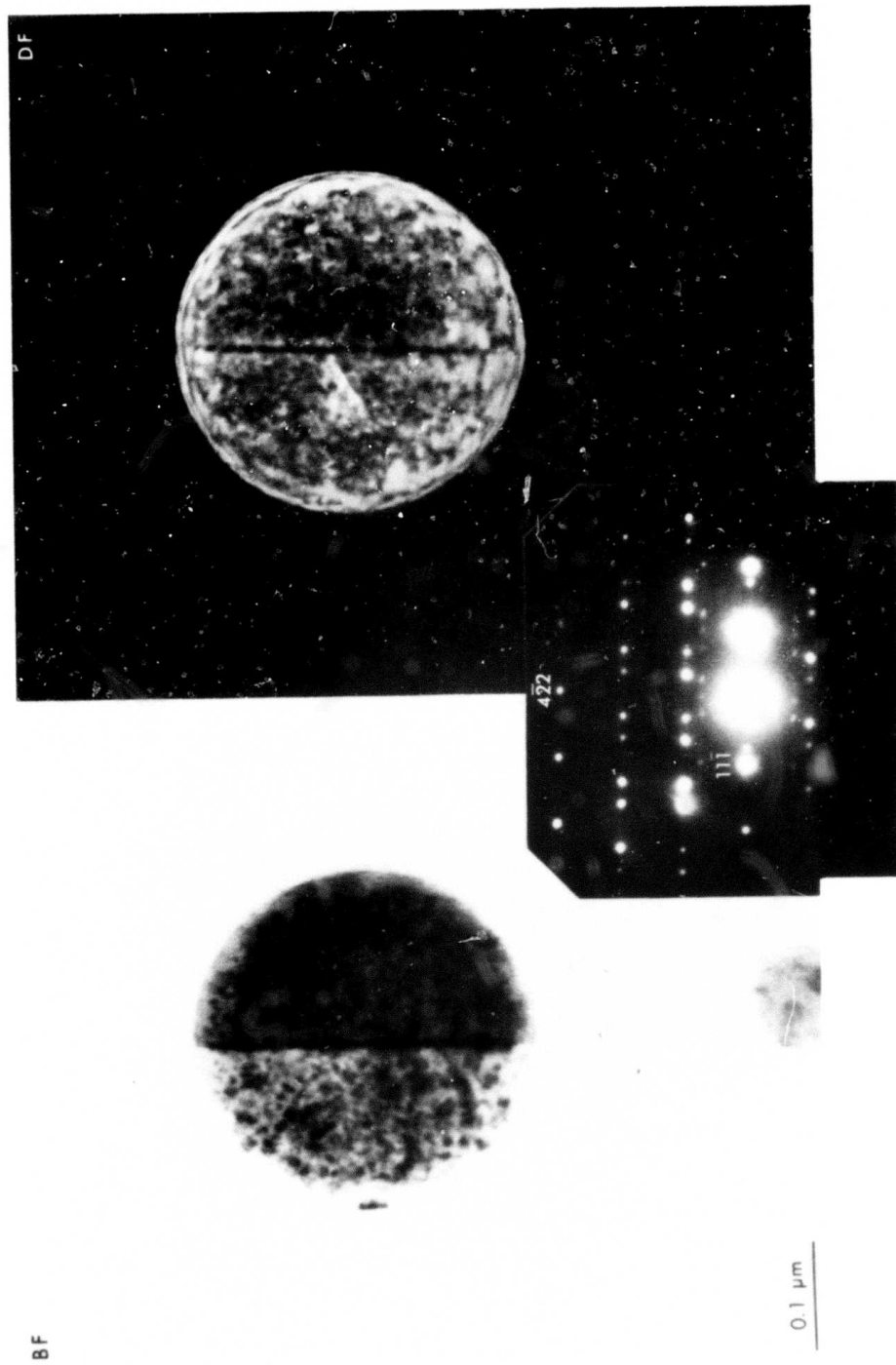
Figure 43. Twin crystals in Al-3%Si EHD powder. The electron diffraction pattern shows that the boundary is a {111} plane, apparently coherent although decorated with precipitates in some cases.
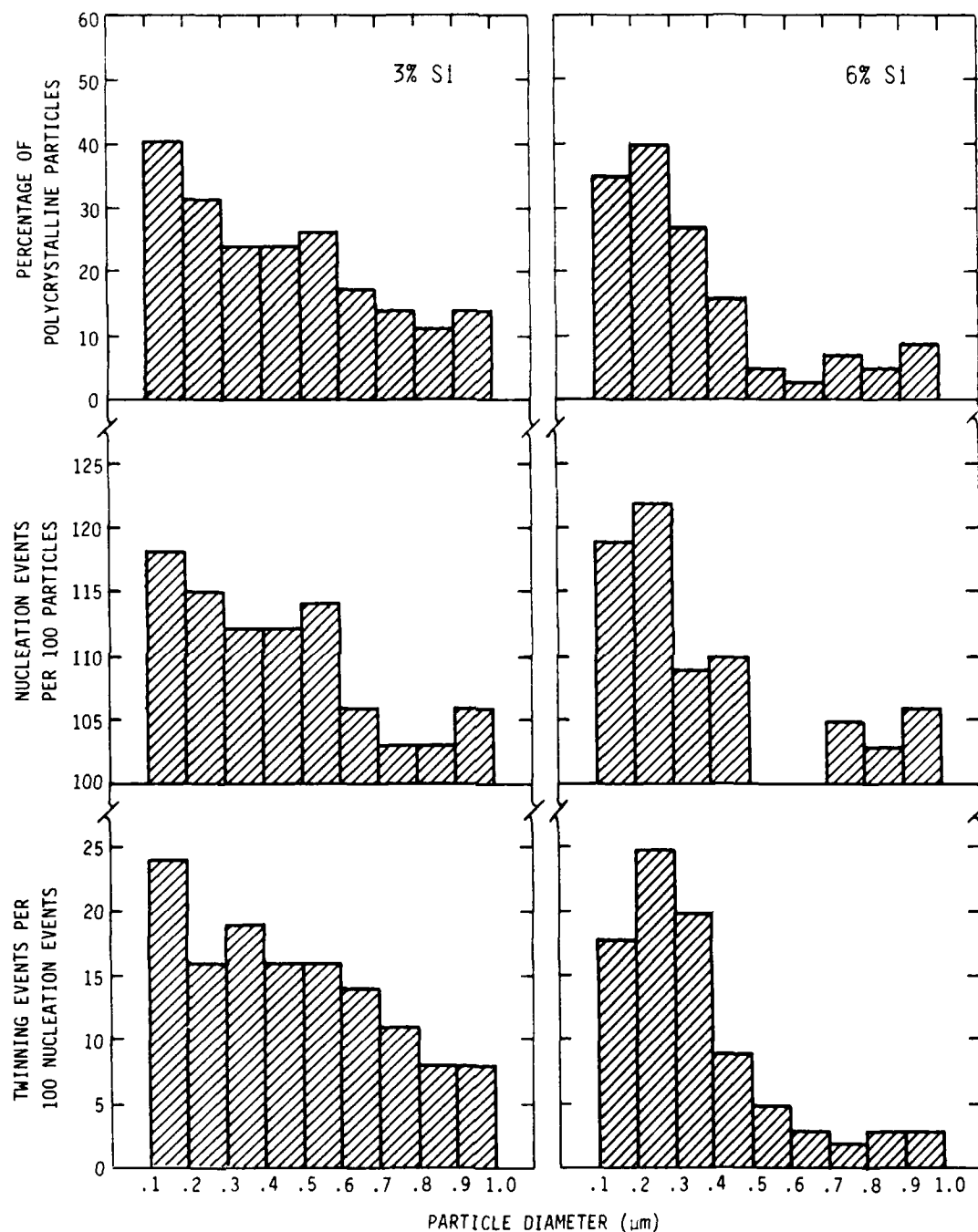
Figure 44. Nucleation behavior of aluminum-silicon powders
produced by EHD atomization. Results are from over
400 particles in each alloy composition.

less segregated than their monocrystal counterparts of equivalent size.

The incidence of multiple nucleation can be accounted for in terms of Equation (2.2), which may be also written as follows

$$N = V \int_{T_M}^{T_N} [J(T)/\varepsilon] \ dT \qquad (9.2)$$

This relationship indicates that the number of nuclei depend on the volume of the assembly (droplet), the nucleation frequency $J(T)$ expressed now as a function of temperature, and the cooling rate ε. Reducing the particle size will decrease the volume $(V \propto r_0^3)$ and increase the cooling rate $(\varepsilon \propto 1/r_0)$, thereby reducing N roughly with a 4th power of the radius. On the other hand, $J(T)$ increases with higher undercoolings ΔT_N, and therefore opposes the volume effect on N. Since $J(T)$ behaves approximately like a step function of ΔT_N, small undercoolings (such as those expected in large droplets) might not affect J significantly and the number of grains should decrease with particle size. However, when substantial undercoolings are achieved (as in the submicron powders) $J(T)$ may increase rapidly with ΔT_N, which varies inversely with r_0. There is conceivably a size range in which the increase in nucleation frequency overcomes the volume effect, enhancing the probability for multiple nucleation.

The occurrence of twins is a phenomenon more difficult to rationalize than multiple nucleation. Twins are considered

rather rare in Al [93], although they have been reported to occur frequently in evaporated films [94] presumably due to stacking errors in the faceted growth from the vapor. Furthermore, most Al twins reported in the literature show boundaries with coherent and incoherent sections.

Twins observed in EHD powders are definitely formed during solidification, as evidenced by the segregation pattern in Figure 45. Note that an incipient cell within the larger grain has penetrated the smaller one, disrupting the otherwise planar boundary. In those twins where a growth direction could be identified, the nucleation site apparently lays on the junction of the twin boundary and the droplet surface. It was then concluded that twins originate from a stacking "accident" in the nucleation process, and the boundary so created propagates later as the solid front advances.

Although it is anticipated that the preservation of the twin boundary will be energetically more favorable than its degeneration into a noncoherent type, its apparent perfection is remarkable in view of the high solidification rates involved in these powders. Furthermore, twin boundaries are sometimes preferentially decorated with precipitates, as in Figure 43, and may show denuded zones in their vicinity, as in Figure 41. If the boundary were perfectly coherent at the atomic level, these effects could be explained by assuming that the segregation conditions where the boundary emerges to the liquid are different from those at the rest of the interface. It could also be argued
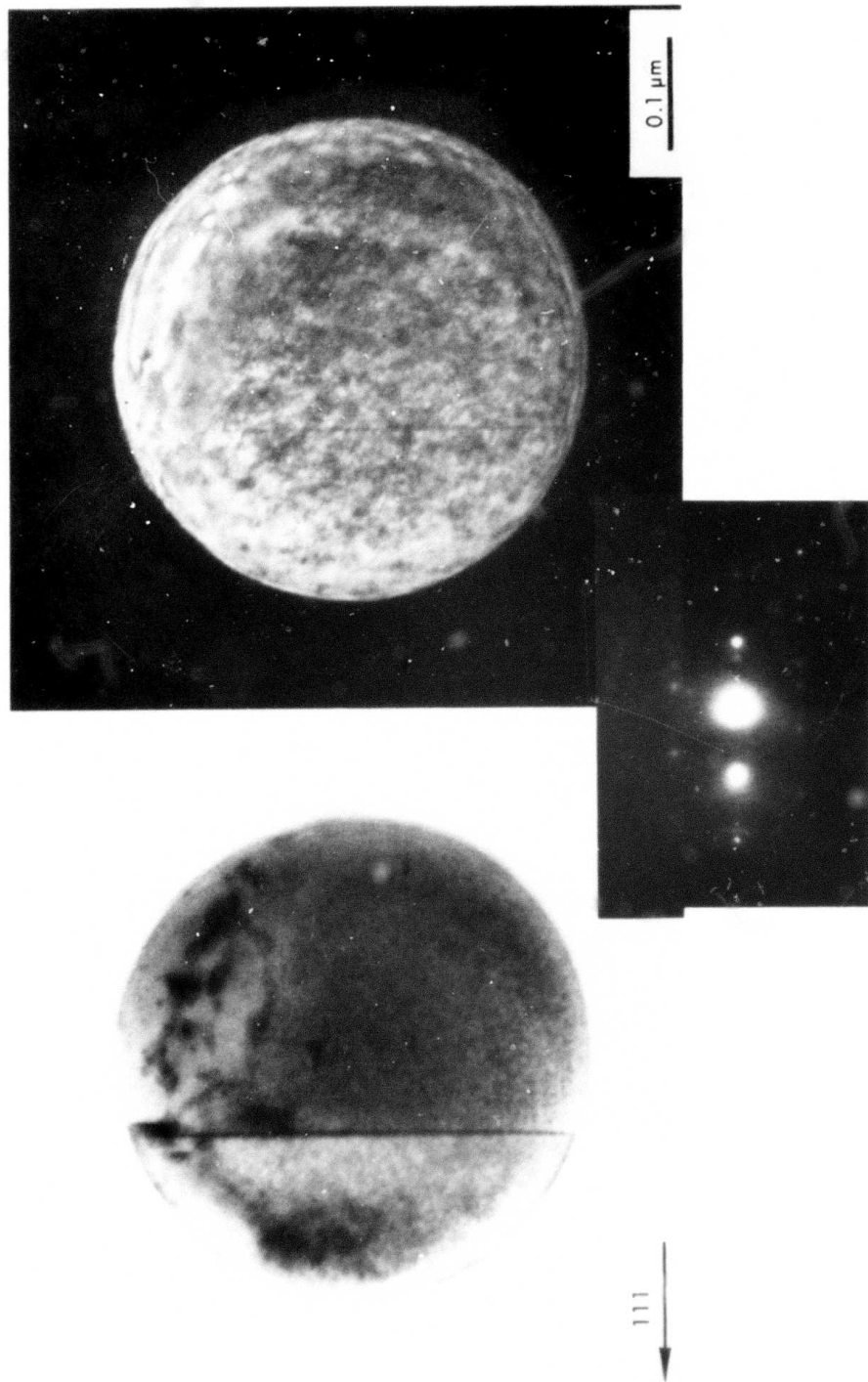
Figure 45. TEM of twin crystals in an Al–6%Si EHD powder. The segregation pattern suggests that nucleation occurred at a point on the boundary-surface intersection.

that small irregularities occur at the boundary during growth,
and their further rearrangement in the solid state (to reduce
surface energy) can accomodate vacancies or solute atoms.

A small fraction of the powders exhibiting this phenomenon
(<10%) show more than one twin boundary (see Figure 46) with as
many as 4 crystallographically related grains being detected in
some cases. In addition, twins with boundaries showing
incoherent segments were also found. These variations of the
structure seem unaccountable at the moment if we ascribe the
origin of the twins only to the nucleation process.

9.3.2 RSR submicron powders

RSR powders exhibit quite different structures from their
EHD submicron counterparts. They are not as spherical, and many
appear extensively polycrystalline with evidence of a texture
reflected in the diffraction pattern, e.g. Figure 47. However,
only in a few instances was it possible to distinguish the
individual crystals, and even under dark field the grain
boundaries were not sharply delineated. The presence of silicon
was revealed by diffraction, but could not be discerned in the
images. Some of this Si was crystallographically related to the
matrix and probably formed after solidification, see Figure 48.

Extensive dislocation substructures were detected in most
powders, as opposed to the EHD material which is commonly
dislocation-free. The relatively high dislocation density,
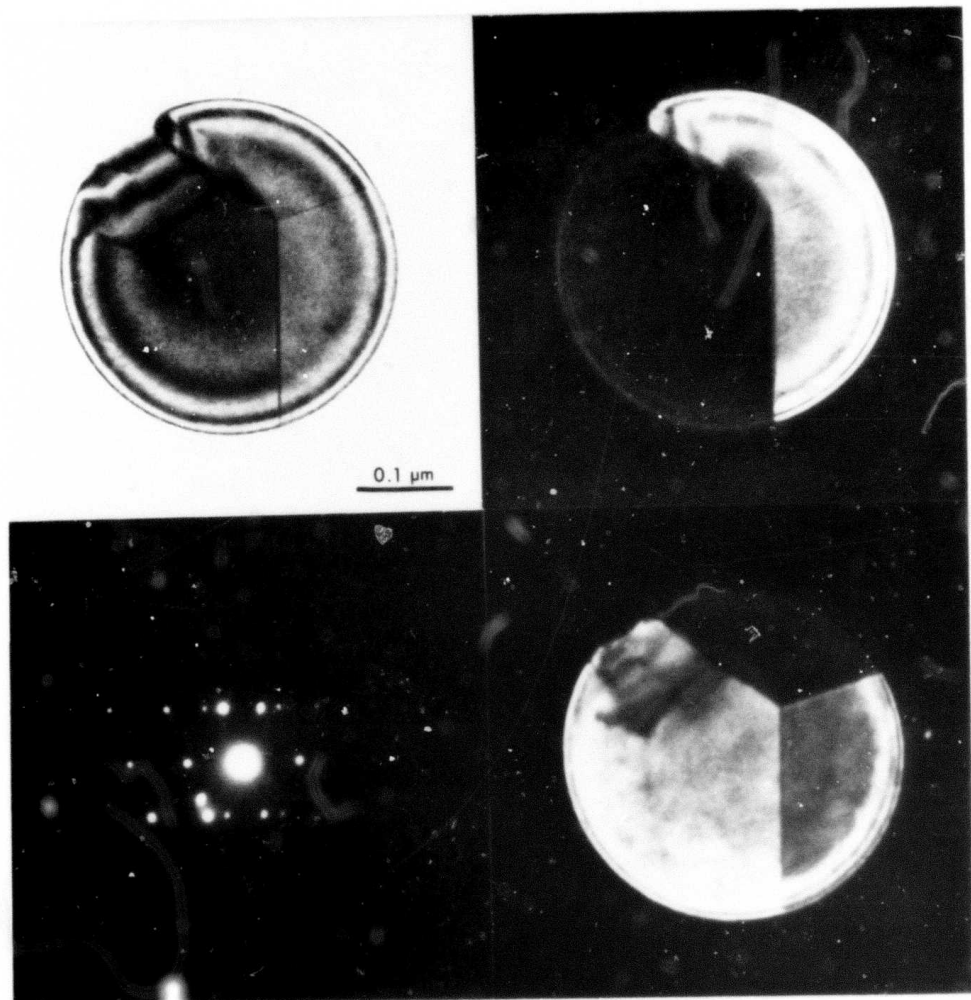
Figure 46. TEM images of multiple twins in an Al-3%Si EHD powder. Two of the boundaries are {111} planes and seem perfectly coherent. A smaller grain with partially faceted boundaries is also evident but out of contrast.

0.1 μm
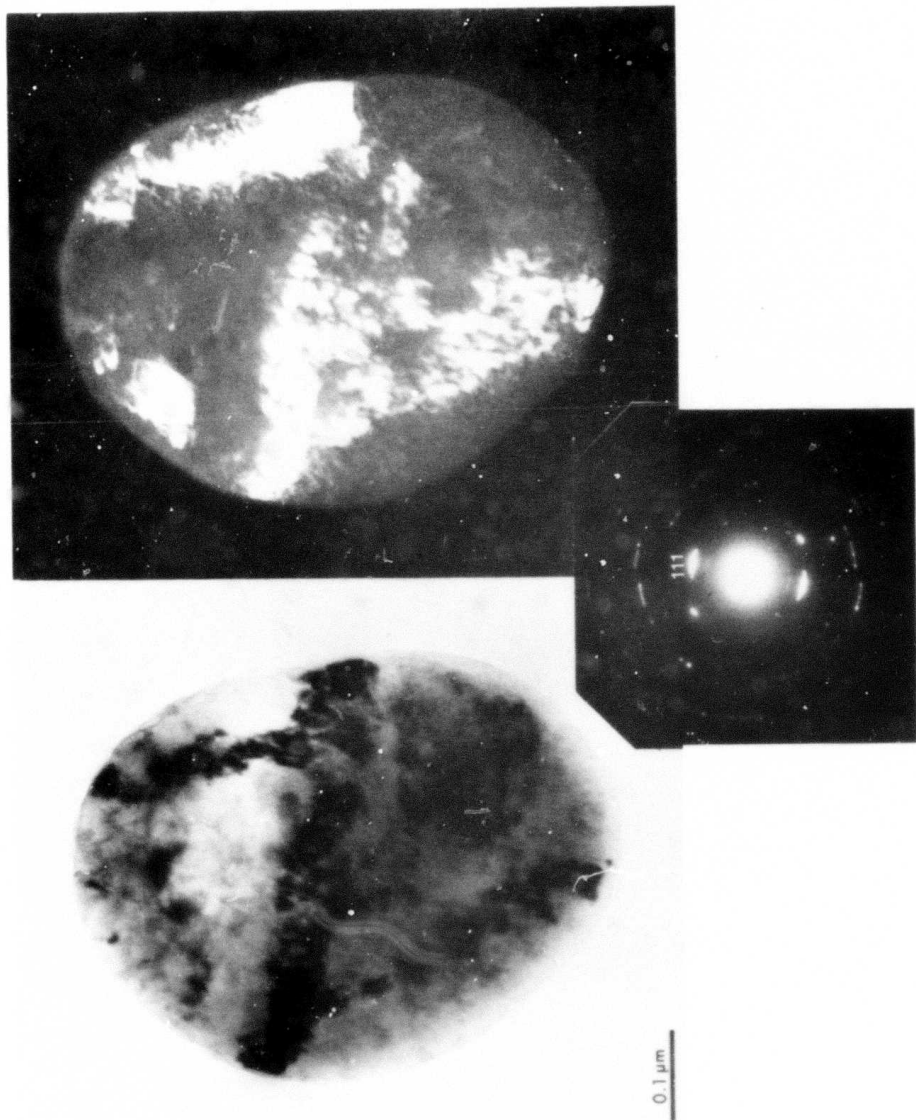
Figure 47. TEM views of an Al-6%Si RSR powder showing a number of grains closely oriented, but no clear boundaries between them.
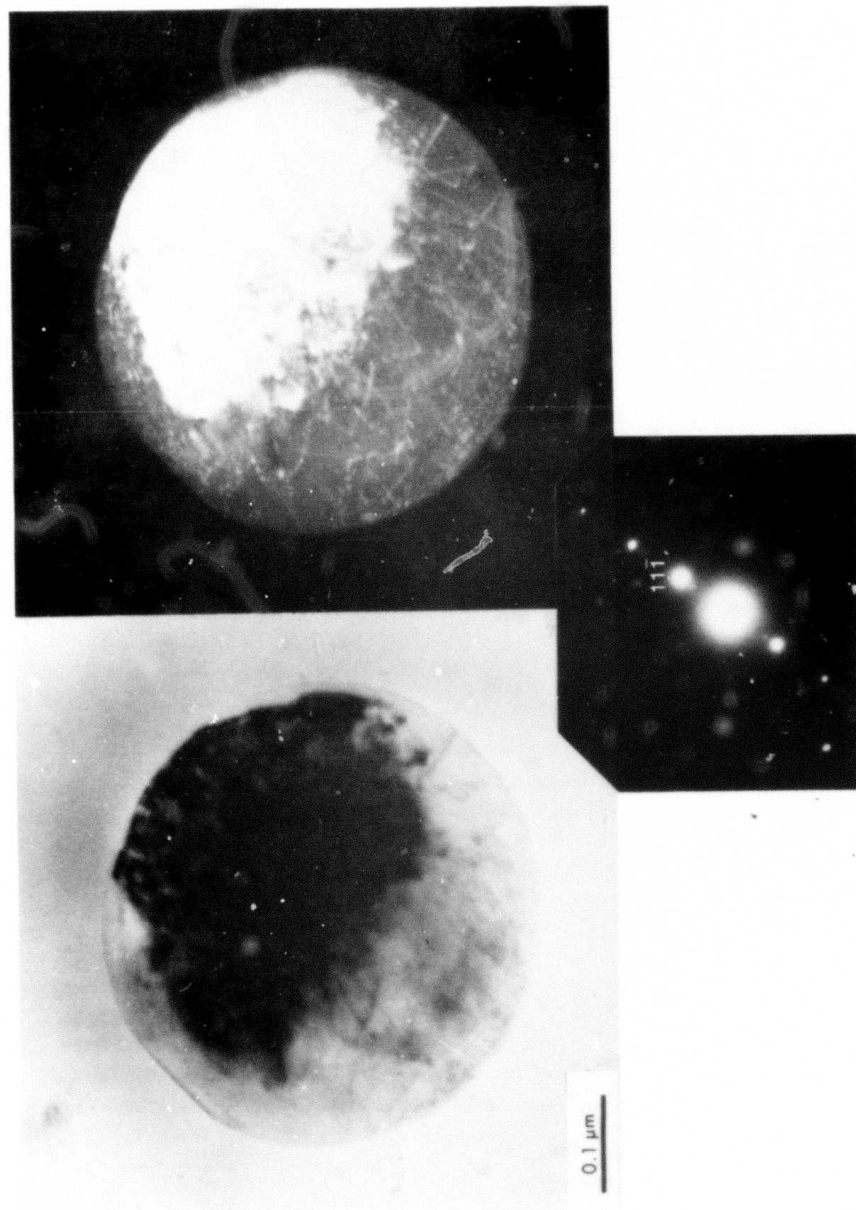
Figure 48. Dislocation substructure in an Al-6%Si RSR powder. The region in contrast actually consists of two grains closely oriented. Some Si, precipitated after solidification, is evident in the diffraction pattern.

probably stemming from collisions of the particle after solidification, largely contributes to the rather confusing aspect of these powders.

About the only conclusive observation at the present time seems to be the absence of cellular or other coarse segregates in the examined specimens. Table 17 indicates that even for a heat transfer coefficient of 2×10^5 W m^{-2} K^{-1}, typical of RSR atomization, the external cooling is expected to extend the rapid solidification regime only slightly over that of the EHD powders. However this increase is not enough to shift the "nose" of the recalescence curve beyond any of the assumed critical temperatures. The apparent decrease in segregation is then likely to reflect the achievement of larger undercoolings ΔT_N in the RSR process at comparable particle sizes. This conclusion is in line with the much larger cooling rates prior to solidification estimated for RSR (e.g. ~10^8 vs. ~10^4 K s^{-1} for a 1 μm droplet), and also with the higher incidence of multiple nucleation noted in these powders. Nevertheless, further work on the solidification behavior of RSR powders is necessary to confirm that cooling rates capable of suppressing the onset of nucleation are achievable during atomization.

9.3.3 Conventional powders

SEM analysis of RSR powders of conventional size (>10 μm) revealed the presence of at least two distinct structures , as
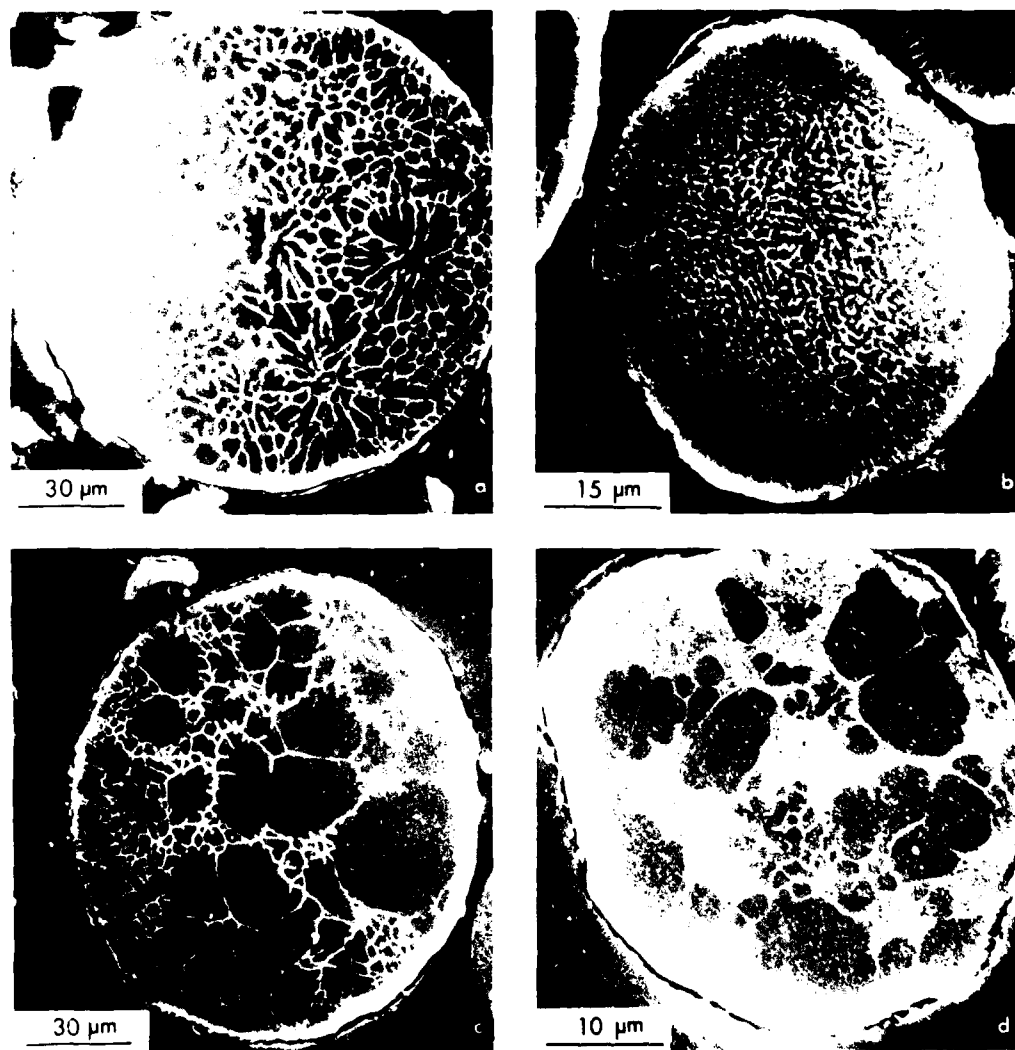
Figure 49. Microstructures observed in Al-4;5%Cu conventional powders; (a) and (b) show two variants of the dendritic structure, whereas (c) and (d) are variants of the duplex structure.

shown in Figure 49. Regular dendritic morphologies with DAS of
~2 μm or less, as well as duplex structures, were observed in the
Al-4.5%Cu alloy. The latter consist of large α-Al regions
surrounded by a finer dendritic matrix or eutectic. Duplex
configurations were not detected in the Al-Si alloys, which were
atomized with higher initial superheat than the Al-4.5%Cu sample.
It has been claimed in a parallel investigation on IN-100 alloy
[95] that the duplex structure results from partial
solidification of the metal on the atomization disc. This
hypothesis was supported by the fact that increasing the initial
melt temperature reduced the proportion of powders showing this
particular configuration.

Figure 49 also suggests that in some instances nucleation
might have occurred inside the droplet, rather than at the
surface, but the evolution of the structure was not readily
apparent. Furthermore, there was no clear indication of whether
these powders achieved any substantial undercooling prior to
nucleation, and homogeneous particles were not observed in this
size range.

Analysis of the microstructural characteristics as a
function of particle size revealed that the dendrite arm spacings
increase from 1 μm for $2r_0 < 44$ μm to about 2 μm for
$105 < 2r_0 < 125$ μm, as shown in Figure 50. This is a consequence
of the increase in solidification time (or reduction in cooling
rate) for the larger particles. In addition, decreasing the
solute content reduces the amount of segregation but does not
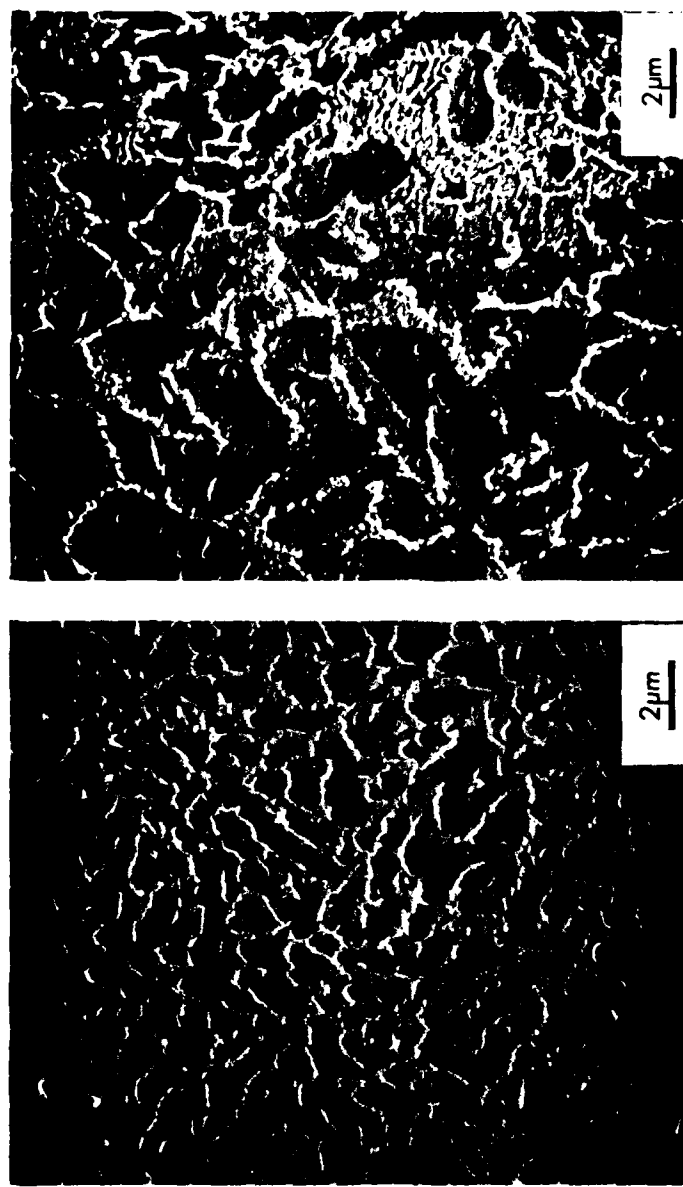
Figure 50. Effect of particle size on the scale of the microstructure in Al-6%Si RSR conventional powders. (a) is typical of particles below mesh 325 (<44 μm) while (b) corresponds to mesh -120 +140 (105-125 μm).

significantly change the scale of the microstructure. Finally, some conventional EHD powders show finer segregate spacings than RSR material of equivalent size. This finding is not consistent with the lower cooling rates expected from radiation, and probably means that the particles analized solidified in contact with a substrate.

Table 18

Effect of Particle Size on the Lattice Parameter[†]
of the Primary Phase in Al-Si Alloys

Diameter (μm)	Al-3%Si	Al-6%Si
<44	4.0445	4.0439
45 - 74	4.0453	4.0447
75 - 105	4.0460	4.0450
105 - 125	4.0462	4.0454

† Average of [220], [331] and [222] peaks.

The effect of particle size on the potential extension in solid solubility was investigated by X-ray diffractometry. The results, shown in Table 18, indicate that reducing the particle size (hence increasing the achievable interface velocities, regardless of geometry) reduces the lattice parameter, a_o, and increases the solute content in the primary phase. In addition, increasing the nominal alloy composition also enhances the solubility of Si. According to previous research by Itagaki et al. [33], an increase of 1% in Si content shrinks the lattice parameter approximately by .001 A. Therefore, it was estimated

that an extra 1.3%Si was dissolved in Al by going from the coarser (>100 μm) to the finer (<44 μm) powders. It should be noted, however, that although the trend in a_o vs. r_0 is consistent with that expected from heat flow considerations, the changes detected are in the order of magnitude of the experimental error. Nevertheless, the approach is conceptually sound, and with careful implementation may provide a reasonable way of relating microstructural modifications to heat flow predictions.

CHAPTER 10

SUMMARY AND CONCLUSIONS

The infinite-series analytical solution to the problem of radially uniform, unidimensional heat flow in an initially superheated metal droplet was coupled to numerical formulations based on the Enthalpy model for studying their solidification behavior. The Newtonian model was reviewed and extended to use it as a basis of comparison and to develop trends for the limiting case where the resistance to heat flow inside the droplet is negligible.

The interface was assumed morphologically stable under all conditions, and the analysis covered two basic growth modes. First, isothermal solidification at the melting temperature (no kinetic barrier or undercooling) with concentric isotherms. In the second mode, undercooling is necessary for nucleation and growth. Solidification starts at a point on the droplet surface and follows an axisymmetric geometry. Although most of the work was focused on powders growing from a single nucleation event, the implications of multiple nucleation were also discussed for the case of microcrystalline structures.

10.1 Liquid Cooling Stage

Analysis of the pre-solidification stage using the Newtonian and series solutions resulted in the following conclusions:

1. Both models predict that the instantaneous average cooling rate in the liquid is directly proportional to the heat transfer coefficient, h, inversely proportional to the droplet radius r_0, and independent of initial superheat θ_0.

2. The cooling time estimated from the analytical solution is always lower than the Newtonian prediction for a fixed surface temperature ($\theta_s = \theta_N$), and higher for a required enthalpy content in the droplet prior to nucleation $\bar{\psi}_N$. t_N increases with r_0 and θ_0, but decreases with increasing h and θ_N.

3. Reaching a desired $\bar{\psi}_N$ value becomes more difficult as the droplet size increases, not only because nucleation must be suppressed to lower temperatures, but also due to the consequent decrease in cooling rate.

4. As expected, the two models converge with decreasing Biot number, but substantial temperature gradients in the droplet were estimated for Bi as low as 0.01.

10.2 Solidification without Undercooling

The trends obtained from the Enthalpy and Newtonian models for solidification without significant undercooling are summarized below:

1. Reducing r_0 diminishes the net solidification time, t_f, in a more pronounced way than the direct proportionality predicted by the Newtonian model. Furthermore, it increases the interface velocity R at equivalent fractions solidified towards the limiting Newtonian values (which are independent of r_0). Reducing r_0 also decreases the G_L/R ratios and increases the achievable cooling rates in the liquid ($\bar{\epsilon}_L$) at the beginning of solidification, and in the solid ($\bar{\epsilon}_S$) at the end of it.

2. Increasing h reduces t_f and increases R in a less pronounced manner than that predicted by the Newtonian model. It always increases G_L/R as well as the cooling rates at any stage during solidification.

3. Increasing initial superheat increases t_f, G_L/R and $\bar{\epsilon}_L$, but decreases R and $\bar{\epsilon}_S$. The effects of superheat are mostly felt in the initial stages of solidification and decay rapidly with decreasing Biot number.

4. The relatively low cooling rates calculated from the enthalpy model are due in part to the prescription of a discrete melting temperature. Alloys solidifying under similar conditions are expected to experience larger cooling rates since the process takes place through a liquid-solid range.

10.3 Solidification with Undercooling

The dimensionless enthalpy-temperature diagram provides a convenient way to describe and compare the thermal history of undercooled droplets during solidification. The approach is particularly useful in the Newtonian analysis, which leads to the following results:

1. The thermal history of the droplet is independent of particle size r_0, for a given growth geometry, and can be readily characterized by two parameters: the initial undercooling θ_N, and the ratio of a dimensionless kinetic coefficient to the Biot number, (K/Bi). The latter reflects the degree of predominance of the recalescence rate (release of latent heat) over the external cooling.

2. The thermal history normally consists of two regimes. The first one is the recalescence or "rapid solidification" stage, where the undercooled droplet is absorbing most of the released heat of fusion, and the heat loss to the environment plays only a minor role. The second regime is one of slower growth, roughly isothermal, and is controlled by the external rate of heat extraction.

3. For typical values of K/Bi encountered in atomization (K/Bi>100), the external cooling has little or no effect in extending the "rapid solidification" regime to a

fraction solid substantially larger than that dictated by the limiting case of adiabatic solidification, $g^a = -\theta_N$. Increasing the number of nucleation events further reduces the role of the external cooling during recalescence.

4. Although the net solidification time, t_f, decreases with increasing undercooling prior to nucleation, the total time spent by the droplet in cooling and solidification increases, as much as twice from the case of no-undercooling, thereby requiring longer flight times in a given atomizer. As before, the times increase with r_0 and decrease with larger h values.

The Enthalpy model for undercooled solidification revealed that departures from the Newtonian model may occur at Biot numbers as low as 10^{-4}. This is a direct consequence of the "local" recalescence of the interface which is now able to alter both its velocity and the thermal field in its vicinity in order to accomodate tha latent heat released. In general, this model predicts that:

1. For a given undercooling, the local recalescence of the interface is accelerated (and hence the extent of rapid solidification reduced) as r_0 and the kinetic parameter K_M are increased.

2. Interface velocities and undercoolings at any fraction solid are increased by reducing r_0 or increasing θ_N and h, although this latter variable becomes important only

towards the end of recalescence. Furthermore, increasiang K_M will reduce the interface undercooling but increase its velocity.

3. Both models indicate that if the critical temperature, T_C, for a certain metastable effect is reasonably close to T_M, rapid solidification may be obtained with moderate initial undercoolings provided the K/Bi ratio is small enough to make $\Delta T^*_{min} < \Delta T_C$. However, if $T_C << T_M$ the extent of rapid solidification is limited by θ_N. In any case, the Newtonian model always provides a limit to the achievable fraction solidified below T_C.

4. Maximum temperature differences inside the droplet (i.e. departure from Newtonian conditions) increase with Biot number, K_M and ΔT_N.

5. The interface shapes predicted by the enthalpy model are close to the convex spherical front configuration assumed for the Newtonian analysis. At large Bi and K_M, and small θ_N the interface becomes concave towards the liquid, approaching the concentric geometry of the no-undercooling case.

10.4 Microstructural Observations

Examination of rapidly solidified aluminum alloy powders produced by two different atomization techniques (EHD and RSR)

revealed some novel microstructures, especially in the submicron size range. The results were coupled with heat flow concepts in developing an understanding of the thermal history during solidification. The relevant findings are listed below:

1. Decreasing the powder size, therefore increasing the achievable undercoolings and interface velocities, reduces the extent of segregation. This translates into an increased solute content of the primary phase, detected in the conventional size powders, and eventually in homogeneous solidification of submicron droplets with Si contents as high as 6%.

2. Increasing h from radiation (EHD) to convection (RSR) appears to reduce segregation, presumably by suppresing nucleation towards larger undercoolings due to an increase of 4 orders of magnitude in the calculated cooling rate.

3. Submicron powders showing segregation but not cellular breakdown may be evidence of interface stability due to surface tension effects.

4. Increasing undercooling by reducing particle size promotes multiple nucleation and the incidence of twin crystals in the submicron range. The latter are believed to originate mainly from stacking "accidents" in the nucleation process. The twin boundaries appear to be coherent, although a few instances of incoherent segments were observed. In general, twins and

polycrystalline powders are less segregated than their
monocrystal counterparts.

LIST OF REFERENCES

1. R. E. Spear and G. R. Gardner: Trans. AFS 71, 209 (1963).

2. T. F. Bower, H. D. Brody and M. C. Flemings: Trans. AIME 236, 624 (1966).

3. B. P. Bardes and M. C. Flemings: Trans. AFS 74, 406 (1966).

4. G. R. Armstrong and H. Jones: in Solidification and Casting of Metals. Proceedings of a Conference at the University of Sheffield, 18-21 July 1977. London: The Metals Society, 1979, p. 454.

5. W. A. Dean and R. E. Spear: in Strenghtening Mechanisms: Metals and Ceramics, J. J. Burke et al. (eds.). Syracuse, NJ: Syracuse University Press, 1966, p. 268.

6. H. Matyja, B. C. Giessen and N. J. Grant: J. Inst. Met. 96, 30 (1968).

7. C. Suryanarayana and T. R. Anantharaman: J. Mater. Sci. 5, 992 (1970).

8. P. Ramachandrarao, M. G. Scott and G. A. Chadwick: Phil. Mag. 25, 961 (1972).

9. H. A. Davies and J. B. Hull: J. Mater. Sci. 9, 707 (1974).

10. J. A. Horwath and L. F. Mondolfo: Acta Met. 10, 1037 (1962).

11. H. M. Skelly and C. F. Dixon: Int. J. Powder Met. 7[3], 47 (1971).

12. R. J. Towner: Met. Prog. 73[5], 70 (1958).

13. T. R. Anantharaman and C. Suryanarayana: J. Mater. Sci. 6, 1111 (1971).

14. H. Jones: Aluminium, 54[4], 274 (1978).

15. K. O. Krishnanand and R. W. Cahn: in Rapidly Quenched Metals, N. J. Grant and B. C. Giessen (eds.). Cambridge, MA: M.I.T. Press, 1976, p. 67.

16. G. Thursfield and M. J. Stowell: J. Mater. Sci. 9, 1644 (1974).

17. C. Panseri and M. Paganelli: Alluminio 37, 387 (1968).

18. N. J. Grant: Fizika 2, Suppl. 2, 16.1 (1970).

19. A. F. Polesya and A. Stepina: Met. Abs. 3[7], 800 (1970).

20. H. Jones: Rep. Prog. Phys 36, 1425 (1973).

21. P. E. Brown and C. M. Adams: Trans. AFS 69, 879 (1961).

22. T. Z. Kattamis and R. Mehrabian: J. Vac. Sci. Tech. 11[6], 1118 (1974).

23. M. H. Burden and H. Jones: Metallography 3[3], 307 (1970).

24. H. Jones: Mat. Sci. Eng. 5, 1 (1969/70).

25. I. R. Hughes and H. Jones: J. Mat. Sci. 11, 1781 (1976).

26. D. B. Williams and J. W. Edington: in Rapidly Quenched Metals, N. J. Grant and B. C. Giessen (eds.). Cambridge, MA: M.I.T. Press, 1976, p. 135.

27. N. I. Varich and K. E. Kolesnichenko: Metall. Abs. 28, 715 (1961).

28. N. I. Varich and R. B. Lyukevich: Russ. Met. [4], 58 (1970).

29. E. Blank: Z. Metallkunde 63, 324 (1972).

30. M. H. Jacobs, A. G. Doggett and M. J. Stowell: J. Mater. Sci. 9, 1631 (1974).

31. K. M. Entwistle, P. Fuller and I. Brough: Acta Met. 26, 1055 (1978).

32. L. F. Mondolfo: Aluminum Alloys: Structure and Properties. London: Butterworths, 1976, p. 373.

33. M. Itagaki, B. C. Giessen and N. J. Grant: Trans. Quart. ASM 61, 330 (1968).

34. S. K. Bose and R. Kumar: J. Mater. Sci 8, 1795 (1973).

35. H. Matyja, K. C. Russel, B. C. Giessen and N. J. Grant: Met. Trans. 6A, 2249 (1975).

36. M. Kaczorowski, M. W. Grabski, J. Sawicki and P. Murza-Mucha: J. Mater. Sci. 14, 2781 (1979).

37. E. H. Hollingsworth, G. R. Frank and R. E. Willett: Trans. AIME 224, 188 (1962).

38. P. Ramachandrarao and M. Laridjani: J. Mater. Sci. 9, 434 (1974).

39. P. Ramachandrarao, M. Laridjani and R. W. Cahn: Z. Metallkunde 63, 43 (1972).

40. H. A. Davies and J. B. Hull: J. Mater. Sci 11, 2149 (1976).

41. H. Jones: in Rapidly Quenched Metals, N. J. Grant and B. C. Giessen (eds.). Cambridge, MA: M.I.T. Press, 1976, p. 1.

42. J. W. _ ristian: The Theory of Transformations in Metals and Alloys. Oxford: Oxford University Press, 1965, Ch. 14.

43. W. J. Boettinger, F. S. Biancaniello, G. M. Kalonji and J. W. Cahn: in Rapid Solidification Processing, Principles and Technologies II, R. Mehrabian, B. H. Kear and M. Cohen (eds.). Baton Rouge, LA: Claitor Pub. Div., 1980, p. 50.

44. J. W. Christian: The Theory of Transformations in Metals and Alloys. 2nd. Edition, Part I.- Equilibrium and General Kinetic Theory. Oxford: Pergamon Press, 1975, Ch. 10.

45. D. Turnbull: Trans. AIME 175, 774 (1948).

46. H. Reiss and J. L. Katz: in Rapid Solidification Processing, R. Mehrabian, B. H. Kear and M. Cohen (eds.). Baton Rouge, LA: Claitor Pub. Div., 1978, p. 64.

47. D. Turnbull: J. Chem. Phys. 20, 411 (1952).

48. J. H. Hollomon and D. Turnbull: Prog. Metal Phys. 4, 333 (1953).

49. J. H. Perepezko, D. H. Rasmussen, I. E. Anderson and C. R. Loper, Jr.: in Solidification and Casting of Metals. Proceedings of a Conference at the University of Sheffield, 18-21 July 1977. London: The Metals Society, 1979, p. 169.

50. J. H. Perepezko: in Rapid Solidification Processing, Principles and Technologies II, R. Mehrabian, B. H. Kear and M. Cohen (eds.). Baton Rouge, LA: Claitor Pub. Div., 1980, p. 56.

51. R. E. Cech and D. Turnbull: Trans. AIME 191, 242 (1951).

52. D. Turnbull and R. E. Cech: J. Appl. Phys. 21, 804 (1950).

53. B. E. Sundquist and L. F. Mondolfo: Trans. AIME 221, 157 (1961).

54. R. T. Southin and G. A. Chadwick: Acta Met. 26, 223 (1978).

55. R. Cantor and R. D. Doherty: Acta Met. 27, 33 (1979).

56. J. W. Cahn, W. B. Hillig and G. W. Sears: Acta Met. 12, 1421 (1964).

57. D. Turnbull: in Thermodynamics in Physical Metallurgy. Metals Park, OH: American Society for Metals, 1949.

58. R. J. Schaefer and M. E. Glicksman: J. Crystal Growth 5, 44 (1969).

59. W. A. Tiller, J. W. Rutter, K. A. Jackson and B. Chalmers: Acta Met. 1, 428 (1953).

60. W. W. Mullins and R. F. Sekerka: J. Appl. Phys. 35[2], 444 (1964).

61. R. F. Sekerka: J. Appl. Phys 36[1], 264 (1965).

62. M. Cohen, B. H. Kear and R. Mehrabian: in Rapid Solidification Processing, Principles and Technologies II, R. Mehrabian, B. H. Kear and M. Cohen (eds.). Baton Rouge, LA: Claitor Pub. Div., 1980, p. 1.

63. J. W. Cahn, S. R. Coriell and W. J. Boettinger: in Laser and Electron Beam Processing of Materials, C. W. White and P. S. Peercy (eds.). Materials Research Society, 1979.

64. S. R. Coriell and R. F. Sekerka: in Rapid Solidification Processing, Principles and Technologies II, R. Mehrabian, B. H. Kear and M. Cohen (eds.). Baton Rouge, LA: Claitor Pub. Div., 1980, p. 35.

65. J. C. Baker: "Interfacial Partitioning During Solidification". Ph.D. Thesis, M.I.T. 1970, Ch. 5.

66. J. S. Langer and H. Muller-Krumbhaar: Acta Met. 26, 1681-1708 (1978). (A series of 3 papers).

67. G. P. Ivantsov: Dokl. Akad. Nauk. USSR 58, 567 (1947). Translation available as Gen. El. Res. Lab. Report 60-RL-2511M.

68. G. Horvay and J. W. Cahn: Acta Met. 9, 695 (1961).

69. M. E. Glicksman and S. C. Huang: in Rapid Solidification Processing, Principles and Technologies II, R. Mehrabian, B. H. Kear and M. Cohen (eds.). Baton Rouge, LA: Claitor Pub. Div., 1980, p. 68.

70. T B. Masalski and Y. Bienvenu: in Rapidly Quenched Metals, N. J. Grant and B. C. Giessen (eds.). Cambridge, MA: M.I.T. Press, 1976, p. 95.

71. J. C. Baker and J. W. Cahn: Acta Met. 17, 575 (1969).

72. J. C. Baker and J. W. Cahn: in Solidification. Metals Park OH: American Society for Metals, 1971, p. 23.

73. M. Hillert and Bo Sundman: Acta Met. 25, 11 (1977).

74. J. P. Hirth: Met. Trans 9A, 401 (1978).

75. J. Szekely and R. J. Fisher: Met. Trans 1, 1480 (1970).

76. D. J. Hodkin, P. W. Sutcliffe, P. G. Mardon and and L. E. Russel: Powder Met. 16, 277 (1973).

77. M. R. Glickstein, R. J. Patterson II and N. E. Shockley: in Rapid Solidification Processing, R. Mehrabian, B. H. Kear and M. Cohen (eds.). Baton Rouge, LA: Claitor Pub. Div., 1978, p. 46.

78. G. H. Geiger and D. R. Poirer: Transport Phenomena in Metallurgy. Reading, MA: Addison-Wesley, 1973, p. 291,303.

79. R. Mehrabian: in Rapid Solidification Processing, R. Mehrabian, B. H. Kear and M. Cohen (eds.). Baton Rouge, LA: Claitor Pub. Div., 1978, p. 9.

80. Thermophysical Properties of Matter. TPRC Data Series vol. 7, Thermal Radiation Properties: Metallic Elements and Alloys. Y. S. Toloukian and D. P. DeWitt (eds.). New York, NY: Plenum, 1970, p. 2.

81. A. R. Cox: "Application of Rapidly Solidified Alloys". Quarterly Report, DARPA contract F33615-76-C-5136, Aug, 1978.

82. K. A. Jackson, D. R. Uhlmann and J. D. Hunt: J. Crystal Growth 1, 1 (1967).

83. M. E. Glicksman and R. J. Shaefer: J. Crystal Growth 1, 297 (1967).

84. G. J. Abbaschian and S. F. Ravitz: J. Crystal Growth 28, 16 (1975).

85. A. D. Pasternak: Phys. Chem. of Liquids 3, 41 (1972).

86. Metals Reference Book: 5th. Edition, C. J. Smithells (ed.). London: Butterworths, 1976, p. 944.

87. N. Shamsundar and E. M. Sparrow: Trans. ASME, Series C, 97, 333 (1975).

88. V. S. Arpaci: Conduction Heat Transfer. Reading, MA: Addison-Wesley, 1966, p. 288.

89. P. Moon and D. E. Spencer: Field Theory for Engineers. Princeton, NJ: D. Van Nostrand, 1961, p. 376-384.

90. J. Perel, J. F. Mahoney, P. Duwez and B. E. Kalensher: in Rapid Solidification Processing, Principles and Technologies II, R. Mehrabian, B. H. Kear and M. Cohen (eds.). Baton Rouge, LA: Claitor Pub. Div., 1980, p. 287.

91. J. F. Mahoney, J. Perel, Z. Shanfield and B. E. Kalensher: "Development of a Tabletop Model for the Generation of Amorphous/Microcrystalline Metal Powders". Technical Report, ONR Contract N00014-77-C-0373, 30 April 1980.

92. P. A. Joly and R. Mehrabian: J. Mater. Sci. 9, 1446 (1974).

93. C. M. Sargent: Trans. AIME 242, 1188 (1968).

94. M. J. Olney and G. C. Smith: Acta Met. 3, 205 (1955).

95. B. H. Kear, P. R. Holiday and A. R. Cox: Met. Trans. 10A, 136 (1979).

APPENDIX A

METAL PROPERTIES USED IN THE CALCULATIONS*

	Al	Fe	Ni
Melting Temperature T_M (K)	933	1810	1726
Hypercooling Temperature T_H (K)	569	1464	1315
Heat of Fusion ΔH_M (10^5 J kg^{-1})	3.95	2.72	3.02
Average Density ρ (kg m^{-3})	2.46	7.19	8.07
Specific Heat (10^3 J kg^{-1}K^{-1}) C_L	1.09	0.787[†]	0.734
C_S	1.19	0.764[†]	0.619[†]
Thermal Conductivity (W m^{-1} K^{-1}) k_L	90.8	40.3	39.3[†]
k_S	210.8	34.6	87.0[†]
Thermal Diffusivity (10^{-5}m^2 s^{-1}) α_L	3.4	0.712	0.664
α_S	7.18	0.630	1.74
Stefan Number Ste (T_G = 300)	1.74	4.37	3.47

* Thermophysical properties at T_M
† Estimated by extrapolation.

APPENDIX B

NOMENCLATURE

Dimensioned variables

A   heat transfer area between two neighbor volume elements

a_O lattice parameter of the aluminum

C   specific heat

DAS   dendrite arm spacing

D_L self-diffusion coefficient in the liquid

d_{MX} distance between two nearest neighbors in a close packed microcrystalline structure

E_D activation energy of diffusion

e   emissivity

F   free energy

G   temperature gradient at the liquid solid interface

g   fraction solid

H   enthalpy content over that of the solid at the melting temperature H_{SM}

ΔH_M heat of fusion

h   heat transfer coefficient

J   nucleation frequency

K_M kinetic parameter relating the velocity and undercooling in the linear law, evaluated at the melting temperature

k   thermal conductivity

m   metric coefficients

N   number of nuclei or grains

Q   heat flow term in the enthalpy balance equations

R   interface velocity

r   radial coordinate, $0 \leq r \leq r_0$

T   temperature

T_C critical temperature for a metastable effect to be achieved by rapid solidification

T_0 initial temperature

ΔT undercooling

$\Delta (T)$ maximum temperature difference inside the droplet during solidification

t   time

V   volume

V   velocity of the droplet relative to the cooling environment (gas)

z   distance from the center of the droplet along the growth axis

α thermal diffusivity

δ length of an interface step

ε cooling rate

γ average jumping distance for an atom to join the solid

ν kinematic viscosity

ρ density

σ Stefan-Boltzmann constant

υ jumping frequency of an atom

Dimensionless variables

Bi   Biot number, hr_0/k_L

Fo   Fourier number, $\alpha t/r_0^2$

K   Kinetic parameter, $(r_0/\alpha_L)\ (\Delta H_M/C_L)\ K_M$

M   Mach number, V_∞/V_{sound}

Nu   Nusselt number, $2hr_0/k_G$

Pe   Peclet number, $Rr_t/2\alpha_L$

Pr   Prandtl number, ν/α

$\underline{R}$ interface velocity, $(r_0/\alpha_L)\ R$

Ste   Stefan number, $C_L(T_M - T_G)/\Delta H_M$

u   coordinate in the bispherical system perpendicular to the growth direction

v   coordinate in the bispherical system along the growth direction

z^* position of the interface along the growth axis, z/r_0

β Cahn's parameter in the kinetic equations

θ temperature, $C_L(T - T_M)/\Delta H_M$

ϕ radial coordinate, r/r_0

ψ enthalpy, $(H - H_{SM})/\Delta H_M$

Subscripts

c   convection

E   equilibrium

f   end of solidification

G   gas environment

H   hypercooling

i   nodal index in the radial coordinate for the case of
      no-undercooling and in the u direction for the bispherical
      mesh.

j   nodal index in the v direction for the bispherical mesh

k   time step index

ℓ denotes the node containing the liquid-solid interface

L   liquid

M   at the melting temperature

m   number of nodes in the v direction

N   at the moment of nucleation

n   number of nodes in the ϕ direction for the concentric model,
      and in the u direction for the bispherical mesh

r   radiation

S   solid

s   at the surface

t   at the dendrite tip

Superscripts

*   at the interface

+   in the positive r direction for the concentric geometry

-     in the negative r direction

N   in the positive u direction for the bispherical mesh

S   in the negative u direction

E   in the positive v direction

W   in the negative v direction